Kinetic characterization and modelling of sequentially entrapped enzymes in 3D-printed PMMA microfluidic reactors for the synthesis of amorphadiene via the isopentenol utilization pathway

by

Derek C. Kabernick

A thesis
presented to the University of Waterloo
in fulfillment of the
thesis requirement for the degree of
Master of Applied Science
in
Chemical Engineering

Waterloo, Ontario, Canada, 2021

Author's Declaration

I hereby declare that I am the sole author of this thesis. This is a true copy of the thesis, including any required final revisions, as accepted by my examiners.

I understand that my thesis may be made electronically available to the public.

Abstract

Recent technological developments in the field of additive manufacturing have gained researcher attention as a low cost, high resolution, method for the fabrication of microfluidic reactors. In recent years cascade immobilized enzyme microfluidic reactors have been developed for *in vitro* synthesis, cofactor regeneration, and product detection due to the benefits of enzyme immobilization such as increased stability, ease of product recovery, and ability for continuous operation. Reviews of the current literature relating to 3D-printed cascade immobilized enzyme microfluidic reactors and isoprenoid synthesis have been performed and analyzed to identify cascade enzyme entrapment and the recently discovered, synthetic, isopentenol utilization pathway as promising topics for investigation. Expanding upon the current fields of cascade immobilized enzyme systems and isoprenoid synthesis, in this study, additive manufacturing was used to entrap enzymes during 3D-printing for the fabrication of sequentially immobilized microfluidic reactors to synthesize amorphadiene, a precursor to the antimalaria drug artemisinin, *in vitro* via the isopentenol utilization pathway.

As an initial proof-of-concept to investigate the feasibility of simultaneously entrapping enzymes in a poly(methyl methacrylate) matrix during stereolithographic 3D-printing, alkaline phosphatase was kinetically characterized for microfluidic reactor modelling in COMSOL Multiphysics and tested experimentally. Kinetic characterization demonstrated no significant shift in the modelled substrate binding affinity between the free and immobilized assays having values of 1.57 ± 0.02 µM and 1.59 ± 0.01 µM, respectively. Due to the internal diffusion limitations of enzyme entrapment, the modelled immobilization efficiencies at a surface area to volume ratio of 2666 m^2/m^3 were low ranging from 0.028 ± 0.003 to 0.057 ± 0.002. Continuous operation of an immobilized alkaline phosphatase microfluidic reactor demonstrated high stability retaining 85.4-92.3 % and 54.2 % of its initial mean enzymatic activity over 16 days of continuous operation and 84 days of storage, respectively. COMSOL Multiphysics was also an effective modelling tool with only a 3.9 % difference between the observed and modelled outlet product concentrations of 4-nitrophenol.

Based on the promising modelling and characterization results for alkaline phosphatase, the isopentenol utilization pathway enzymes were synthesized, purified, and characterized having normalized immobilization efficiencies ranging from 0.0135 ± 0.010 to 0.249 ± 0.026 for a surface to volume ratio of 2666 m^2/m^3. Amorphadiene was successfully synthesized for the enzymes free in solution and sequentially immobilized along the walls of a microfluidic reactor resulting in an amorphadiene productivity of 0.00115 ± 0.0008 mg/L·h and $1.81\text{x}10^{-6} \pm 0.18 \pm 10^{-6}$ mg/L·h β-caryophyllene equivalent, respectively. Monitoring the stability of the downstream enzyme compartments was hindered due to low pyrophosphate detectability, however the stability of the choline kinase and isopentenyl phosphate kinase compartments were relatively high with only a 11.4-16.6 % decrease in the concentration of adenosine diphosphate after 10-13 days of continuous operation and 58.7-60.7 % after 41 days. The relative steady-state error of the COMSOL Multiphysics modelled outlet adenosine diphosphate concentration was only 1.2-4.9 %, however the design of the cascade microfluidic reactor was significantly limited by the requirement for extensive enzyme dilution and future work will depend on further stereolithographic developments resolving this limitation.

Acknowledgments

Foremost, I would like to thank my supervisors Dr. Valerie Ward and Dr. Jeff Gostick for their continued guidance, support, and training throughout my progression writing this thesis and earning my Master of Applied Science in Chemical Engineering degree. I would also like to thank the PMEAL and Bio research groups in the chemical engineering department for taking an interest in my research and providing valuable insight. Lastly, I would like to thank Dr. Marc Aucoin, Dr. Raymond Legge, and Dr. Perry Chou for permission to use their laboratory equipment, as well as Caleb Seward, Hamid Hamedaani, Jared Roth, and Sepandar Malekghasemi for their cooperation and assistance in the lab. I would also like to acknowledge the University of Waterloo Multi-Scale Additive Manufacturing Lab for their financial support.

Table of Contents

List of Figures

List of Tables

List of Abbreviations

AACT - acetoacetyl-coenzyme A thiolase

AAO – ascorbate oxidase

AB-NTA - N-(5-amino-1-carboxy-pentyl) iminodiacetic acid

ABS – acrylonitrile butadiene styrene

AcAcCoA - acetoacetyl-coenzyme A

AcBzTacn - 1-Aceto-4-benzyltriazacyclononane

AcCoA – acetyl coenzyme A

AD – amorphadiene

ADP – adenosine diphosphate

ADS – amorphadiene synthase

AHD – alcohol dehydrogenase

ALP – alkaline phosphatase

ATP - adenosine triphosphate

BFD – benzoylformate decarboxylase

BSA – bovine serum albumin

CAD - computer-aided design

CAT – catalase

CDP–ME - 4-diphosphocytidyl-2-C-methyl-D-erythritol

CDP-MEP – 4-diphosphocytidyl-2-C-methyl-D-erythritol-2-phosphate

CE – cholesterol esterase

CFD – computational fluid dynamics

CK – choline kinase

CMP – cytidine monophosphate

CNO - calcium niobate

CoA - coenzyme A

COD – cholesterol oxidase

C-P450 - cytochrome-P4502C9

CTP – cytidine triphosphate

DC – detergent compatible

DCW – dry cell weight

DEA – diethanolamine

DLP – digital light processing

DMAP - dimethylallyl monophosphate

DMAPP - dimethyl allyl diphosphate

DMSO – dimethyl sulphoxide

DP - dahms pathway

DXP – 1-deoxy-D-xylulose-5-phosphate

DXR – 1-deoxy-D-xylulose-5-phosphate reductase

DXS – 1-deoxy-D-xylulose-5-phosphate synthase

EDC - 1-ethyl-3-(3-dimethylaminopropyl) carbodiimide

EDP - Entner-Doudoroff pathway

EMP - Embden-Meyerhof-Parnas

EN – ethylenediamine

F_{ald}DH - formaldehyde dehydrogenase

F_{ate}DH - formate dehydrogenase

FDM – fused deposition modelling

FPP – farnesyl diphosphate

G3P – D-glyceraldehyde 3-phosphate

GA – glutaraldehyde

GC-MS – gas chromatography-mass spectroscopy

GFP – green fluorescent protein

GGPP - geranyl geranyl disphosphate

GOD – glucose oxidase

GPP – geranyl diphosphate

HA – hydroxyacetone

HMBPP – 1-hydroxy-2-methyl-2-E-butenyl-4-diphosphate

HMDA – hexamethylene-diamine

HMG - 3-hydroxy-3-methylglutaric acid

HMG-CoA - 3-hydroxy-3-methylglutaryl-coenzyme A

HMGR - 3-hydroxy-3-methylglutaryl-CoA reductase

HMGS - 3-hydroxy-3-methylglutaryl-coenzyme A synthase

HRP – horseradish peroxidase

IDI - isopentenyl disphosphate isomerase

INV – invertase

IP - isopentenyl monophosphate

IPK - isopentenyl phosphate kinase

IPP - isopentenyl disphosphate

ISP – isoprenol

IspA – farnesyl diphosphate synthase

IspD – MEP cytidylyl-transferase

IspE – 4-diphosphocytidyl-2-C-methyl-D-erythritol kinase

IspF - 2-C-methyl-D-erythritol-2,4-cyclodiphosphate synthase

IspG – 1-hydroxy-2-methyl-2-E-butenyl-4-diphosphate synthase

IspH – 1-hydroxy-2-methyl-2-E-butenyl-4-diphosphate reductase

ISPT – isopentenol

IUP - isopentenol utilization pathway

LB – lysogeny broth

LDH - lactate dehydrogenase

LOD – lactate oxidase

LPS - levopimaradiene synthase

MEC – 2-C-methyl-D-erythritol-2,4-cyclodiphosphate

MEP – 2-C-methyl-D-erythritol-4-phosphate

MPD - mevalonate phosphate decarboxylase

MVA – mevalonate

MVD - mevalonate diphosphate decarboxylase

MVK - mevalonate kinase

MVP - mevalonate-5-phosphate

MVPP - mevalonate-5-diphoshate

NADH – Reduced nicotinamide adenine dinucleotide

NADP - Nicotinamide adenine dinucleotide phosphate

NADPH - nicotinamide adenine dinucleotide phosphate

NHS - N-hydroxysuccinimide

NMR – nuclear magnetic resonance

NP - 4-nitrophenol

NTA - nitrilotriacetic acid

PAD - peptidyl arginine deiminase type 1

PBR – packed bed reactor

PC – polycarbonate

PCAF - acetyltransferase p300/CBP associated factor

PCR – polyerase chain reactions

PDMS – poly(dimethylsiloxane)

PEG – poly(ethylene glycol)

PEG-DA – poly(ethylene glycol) diacrylate

PEG-DE – poly(ethylene glycol) diglycidyl ether

PEG-MA – poly(ethylene glycol) methacrylate

PEI – polyethylenimine

PEP - phosphor(enol)pyruvate

PK – pyruvate kinase

PMK - phosphomevalonate kinase

PMMA – poly(methyl methacrylate)

PMMO – monooxygenase

PNPP - 4-nitrophenyl phosphate

POL – peroxidase

PPi – pyrophosphate

PPP - pentose phosphate pathway

PVA – poly(vinyl alcohol)

PVC – poly(vinyl chloride)

PYR – pyruvate

SAV – surface area to volume

SDS-PAGE - sodium dodecyl sulphate–polyacrylamide gel electrophoresis

STL - standard tessellation language

TA – transketolase

TBAP -tetrabutylammonium dihydrogenphosphate

TCAN – trichloroacetonitrile

TPM - (trichlorosilyl)propyl methacrylate

UV – ultraviolet

β -gal – β-galactosidase

β-NAD - β-nicotinamide adenine dinucleotide

ω-TA - ω-transaminase

List of Symbols

a – Surface to Volume ratio of reaction volume (m^2/m^3)

D_{ij} – Diffusivity coefficient of component i in solvent j (m^2/s)

$[E_{o,k}]$ – Initial concentration of enzyme k (µM)

F – Volume force vector (N/m^3)

I – Identity matrix (dimensionless)

$[i]$ – Concentration of species i (µM)

$[i]_0$ – Initial Concentration of species i (µM)

$J_{i,0}$ – Boundary molar flux rate of component i ($\mu mol/m^2 \cdot s$)

$k_{cat,k}$ – Turnover rate of enzyme k (1/s)

$K_{M,ki}$ – Binding affinity of enzyme k for substrate i (µM)

L – Length of the microfluidic reactor (m)

M_B – Molecular weight of solvent (kg/kmol)

n – Number of observations (dimensionless)

N – Outward pointing normal vector of the boundary (dimensionless)

P –Pressure (Pa)

P_0 – Inlet Pressure (Pa) (no tangential-stress condition)

$\widehat{P_0}$ – Inlet pressure (Pa) (adjusted tangential-stress condition)

R^2 – Coefficient of determination (dimensionless)

SE – Standard Error of the Mean (dimensionless)

SSE – Sum of squared estimates of error ($\mu M^2/s^2$)

SST – Total sum of squares ($\mu M^2/s^2$)

$[S_i]$ – Substrate concentration of component i (µM)

t – time (s)

T – Temperature (K)

T_M – Melting Temperature (K)

$\dot{t}$ – Critical t-distribution value (dimensionless)

u – Velocity vector (m/s)

$\bar{u}$ – Mean longitudinal velocity (m/s)

y – Longitudinal distance (m)

α – significance level (dimensionless)

δ – Ramping variable (dimensionless)

η_k – Immobilization Efficiency of enzyme k (dimensionless)

$\hat{\eta}$ –Mean normalized immobilization efficiency (dimensionless)

μ – Viscosity of solution (kg/m·s)

$\hat{\nu}$ – Normalized reaction rate (µmol/m^2·s)

$\bar{\nu}_{exp,k}$ – Average experimental rate of reaction (µM/s)

$\nu_{exp,k}$ – Experimental rate of reaction for enzyme k (µM/s)

$\nu_{pred,k}$ – Predicted rate of reaction for enzyme k (µM/s)

ρ – Fluid density (kg/m^3)

$\hat{v}_A$ – Solute molal volume at normal boiling point (m^3/kmol)

$\upsilon_{i,k}$ – Stoichiometic coefficient of species i for reaction k (dimensionless)

φ – Association factor for solvent (2.26 for water) (Dimensionless)

1. Review of 3D-Printed Cascade Immobilized Enzyme Microfluidic Reactors

1.1. Introduction

Enzyme cascade reactions are commonly used by cells for a variety of natural endogenous metabolic pathways. In nature, these pathways achieve high selectivity by avoiding by-product formation and utilizing metabolic regulation to keep reactant concentrations low. Although suitable for cell metabolism, native hosts often require metabolic engineering to achieve economically viable productivity levels at an industrial scale (Woolston et al., 2013). There are many review articles available outlining the metabolic engineering efforts to increase product yields and promote efficient cell regulation across a variety of fields (Pickens et al., 2011; Woolston et al., 2013; Lee et al., 2012; McNerney et al., 2015). Despite significant improvement over the past decades, *in vivo* cascade systems have several limitations such as undesirable side-reactions, growth inhibition due to the accumulation of toxic metabolites, central carbon metabolism competing with engineered pathways, diffusion limitations preventing efficient substrate/product transport, enzyme inhibition from internal cell metabolites, and the need for extensive metabolic engineering to balance pathway flux, enzyme inhibition, and central carbon metabolism (Muschiol et al., 2015; Erb et al., 2017).

Cell-free cascade systems alleviate the requirement for extensive metabolic engineering and prevent diffusion limitations from transcriptional and translational regulation, host toxicity, and competing endogenous pathways, allowing for higher productivity and theoretical yields (Dudley et al., 2015, Xue & Woodley, 2012). Enzyme concentrations are also easily controllable allowing for simplified optimization procedures without having to develop new metabolically engineered strains. Additionally, the use of enzyme immobilization enhances enzyme stability, reusability, allows for easy product recovery, and enables continuous operation (Sheldon & Woodley, 2018). Extension of single-enzyme immobilization to multi-enzyme cascade systems also has several advantages for a variety of applications such as product detection, co-factor regeneration, and the synthesis of *in vitro* metabolic pathway products. The use of sequential or co-immobilization enables several enzymatic steps to occur within one reactor allowing reactors to have smaller volumes, shorter residence times, less waste generation, and fewer purification steps than typically required for reactors in series (Muschiol et al., 2015; Sheldon & Woodley, 2018).

For efficient operation of cascade immobilized reactors, continuous-flow microfluidic devices are often used. The use of microfluidic reactors is ideal since they can be fabricated at micro-scale, offer high surface area to volume (SA:V) ratios which limit external diffusion limitations, require small reagent volumes reducing waste, and are easily scalable to industrial levels through scaling up or parallelization processes (Meller et al., 2017; Zhu et al., 2020). Microfluidic reactors have traditionally been fabricated from either glass which requires surface activation for enzyme immobilization and is costly to manufacture or poly(dimethylsiloxane)

(PDMS) which is commonly prepared using soft lithography, but requires several fabrication steps, is chemically incompatibility with many organic solvents, has low mechanical strength, poor temperature stability, and is limited to planar microreactor configurations (Faustino et al., 2016). Over the past several years, additive manufacturing and 3D-printing technologies have gained researcher attention as an increasingly viable alternative for microfluidic reactor fabrication.

There are many different types of additive manufacturing such as thermal bonding methods including material extrusion, powder bed fusion, fused deposition modelling (FDM), material jetting, and binder jetting, as well as ultraviolet (UV) photoinitiated polymerization methods such as stereolithography and digital light processing (DLP). Several review articles describing the different printing methods in detail are available in the literature (González-Henríquez et al., 2019; Ngo et al., 2018; Bikas et al., 2015). Additive manufacturing technologies utilize computer-aided design (CAD) modelling software and layer-by-layer printing which allows for highly customizable reactor designs at microscale resolution. The most common materials for 3D-printing are polymers such as poly(methyl methacrylate) (PMMA), nylon, acrylonitrile butadiene styrene (ABS), polycarbonate (PC), poly(ethylene glycol) diglycidyl ether (PEG-DA), and poly(vinyl chloride) (PVC). The use of additive manufacturing allows for highly customizable, cheap, and quick reactor fabrication which supports rapid prototyping and experimentation.

This review focuses on coupling the use of additive manufacturing with enzyme immobilization for the analysis of current literature studies relating to cascade immobilized enzyme microfluidic reactors. The topics reviewed include microfluidic reactor design, single enzyme immobilization methods suitable for 3D-printable supports, and cascade enzyme systems such as sequential and co-immobilization. Since the coupling of these topics is relatively new, the literature studies selected for analysis in this review often highlight the use of additive manufacturing, microfluidic reactor design, enzyme immobilization methods, or cascade enzyme reactors without directly coupling all the topics in tandem for the purpose of comparison. A summary of the current literature studies related to the discussion of 3D-printed cascade immobilized enzyme microfluidic reactors is presented below in Table 1.

Table 1: Summary of 3D-printable immobilization systems and cascade enzymatic studies.

Immobilization Type	Enzyme(s)	Support/Method	Performance	Reference
Adsorption	LOD	Surface activated ABS	Poor stability, activity decreased 60 % after one week of continuous operation	Su et al. (2016)
Covalent Bonding	GOD	Surface activated PMMA with PEI and GA crosslinking	Moderate stability, activity decreased 50 % after 21 days of discontinuous operation	Cerdeira Ferreira et al. (2013)
	GOD LOD	Surface activated ABS crosslinked with GA	Enzyme-specific immobilization procedure with GA enhancing GOD and inhibiting LOD immobilization	Su et al. (2016)
	HRP	Allyl glycidyl ether surface activated thiol-ene-epoxy†	Up to 81 % increased productivity for spatially distributed enzymes, strong correlation between experimental results and CFD model	Hoffmann et al. (2018)
	Trypsin	NHS surface activated polyester fleece with BSA spacers†	High stability, use of BSA spacer increased enzyme loading by 65 %, activity over 4-fold, and stability over 16-fold	Nouaimi et al. (2001)
	ω-TA	Acid hydrolyzed nylon microchannels crosslinked with GA and PEI	High activity, high stability after 105 catalytic cycles	Peris et al. (2017)
	ALP	EDC/NHS surface activated PC microchannels with PEI and PEG-DA spacers	High stability, increased productivity at high SA:V ratios from enhanced rates of substrate diffusion	Ogończyk et al. (2012)
	GOD, HRP	EDC surface activation of 3D-printed acrylic-based VeroClear	High operational control using temperature, pH, and high surface area enzyme modules	Kazenwadel et al. (2016)
	HRP INV, GOD, HRP	Grafting of PEG on methacrylate-based polymer monolith with azlactone functionalization	High stability, PEG spacer increased product yields over 7-fold, poor spatial distribution of sequentially immobilized enzymes	Logan et al. (2007)

Immobilization Type	Enzyme(s)	Support/Method	Performance	Reference
	CE, COD, POD	Acid hydrolysis surface activated PVC with glutaraldehyde crosslinking	High stability, retained 75.23 % activity relative to the enzymes free in solution	Chauhan & Pundir (2011)
	AAO CAT GOD, HRP	EN-DMSO surface activated PMMA microchannels with GA and PEI crosslinking	Intensive immobilization procedure optimization, enzyme-specific stability ranging from 100 % for CAT to only 25 % for GOD-HRP after 15 days operating	Cerqueira et al. (2015)
Affinity Binding	His-tagged TK	Direct AB-NTA binding to PMMA microchannel	Low stability, 15 % immobilization binding efficiency, only 4 % of free enzyme activity retained	Kulsharova et al. (2018)
	His-tagged GFP	Aminosilane surface activated PC with crosslinked GA, chitosan, and AB-NTA bonding	Immobilization procedure was suitable for a variety of supports, uneven spatial distribution of enzymes	Oshige et al. (2013)
	His-tagged C-P450	EDC/NHS surface activation of PMMA channel with optional AcBzTacn bonding	High stability, inconsistent continuous immobilization procedure with preference for binding near reactor inlet	Wollenburg et al. (2014)
	HaloTag PAD, SnapTag PCAF	Self assembled monolayer of alkanethiolates on gold absorbed to glass with selective phenylglyoxal bonding†	Use of different affinity binding tags prevented non-specific binding and allowed directional synthesis	Grant et al. (2018)
	HRP, GOD	Spatially distributed binding of DNA scaffolds to graphene oxide plates†	High stability, co-immobilized supports enhanced substrate channelling increasing enzymatic activity 1.8-fold relative to sequential immobilization and 3-fold relative to the free enzymes	Mathesh et al (2017)
	HRP, GOD	Spatially distributed binding to DNA origami tiles†	Substrate channeling enhanced enzymatic activity over 3-fold for enzyme spacing below 65 nm and over 15-fold for spacing below 20 nm relative to the free enzymes	Fu et al. (2012)

Immobilization Type	Enzyme(s)	Support/Method	Performance	Reference
	β-gal, HRP, GOD	Cationic dendronized polymer absorption to glass microchannels with biotin/avidin binding†	High stability, accurate spatial distribution of sequentially immobilized enzymes	Fornera et al. (2012)
	β-gal, HRP, GOD	Heparin surface activated PDMS/microspheres with biotin/avidin binding†	Product yield enhanced 2.5 to 3-fold for sequentially immobilized microspheres in a PBR and co-immobilized wall-coated microchannels respectively relative to co-immobilized microspheres in a PBR	Boehm et al. (2013)
Entrapment	Protease	Freeze-dried PVA monolithic microchannel (10-30 µm microstructures)†	Low stability, low selectivity, adding elbows to reactor design increased backpressure reducing substrate diffusion and causing lower yields	Nakagawa et al. (2014)
	ADH BFD β-gal	3D-printed PEG-DA hydrogel (photoinitiated)	High stability, low activity ranging from 6.0 % of free enzyme activity retention for β-gal up to 14.0 % for ADH, increased mass transfer limitations for high activity enzymes	Schmieg et al. (2019)
	PMMO	3D-printed PEG-DA based hydrogel (photoinitiated) microchannel	Retained 85 % activity relative to the enzyme free in solution, high enzyme loading ranging from 27-54 %	Blanchette et al. (2016)
	GOD, HRP ALP	3D-printed PEG-DA	Retained sequential enzyme activity during 3D-printing of complex geometries	Mandon et al. (2017)
	GOD, HRP (CNO nanosheets)	PEG-MA hydrogel (UV/chemical initiation)	Increased activity retention of 79 % for chemical-initiated polymerization relative to only 59 % for UV-initiated polymerization	Liao et al. (2015)
	GOD, HRP β-gal, HRP	PEG-DA hydrogel absorbed to TPM surface activated glass	High stability, GOD retained its activity 6-fold better than β-gal relative to the free enzymes	Heo & Crooks (2005)
	F_{ate}, F_{ald}, ADH	Alginate-Silica (ALG-SiO_2)†	High activity, high stability, increased methanol yields for co-immobilization than sequential immobilization	Xu et al. (2006)

†Denotes studies not applicable to 3D-printable supports.

1.2. Enzymatic Microfluidic Reactor Design

Microfluidic reactors are often used for laboratory studies since they promote efficient heat and mass transfer while only requiring small reagent quantities for continuous operation. This allows for low-cost preliminary experimentation before scaling to industrial levels through either scale up processes to design larger reactors or scaling out processes using several reactors in parallel. One of the main advantages characteristic of microfluidic reactors are high SA:V ratios which facilitate shorter substrate diffusion lengths and higher immobilized enzyme productivities (Meller et al., 2017). Microfluidic reactors are also convenient for the detection of many enzymatic products since they can be coupled in-line with low throughput chromatography, electrophoresis, spectrometry, or process control equipment (Wang et al., 2010; Kazenwadel et al., 2016; Peris et al., 2017). Using small reagent quantities also allows for increased process control and reduced risk of a runaway reaction when using thermophilic enzymes for systems involving unstable intermediate metabolites or exothermic reactions that may be hazardous to operate at large scale (Borovinskaya & Reschetilowski, 2012).

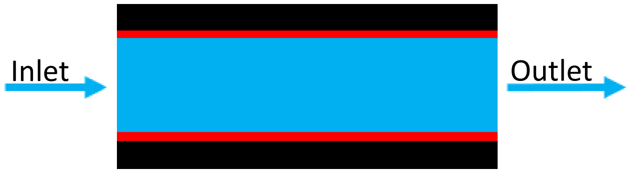

a) Open tubular (wall coated)

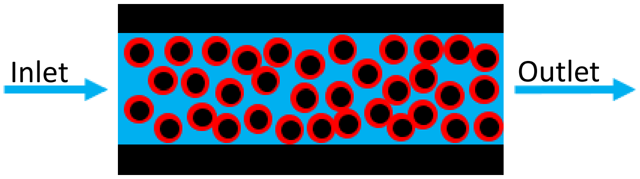

b) Packed bed

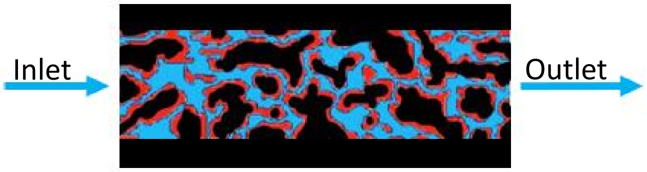

c) Monolithic

Figure 1: Schematic diagrams of a) open tubular (wall coated), b) packed bed, and c) monolithic immobilized enzyme microfluidic microchannels. Supports are coloured in black and enzymes in red.

There are several different types of immobilized microfluidic reactors such as open-tubular, monolithic, and packed bed reactors (PBR) as shown in Figure 1. Optimization of microfluidic reactors for increased productivity involves optimizing both enzyme kinetics and diffusional limitations. The former depends on operational variables such as pH, temperature, substrate concentrations, enzyme inhibition, and the selected immobilization procedure which can affect enzyme activity to various degrees depending on the chemical structures of the enzyme and support. The immobilization method, especially enzyme entrapment, can prevent the substrate from accessing the immobilized enzyme contributing significantly to internal diffusion limitations. Although internal diffusion limitations are critical and often rate-limiting, review of microfluidic reactor design will focus on geometric and operating considerations that affect external diffusion in the bulk solution since internal diffusion is highly dependant on the immobilization procedure selected and will therefore be discussed in the subsequent sections.

For reactors limited by external diffusion, the substrate often requires long residence times allowing for diffusion from the bulk solution to the immobilized enzyme surface. The adverse effects of slow external diffusion rates are further compounded when considering cascade enzyme systems which often require several diffusion steps between the bulk solution and the enzyme active sites as reaction intermediates are sequentially consumed. Although using narrow microchannels to reduce diffusion pathlengths and increasing the residence time of the substrate in the reactor by decreasing the flow rate or increasing the length of the reactor can overcome external diffusion limitations, the latter option results in large reactors with high turnover rates which limits industrial scalability (particularly through scale-up methods). Optimal microfluidic reactor design for immobilized cascade enzyme systems instead focuses on reducing the microchannel diameter to increase the SA:V ratio and reduce substrate diffusion pathlengths, reducing backpressure which decreases local substrate diffusion as pressure drop occurs, and identifying optimal enzyme spatial distributions.

Ogończyk et al. (2012) investigated substrate diffusion limitations for covalently immobilized alkaline phosphatase (ALP) by varying the cross-sectional area of open-tubular polycarbonate microreactors having equal reactor volumes (and residence times). Product formation was significantly enhanced for the microchannel reactors having the smallest cross-sectional area and correspondingly highest SA:V ratio due to reduced substrate diffusion paths between the bulk solution and immobilized enzymes at the surface of the microchannel walls (Ogończyk et al., 2012).

Nakagawa et al. (2014) entrapped protease in freeze-dried poly(vinyl alcohol) (PVA) monoliths within microfluidic channels to investigate proteolytic performance and product yields for different reactor configurations. The enzyme activity and corresponding product yields were found to vary with the magnitude of pressure drop throughout the microfluidic reactors. The channels having several elbows and high backpressure had relatively low product yields whereas the reactors with fewer or no elbows had reduced resistance to flow, and proportionally lower pressure drop which increased product yields by facilitating increased substrate diffusion (Nakagawa et al., 2014).

Hoffmann et al. (2018) investigated the affect of enzyme spatial distribution on reactor efficiency by covalently immobilizing horseradish peroxidase (HRP) in several patterns on a microchip reactor and using computational fluid dynamics (CFD) followed by experimental validation to determine the optimal enzyme distribution. As expected, the absolute product yield increased as more of the microchip surface was immobilized with enzyme, however specific product yields per unit area were 57 % and 78 % higher for coarse and fine checkerboard patterns when compared to the fully immobilized surface due to higher local substrate concentrations at the enzyme active sites (Hoffmann et al., 2018). Schäpper et al. (2011) also used topological optimization to enhance enzyme productivity for the modelling of immobilized whole cells from *Saccharomyces cerevisiae*. The optimal modelled reactor configuration featured large islands of immobilized whole cells which increased the predicted enzyme productivity 5-fold due to reduced metabolite inhibition and higher local substrate concentrations which enhanced the expected diffusion rates into the cells relative to using high enzyme loading with lower uniform substrate concentrations throughout the reactor (Schäpper et al., 2011). A trade-off exists between achieving high absolute product yields when using high enzyme loading and having correspondingly lower enzyme productivity throughout the reactor. Therefore, topological optimization of enzyme spatial distributions should be considered in tandem with the selection of the reactor type and size to prevent external substrate diffusion limitations and enhance mass transfer.

1.3. Types of Immobilization for 3D-Printed Supports

The procedure for enzyme immobilization is highly variable depending on many factors such as the enzyme and support chemistries, mass transfer limitations, and reagent compatibility.

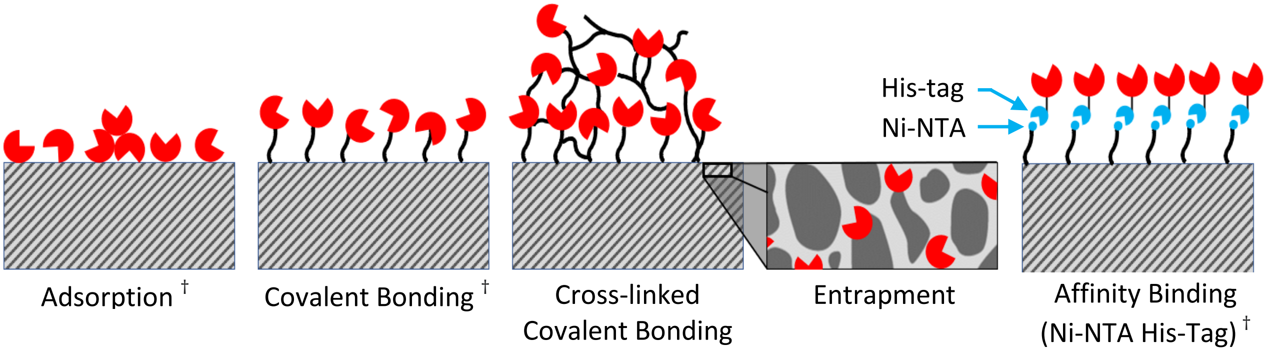

† Requires surface activation of 3D printed supports.

Figure 2: Example schematic representations of adsorption, covalent bonding, cross-linked covalent bonding, entrapment, and affinity binding (Ni-NTA his-tagged protein interaction). Enzymes are coloured red, 3D-printed supports grey, and Ni-NTA/His-tags blue.

For 3D-printed polymer-based supports, the types of immobilization can be classified based on their attachment mechanism of either adsorption, covalent bonding (including cross-linking), affinity binding, or entrapment as depicted schematically in Figure 2.

Table 2: Characteristics of different enzyme immobilization techniques for 3D printed supports.

Characteristics	**Adsorption**	**Covalent Bonding**	**Covalent Crosslinking**	**Affinity Binding**	**Entrapment**
Preparation:	Moderate	Extensive	Extensive	Extensive	Simple
Applicability:	Wide	Selective	Selective	Wide	Wide
Binding Force:	Weak	Moderate	Moderate	Strong	Strong
Stability:	Low	Moderate	Moderate	High	High
Enzyme Activity:	Moderate	Low	Low	High	Moderate
Enzyme Leakage:	High	Low	Low	Low	Low
Diffusion Limitations:	Moderate	Low	Moderate	Low	High

The advantages and disadvantages of each immobilization method are summarized in Table 2 based on important considerations such as applicability, stability, enzyme activity, and experimental preparation, among others. Although Table 2 provides a general characterization of each immobilization type, as will be discussed in the subsequent sections, each immobilized enzyme system is unique and often systems have varying performance for a given type or combination of immobilization types based on the enzymes, supports, and immobilization procedure used.

1.3.1. *Adsorption*

Physical adsorption is the simplest and most widely applicable immobilization method. It utilizes physical interactions such as van der Waals forces, hydrogen bonding, and hydrophobic interactions to adsorb enzymes to the support. The interactions are non-specific which often causes enzyme leakage due to relatively weak enzyme immobilization. Enzyme adsorption is typically sensitive to high substrate and product concentrations, ionic strength, and pH which reduce enzyme activity and contribute to increased product contamination (Zhu et al., 2020; Sheldon & Woodley, 2018). The random orientation of absorbed enzymes also introduces diffusion limitations caused by steric hinderances. This not only reduces the enzyme activity due to increased diffusion resistance but can also cause the enzyme active sites to become inaccessible if enzyme overloading occurs (Zhu et al., 2020). The typical advantages of physical adsorption are that the immobilization procedure is simple, enzyme adsorption is reversible allowing for support reuse, and no chemical modification of the support or enzymes is required. Although the latter is true of all supports, when using additive manufacturing to fabricate enzyme supports, chemical modification is often required since 3D-printed polymers are usually chemically inert resulting in very weak van der Waal interactions and poor enzyme absorption (Jesionowski et al., 2014). Crosslinked polymers commonly used for 3D-printing such as PMMA, PEG-DA, PC, Nylon, and ABS are chemically inert and have very little surface functionality which makes physical adsorption an unattractive immobilization method for 3D-printed supports since applying surface modification complicates the immobilization procedure and prevents the supports from being reused. Since these are two of the differentiating benefits of using adsorption, a better approach for supports requiring surface modification are immobilization methods such as covalent bonding or affinity binding which have increased stability, less diffusion limitations, and less enzyme leakage (Sheldon & Woodley, 2018).

1.3.2. *Covalent Bonding*

Covalent bonding is a non-specific immobilization method formed by the chemical reaction of enzyme functional groups with the surface of a support. Support selection is very important since there are many different surface and enzyme functionalities such as carboxyl, hydroxyl, aldehyde, amine, epoxy, sulfhydryl, succinimide, and azlactone groups (Zhu et al., 2020; Meller et al., 2017). Although varying enzyme and support functionality introduces the requirement for specific immobilization procedures and optimization, covalent bonding prevents enzyme leakage, has relatively high enzyme stability, and is suitable for a wide range of operating conditions (Sheldon & Woodley., 2018; Zhu et al., 2020).

An important consideration for covalent immobilization is the prevention of undesirable conformational changes, steric hinderances, and multi-point enzyme attachment which reduce activity by preventing access to the enzyme active site. Fortunately, these issues can be minimized by selecting suitable immobilization procedures. Deactivation of the enzyme active site by direct bonding with the support can be prevented by blocking the active site with a substrate or competitive inhibitor during the immobilization process. The use of spacers to increase the distance between the immobilized enzyme and its support can also be advantageous for maintaining high enzyme activity. Nouaimi et al. (2001) investigated the immobilization of trypsin on polyester fleece using different spacers and found that longer spacers minimized steric hinderances, increased stability, and allowed for increased enzyme loading. Compared to direct immobilization of trypsin on polyester fleece, the use of bovine serum albumin (BSA) spacers increased enzyme loading by 65 %, initial enzyme activity over 4-fold, and enzyme stability after one week over 16-fold (Nouaimi et al., 2001). Crosslinking agents such as glutaraldehyde (GA) have also been extensively used to increase enzyme loading and activity by increasing the functionality and surface area of the support (Peris et al., 2017; Cerqueira et al., 2015; Su et al. 2016).

The applicability of covalent bonding for a variety of enzyme and support functionalities coupled with the ability to improve the immobilization procedure with spacers and crosslinking agents makes covalent bonding a highly versatile immobilization method. One of the main drawbacks is the irreversible bonding of the enzyme to the support which prevents the support from being reused once enzyme deactivated occurs. This contributes significantly to the operating cost of the immobilized reactor especially at increased scale when using traditional reactors that are expensive to fabricate. Although reusability remains a drawback, additive manufacturing technologies provide an inexpensive solution for the fabrication of highly complex reactors requiring only surface modification to be applicable for covalent bonding enzyme immobilization.

Peris et al. (2017) used FDM 3D-printing to fabricate a continuous-flow reactor made of nylon for the immobilization of ω-transaminase (ω-TA). The immobilization procedure used GA to functionalize the support surface and promote crosslinking, coupled with polyethylenimine (PEI) to generate free amine groups for enzyme bonding. The immobilized ω-TA retained its activity after immobilization having a comparable productivity to the enzyme free in solution while also maintaining excellent stability for over 100 h of operation (Peris et al., 2017). Cerqueira et al. (2015) used a similar immobilization procedure with direct surface modification by ethylenediamine (EN) in dimethyl sulphoxide (DMSO) followed by GA and PEI crosslinking for the immobilization of various enzymes onto PMMA microchannels. Although the immobilization procedure was optimized for glucose oxidase (GOD) and applied to different enzymes, the stability of the immobilized reactors were highly enzyme-dependant ranging from 100 % retained enzyme activity for catalase (CAT), 71 % for ascorbate oxidase (AAO), and only 25 % retained enzymatic activity for co-immobilized GOD and HRP after 15 days of continuous operation (Cerqueira et al., 2015). Cerdeira Ferreira et al. (2013) also observed moderate enzyme stability retaining only 50 % of the initial enzyme activity after 21 days of operation for the optimized immobilization of GOD on PMMA microchannels using PEI and GA crosslinking.

Ogończyk et al. (2012) investigated the immobilization of ALP onto PC microchannels using direct surface modification with PEI and various covalently bound spacers. The use of poly(ethylene glycol) diglycidyl ether (PEG-DE) spacers significantly increased enzyme activity relative to direct immobilization via PEI surface modification, however in all cases (including when using enzyme blocking) the immobilized enzymes displayed poor activity presumably from undesirable enzyme-support bonding (Ogończyk et al., 2012). An alternative immobilization procedure utilizing 1-ethyl-3-(3-dimethylaminopropyl) carbodiimide (EDC) and N-hydroxysuccinimide (NHS) to first activate the PC surface and promote PEI crosslinking prior to enzyme bonding enhanced enzyme activity and greatly improved stability allowing for constant enzyme activity during 25 days of storage (Ogończyk et al., 2012). Kazenwadel et al. (2016) also demonstrated the potential use of EDC for the surface activation of VeroClear, a photoinitiated polymer similar to PMMA, during the direct bonding of GOD and HRP to the activated support surface.

Logan et al. (2007) reduced non-specific enzyme adsorption by utilizing a three-step immobilization procedure for the immobilization of HRP on a methacrylate-based polymer monolith. The immobilization procedure first modified the support surface using poly(ethylene glycol) (PEG) as a spacer, followed by covalent bonding of azlactone to functionalize the surface for subsequent enzyme bonding. After optimization of the immobilization procedure, the enzyme activity remained constant after several weeks of operation and the use of PEG to reduce undesirable enzyme-support interactions significantly increased the product yield over 7-fold (Logan et al., 2007). Additionally, the inclusion of a surfactant further prevented undesirable enzyme-support interactions resulting in an 18-fold product yield increase relative to the immobilized unmodified polymer monolith (Logan et al., 2007).

1.3.3. *Affinity Binding*

Affinity binding is an immobilization method that utilizes ligands to promote site specific enzyme binding. There are several types of affinity binding such as DNA-directed immobilization, halo/his-tag-metal binding, avidin-biotin, and antigen-antibody binding. For 3D-printable supports, his-tagged enzyme immobilization utilizing nitrilotriacetic acid (NTA) for binding is the most common method applied in the literature and so will be given focus in this section. His-tagged immobilization utilizes genetic engineering to tag polyhistine linkers to enzymes (typically at the N- or C- terminus away from the active site) which then bind via metal coordination with NTA immobilized on the enzyme support (Zhu et al., 2020). Although this immobilization method typically still requires surface modification and adsorption or covalent bonding to immobilize NTA to the support, it has several advantages unrealized by direct enzyme immobilization using covalent bonding. The first being that metal coordination binding allows for orientation-controlled enzyme immobilization which increases enzyme loading and enhances stability by preventing undesirable enzyme bonding (Jia et al., 2014). Additionally, the use of chemical treatments or changes in operating conditions such as pH or temperature often promotes reversible enzyme binding allowing for enzyme reloading and reactor reuse (Zhu et al., 2020). Although affinity binding is highly preferable relative to covalent bonding or adsorption for increased enzyme activity and stability, its application is often limited by its complexity. The requirement for genetic engineering to tag enzymes, followed by enzyme purification, and optimization of a multi-step immobilization procedure requiring surface modification and the immobilization of NTA to the support at minimum (or more likely to a spacer or crosslinking agent requiring additional steps) contributes significantly to the cost of immobilization. Despite this consideration, the use of affinity binding often has merit as an alternative to covalent bonding for enzymes prone to undesirable enzyme bonding and conformation changes despite its complexity. Additionally, as will be discussed in the subsequent sections, affinity binding is often preferable to covalent bonding for cascade enzyme immobilization since the immobilization procedure for a given support is the same for all enzymes which subsequently promotes similar enzyme stability relative to covalent bonding which can be highly variable if multiple different immobilization procedures are used.

Wollenberg et al. (2014) investigated the immobilization of his-tagged cytochrome-P4502C9 (C-P450) onto surface activated PMMA microchannels using N- and C- terminus attachment. The immobilization procedure used EDC and NHS for activation of the PMMA surface carboxylic groups, followed by direct amine bonding for N- terminus attachment, or covalent bonding of 1-Aceto-4-benzyltriazacyclononane (AcBzTacn) followed by his-tag chelation for C-terminus attachment (Wollenberg et al., 2014). Initial PMMA-chip immobilization experiments showed an approximately 3-fold increase in product formation when his-tagged C-terminus chelation was used, however immobilization in a bioreactor favoured covalent bonding via the N-terminus (Wollenberg et al., 2014). A possible explanation for this discrepancy is that fast flow-through enzyme immobilization coupled with long bioreactor flow paths promotes uneven enzyme immobilization, particularly near the entrance where enzyme concentrations are high which leads to overloading and reduced activity. This is a consequence of affinity binding as well as covalent bonding and adsorption immobilization procedures which all utilize a prefabricated support structure for immobilization (as opposed to simultaneous support fabrication and immobilization for entrapped enzymes) which reduces the probability of uniform enzyme immobilization when using continuous enzyme loading.

Oshige et al. (2013) developed a procedure applicable for the immobilization of his-tagged green fluorescent protein (GFP) on a variety of materials including PC supports. The immobilization procedure was rather complex requiring surface functionalization, multiple treatments with GA to promote crosslinking, and the covalent bonding of chitosan and N-(5-amino-1-carboxy-pentyl) iminodiacetic acid (AB-NTA). Despite being applicable for a variety of supports, the spatial distribution of the immobilized enzymes was uneven and support specific (Oshiege et al., 2013). Additionally, having such a laborious immobilization procedure contributes significantly to the cost of immobilization and may only be feasible at scale for particularly unstable enzyme systems.

Kulsharova et al. (2018) utilized the functionality of AB-NTA to develop a simplified one-step procedure for the immobilization of his-tagged transketolase (TA) to unmodified PMMA microchannels. This method was compared to an adapted multi-step procedure similar to Oshige et al. (2013) utilizing hexamethylene-diamine (HMDA) for PMMA surface modification followed by GA crosslinking and AB-NTA covalent bonding prior to his-tag enzyme immobilization. The simplified immobilization procedure had 30 % higher enzyme activity and comparable stability despite having slightly lower enzyme loading at 15 % compared to 26 % for the adapted multi-step procedure (Kulsharova et al., 2018).

1.3.4. *Entrapment*

Enzyme entrapment is a physical immobilization method that constrains the movement of enzymes within a matrix while allowing substrates, products, and cofactors to pass freely. Typically, enzyme supports such as organic and inorganic polymers or hydrogels are produced by adding the enzyme prior to polymerization (Sheldon & Woodley, 2018). Unlike sol-gel enzyme entrapment for soft lithographic materials such as PDMS that initiate polymerization chemically (Jones et al., 2002; Reetz et al., 1996), additive manufacturing processes rely on thermal reaction bonding or photoinitiation (González-Henríquez et al, 2019). The high temperatures required for thermal reaction bonding used in material extrusion, powder bed fusion, FDM, material jetting, and binder jetting are unsuitable for enzyme entrapment due to enzyme degradation at elevated temperatures. However, photoinitiation methods relating to stereolithography and DLP have been implemented successfully for enzyme entrapment (Schmieg et al., 2019; Mandon et al., 2017; Blanchette et al., 2016).

Physical entrapment is a fast and simple method applicable to both purified and whole cells for single or multi-enzyme immobilization. One of the main advantages of enzyme entrapment is that enzyme and support specific optimization are omitted. This makes it an ideal immobilization method for multi-enzyme systems of varying enzyme functionality since covalent bonding and affinity binding typically require intensive immobilization procedures. Physical entrapment also avoids enzyme deactivation from undesirable conformational changes commonly present for chemical immobilization methods and allows for higher enzyme loading. However, most of the active sites are inaccessible to convective flow and the process is highly dependant on internal diffusion rates (Zhu et al., 2020). This introduces significant mass transfer limitations for microfluidic reactors since the substrate and products must diffuse not only between the bulk solution and the polymer matrix surface, but also internally to the enzyme active site. Furthermore, there is the possibility of enzyme leakage causing product contamination. Therefore, appropriate polymer selection, pore size, and microfluidic reactor design are crucial for preventing mass transfer limitations and maintaining the activity of entrapped enzymes. The use of additive manufacturing provides a viable solution for controlling these parameters since the selection and material engineering of lithographic polymers is vast and the high resolution and customization of 3D-printing allows for enhanced design and control.

Schmieg et al. (2019) investigated the direct entrapment of β-galactosidase (β-gal), benzoylformate decarboxylase (BFD), and alcohol dehydrogenase (ADH) in a PEG-DA based hydrogel for the reaction of ortho-nitrophenyl-β-galactoside, benzaldehyde, and acetophenone/(S)-2-hydroxy-1-phenyl-propanone ([S]-HPP), respectively. Direct immobilization of β-gal during photoinitiated extrusion 3D-printing retained 6.9 % of the free enzyme activity, and manual immobilization of ADH and BFD using UV polymerization resulted in 8.9 % and 6.0 % retained activity, respectively (Schmieg et al., 2019). The most efficient immobilization process was for the slower reaction of ADH with (S)-HPP, a reaction cascade intermediate, which had an immobilization efficiency of 14.0 % (Schmieg et al., 2019). The results obtained for β-gal, BFD, and ADH entrapped in a PEG-DA matrix, support that reactions having a faster reaction rate (higher apparent reaction rate constant for a given enzyme concentration) have increased mass transfer limitations and lower immobilization efficiencies due to much of the substrate being consumed before diffusing to all the active sites throughout the polymer matrix.

Mandon et al. (2017) directly entrapped ALP and the cascade enzyme system of GOD and HRP in a PEG-DA based polymer matrix using DLP 3D-printing. The enzymes retained activity throughout the printing process and complex geometries at a resolution of 101.6 µm were able to be printed (Mandon et al., 2017). Furthermore, it was demonstrated that 3D-printing heterogenous structures having multiple spatially distributed enzymes for sequential immobilization systems was easily achievable by substituting different resins during printing (Mandon et al., 2017).

Blanchette et al. (2016) used stereolithography with a high printing resolution of 10-100 µm to polymerize a PEG-DA based hydrogel with embedded particulate methane monooxygenase (PMMO) for the synthesis of methanol in a 3D-printed continuous reactor. PMMO was loaded with 27-54 % efficiency and retained 85 % of its activity after immobilization despite relatively extensive UV exposure rates (Blanchette et al., 2016). By further optimizing the hydrogel printing process to have shorter exposure times and an increased hydrogel SA:V ratio of 2330 m^2/m^3, the enzyme activity surpassed those previously reported for immobilized PMMO with reduced nicotinamide adenine dinucleotide (NADH) as a reducing agent while still having a high loading efficiency (Blanchette et al., 2016). This demonstrates the use of stereolithography for direct enzyme entrapment as a viable option for maintaining enzyme activity during immobilization while also increasing enzyme reusability, printing high resolution tunable continuous reactors, and avoiding complex immobilization procedures.

1.4. Cascade Immobilized Enzyme Systems

Cascade immobilized enzyme systems apply the benefits of single-enzyme immobilization such as increased enzyme stability and reusability for use in multi-enzyme systems. This has a wide range of applications such as for cofactor regeneration, product detection, and cell-free product synthesis.

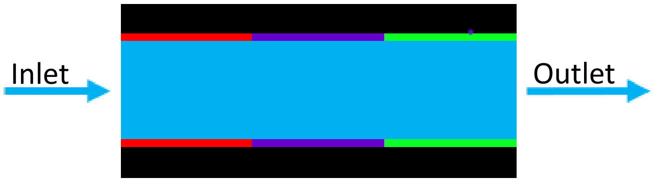

a) Sequential immobilization
(wall coated)

b) Co-immobilization
(wall coated)

Figure 3: Schematic diagrams of a) sequential immobilization (wall coated) and b) cascade immobilization (wall coated) microchannels. Supports are coloured in black and enzymes in red, purple, and green, respectively.

The two primarily methods of cascade enzyme immobilization depicted in Figure 3 are sequential immobilization which spatially distributes enzymes and co-immobilization which has a random distribution. One of the major advantages of immobilized enzyme cascades is that an entire metabolic pathway can be implemented, *in vitro*, within one reactor. This significantly reduces the reaction time, cost, and waste generation relative to single immobilized enzyme reactors in series which typically result in product loss and reduced yields due to intermediate product purification steps (Ji et al., 2016; Sheldon & Woodley, 2018). Additionally, the use of co-immobilization or sequential immobilization for different applications has the potential to enhance yields based on the advantages of the enzyme spatial distribution selected.

For co-immobilized systems, enzymes are co-localized in close proximity to one another which leads to an effect called substrate channeling. When enzymes in a cascade reaction are spatially distributed, the substrate must first diffuse from the bulk solution to the enzyme active site, form a product, and then diffuse back to the bulk solution for each enzymatic step in the cascade. However, when the enzymes are co-immobilized, the diffusion distance between enzymes may become small enough to facilitate substrate channelling which occurs when the product of an enzymatic reaction is transferred directly to the subsequent enzyme active site in the cascade without first diffusing to the bulk solution (Kazenwadel et al., 2015). This effect not only increases the rate of reaction by reducing substrate diffusion pathlengths, but also reduces undesirable reaction kinetics caused by product inhibition by consuming reaction intermediates rapidly. A study investigating the co-immobilization of GOD and HRP on graphene oxides using DNA scaffolds found that co-immobilization under conditions favourable for substrate channeling led to a 1.8 and 3-fold increase in enzymatic activity relative to sequentially immobilized and free enzyme systems, respectively (Methesh et al., 2017). Fu et al. (2012) investigated substrate channeling by adjusting the distance between co-immobilized GOD and HRP on DNA origami tiles. Substrate channelling significantly increased enzyme activity over 15-fold relative to the control at enzyme distances below 10 nm and approximately 3-fold relative to the control up to enzyme distances of 65 nm. However, the immobilization yield was consequently lower at enzymes distances of 10-20 nm due to steric hinderances preventing efficient enzyme loading (Fu et al., 2012). Prefacing the discussion of immobilization procedures for cascade systems it should be specified that for efficient substrate channeling to occur, the selected enzymes should have compatible immobilization procedures and operating conditions which promote concurrent co-immobilization of multiple enzymes. The immobilization methods which are unilaterally applicable for co-immobilization are affinity binding and entrapment which both omit enzyme specific optimization allowing for concurrent co-immobilization. However, simple covalently immobilized systems may also be applicable.

Alternative to the random spatial distribution of co-immobilization, sequential immobilization spatially distributes enzymes into individual compartments for stepwise catalysis of individual enzymatic steps. Although this increases the effects of substrate and product inhibition within individual reaction compartments, spatial distribution of the enzymes reduces inhibition from upstream metabolites and prevents undesirable side-reactions of intermediate products (Ji et al., 2016). Separation of enzymes into individual compartments also allows for local optimization of process operating conditions such as temperature and pH for optimal enzyme activity between compartments which is not possible for co-immobilized enzymes operating under the same conditions. Additionally, enzyme activity and stability are easily quantifiable for sequentially immobilized enzymes whereas the effects of substrate channeling for co-immobilized systems is often implicit.

Optimization of enzyme cascade systems free in solution requires selection of optimal operating conditions promoting high activity for enzymes, followed by experimentation and kinetic analysis to determine the optimal concentration of each enzyme. The same is true for immobilized cascade systems. The enzyme loading concentrations at optimal operating conditions should be balanced so that the catalytic rate of each enzyme is equal (Ji et al., 2016). This improves the catalytic efficiency of the cascade by adjusting each enzymatic rate to the rate-limiting step and prevents the accumulation of intermediate metabolites. Although simply an extension of single-enzyme immobilization and easily optimized to promote initial catalytic efficiency, multi-enzyme immobilized systems are often severely limited in their application due to incompatible or impractical immobilization procedures and unequal stability between sequential enzymes which creates reaction bottlenecks.

Evident of the current limitations in the field of cascade immobilized enzyme systems, the most common method for enzyme attachment in the literature is covalent bonding and is typically only applied to 2- or 3-enzyme cascade systems. Although excellent enzyme loading and product yields are often obtained for applicable enzyme systems having similar immobilization procedures and stability, extension to include enzyme systems having varying enzyme functionality requiring several immobilization procedures is often problematic. Logan et al. (2007) used a multi-step procedure to sequentially immobilize invertase (INV), GOD, and HRP by covalent bonding to a methacrylate-based polymer monolith for kinetic studies. The enzymes had high stability showing no significant change in activity after several weeks of operation, however directional synthesis studies varying the enzyme order within the reactor showed significant product formation for the non-sequential cases which suggests that the immobilization procedure was inefficient at spatially distributing the enzymes (Logan et al., 2007).

Chauhan and Pundir (2011) covalently co-immobilized cholesterol esterase (CE), cholesterol oxidase (COD), and peroxidase (POD) on surface functionalized PVC using GA crosslinking. The enzymes retained 75.23 % of their initial activity when immobilized and showed excellent stability having a half-life of 100 days before reducing 50 % in enzyme activity (Chauhan and Pundir, 2011). The implemented cascade system was highly suitable for serum cholesterol determination without extensive optimization demonstrating the potential of covalent immobilization for simple cascade systems having similar immobilization procedures.

Su et al. (2016) immobilized GOD and lactate oxidase (LOD) onto FDM 3D-printed ABS bioreactors using GA for crosslinking. The immobilization of GOD was enhanced by GA resulting in constant enzyme activity lasting 42 days, whereas LOD immobilization was hindered by GA preventing efficient cascade immobilization (Su et al., 2016). Instead, direct immobilization of LOD onto the ABS surface was used which resulted in low enzyme stability reducing 60 % from the initial enzyme activity in only one week despite optimization of the immobilization procedure (Su et al., 2016). This exemplary study outlines several of the common problems associated with covalently immobilized cascade enzymatic systems. The first being that enzymes of differing functionality often require very different immobilization procedures which makes optimization and implementation of immobilization procedures tedious and more suitable for reactors in series than a cascade enzymatic reactor. This is further justified when considering that co-immobilization is unsuitable for incompatible immobilization procedures and sequential immobilization creates significant bottlenecks if the enzyme stability between adjacent enzyme compartments is dissimilar. These considerations in tandem with the inability to reuse the enzyme supports, non-specific bonding leading to undesirable enzyme conformations and inactivation, and often the requirement for spacers and crosslinking to improve activity makes cascade covalent immobilization impractical for many cascade systems beyond simple 2- or 3-enzyme systems where the compatibility of the immobilization procedure is less likely to be a limiting constraint. Immobilization by affinity binding or entrapment are better alternatives for co-immobilization and sequential immobilization since they omit enzyme-specific optimization allowing for any number of enzymes to be efficiently immobilized. However, these cascade immobilization methods are yet to garner significant researcher attention relating to 3D-printable supports. As such, the benefits and potential issues of affinity binding and entrapment cascade enzyme systems will be covered more generally by analyzing traditional enzyme supports and comparing with the review of single-enzyme affinity binding and entrapped enzyme systems made in the previous sections.

Fornera et al. (2012) sequentially immobilized β-gal, GOD, and HRP onto a cationic dendronized polymer adsorbed to glass microchannels using biotin-avidin affinity binding. The specific enzyme binding of biotin-avidin immobilization was ideal for ensuring enzyme compartmentalization and retention of enzyme activity for several weeks (Fornera et al., 2012). Using the same enzymes with biotin-avidin affinity binding onto PDMS, Boehm et al. (2013) investigated the performance of co-immobilized microspheres in a PBR, sequentially immobilized, single-enzyme, microspheres in a PBR, and co-immobilized enzymes on the walls of a microfluidic reactor. The results showed a 2.5-fold increase in the product yield of the sequentially immobilized enzymes relative to the co-immobilized microspheres (Boehm et al., 2013). Although co-immobilized microspheres enable substrate channeling and are expected to have a higher productivity than sequentially immobilized microspheres, the results suggest that the adjacent co-immobilized enzymes were either spaced too far apart for substrate channeling to be significant or the bottleneck due to the rate-limiting GOD kinetics prevented much of the downstream immobilized HRP from coming in contact with its substrate. Of the three enzyme configurations tested, co-immobilization on the microchannel walls had the highest product yields almost 3-fold higher than the co-immobilized microspheres, however the productivity was substantially lower than both the sequential and co-immobilized microspheres due to the requirement for high enzyme loading rates as a result of reduced surface area for reaction (Boehm et al., 2013).

Grant et al. (2018) sequentially immobilized peptidyl arginine deiminase type 1 (PAD) and acetyltransferase p300/CBP associated factor (PCAF) onto a maleimide functionalized microfluidic chip using engineered HaloTag and SnapTag affinity binding, respectively. The use of different affinity binding methods allowed efficient enzyme compartmentalization and operation of the reactor in the forward and reverse directions to change the enzyme ordering and produce different product compositions as a result of PAD-dependant cross-talking (Grant et al., 2018).

Although affinity binding has been demonstrated for a variety of cascade systems and is compatible for enzymes of different functionality, its practical application is often limited by expensive, labour intensive immobilization procedures. The most applicable method to couple with additive manufacturing for cascade enzyme immobilization is entrapment due to its simplicity and favourable immobilization characteristics. Entrapment not only benefits from the rapid prototyping and customizability of additive manufacturing technologies but allows for concurrent reactor fabrication and immobilization. Additionally, undesirable enzyme conformations are prevented and the limitations of covalent bonding and affinity binding such as complex or labour-intensive immobilization procedures and optimization are avoided. Direct enzyme entrapment using 3D-printing has been implemented successfully for single enzyme systems (Schmieg et al., 2019; Blanchette et al., 2016) and are extendable for both co-immobilization and sequential immobilization without the need for complex immobilization procedures. However, to date cascade enzyme immobilization coupled with additive manufacturing has only been implemented as a proof of concept (Mandon et al., 2017). As such, current enzyme cascade systems using soft lithography and other traditional reactor fabrication methods will be reviewed to outline the potential benefits of cascade enzyme entrapment more generally.

Heo & Crooks (2005) entrapped GOD/β-gal and HRP in PEG-DA based hydrogels adsorbed to 3-(Trichlorosilyl)propyl methacrylate (TPM) surface activated glass for the detection of glucose and galactose within microfluidic channels. The co-immobilized GOD and HRP system maintained high stability over the course of 8 days and retained its initial activity 6-fold better than when β-gal was co-immobilized with HRP (Heo and Crooks, 2005). The observation of enzymes having different immobilization efficiencies despite the same immobilization procedure is common for entrapment due to microenvironmental differences relating to the enzyme and support properties and substrate/product diffusion (Schmieg et al., 2019).

Xu et al. (2006) investigated the sequential and co-immobilization entrapment of formate dehydrogenase ($F_{ate}DH$), formaldehyde dehydrogenase ($F_{ald}DH$), and ADH in an alginate-silica gel for the synthesis of methanol. Co-immobilization of the enzymes on support beads enhanced substrate channeling resulting in significantly higher yields than when sequential immobilization on individual beads was used (Xu et al., 2006). Additionally, the co-immobilized enzyme system had high stability retaining 76.2 % of its initial enzyme activity after 60 days of storage and had comparable yields to the enzymes free in solution (Xu et al., 2006).

Liao et al. (2015) investigated the co-immobilization of GOD and HRP nanocomposite, calcium niobate (CNO), nanosheets to produce poly(ethylene glycol) methacrylate (PEG-MA) based nanocomposite hydrogels by both chemical and UV polymerization for the synthesis of purpurogallin. Immobilization using high-exposure (1 h) UV-initiated polymerization caused significant enzyme deactivation with the immobilized enzymes retaining only 59 % activity, compared to 79 % for chemical polymerization (Liao et al., 2015). The use of high-resolution additive manufacturing for direct enzyme entrapment has the potential to greatly reduce UV catalyzed enzyme deactivation by reducing UV exposure times from those on the scale of hours for soft lithography and other photoinitiated polymerization processes to values typically less than 30 s required for stereolithography and DLP (Schmieg et al., 2019; Mandon et al., 2017; Blanchette et al., 2016).

1.5. Summary and Outlook

Enzyme cascade reactions are important in nature for a variety of regulatory cell processes and endogenous metabolic pathways. Over the past decades, advancements in metabolic engineering have significantly increased pathway productivity for a variety of applications such as product synthesis, cofactor regeneration, and product detection. However, *in vivo* enzyme cascades often require extensive metabolic engineering efforts and are limited by growth inhibition from toxic metabolite accumulation, reduced yields due to competing endogenous pathways and central carbon metabolism, and transcriptional/translational regulation. Cascade immobilized enzymatic 3D-printed microfluidic reactors not only alleviate the limitations of *in vivo* systems, but also couples the advantages of 3D-printed microfluidic reactors such as quick, cheap, high SA:V ratio, scalable, and customizable polymer supports with enzyme immobilization for continuous operation, and enhanced stability, reusability, and product recovery. In this review, the design of enzymatic microfluidic reactors, enzyme immobilization by absorption, covalent bonding, affinity binding, and entrapment, and cascade immobilization methods including co-immobilization and sequential immobilization have been analyzed to summarize the current studies and future applications of additive manufacturing for cascade immobilized enzymatic microfluidic reactors.

Supplementary to the benefits of enzyme immobilization such as increased stability and reusability, the use of microfluidic reactors allows for smaller reactor volumes, shorter residence times, less waste generation, and fewer intermediate purification steps relative to reactors in series. For a given enzyme spatial distribution, immobilization method, and reactor configuration such as open-tubular, PBR, or monolithic, optimal microfluidic reactor design adjusts enzyme concentrations to balance the catalytic rate of sequential enzymatic steps preventing bottlenecks, utilizes a high reactor SA:V ratio, and minimizes backpressure to design a kinetically-limited system without external diffusion limitations (Ogończyk et al., 2012; Nakagawa et al., 2014). Although identifying optimal enzyme spatial distributions requires modelling or trial and error experimentation, its effects are secondary to the selected immobilization procedure which has a significant effect on enzyme activity, stability, spatial distribution precision, and internal diffusion limitations.

Although the performance of immobilized enzyme systems are highly dependant on the type of immobilization and selected enzymes/supports, a summary of the studies reviewed in Table 1 provides an objective overview of each immobilization method. Easily coupled with additive manufacturing, enzyme entrapment by stereolithography or DLP is a fast and simple immobilization method that omits enzyme and support specific optimization and prevents undesirable enzyme bonding and degradation. Since most enzyme active sites are inaccessible to convective flow, entrapment is limited by internal diffusion dependant on the specific enzyme, supports, and substrates selected (Heo & Crooks, Schmieg et al., 2018). The entrapment of β-gal, BFD, and ADH in a PEG-DA matrix demonstrated increased internal mass transfer limitations for faster reaction kinetics (Schmieg et al., 2018) and the entrapment of PMMO in a high SA:V ratio PEG-DA based hydrogel resulted in the highest reported membrane bound PMMO activity with NADH as a reducing agent (Blanchette et al., 2016). Although affinity binding requires surface activation for use with 3D-printable supports and often requires complex and labour-intensive immobilization procedure optimization, enzyme specific optimization is omitted and the controlled orientation of the immobilized enzymes results in high activity and stability (Kulsharova et al., 2018; Wollenburg et al., 2014). In addition to being irreversibly bound and requiring surface activation for 3D-printable supports, covalent bonding is often less consistent than entrapment and affinity binding due to non-specific bonding and steric hinderances. Several studies have utilized covalent bonding for high enzyme activity/stability (Peris et al., 2017; Ogończyk et al., 2012; Logan et al., 2007; Chauhan & Pundir, 2011) and the use of spacers (Nouamini et al., 2001) and crosslinking (Peris et al., 2017; Cerqueira et al., 2015; Su et al., 2016) have been shown to significantly enhance enzyme activity. However, the stability of covalently bonded enzymes remains highly enzyme dependant and requires optimization of the immobilization procedure (Cerqueira et al., 2015; Su et al., 2016; Cerdeira et al., 2013). Due to the requirement for surface activation, weak, non-specific enzyme immobilization, leakage, potential diffusion limitations, and poor stability (Su et al., 2016), adsorption is generally unpreferable for 3D-printable supports.

For cascade immobilized enzyme microfluidic reactors, the spatial distribution and selection of either co-immobilization which requires similar immobilization procedures, reduces product inhibition, and promotes substrate channeling due to reduced diffusion pathlengths (Methesh et al., 2017; Fu et al., 2012; Xu et al., 2006) or sequential immobilization which reduces inhibition from upstream metabolites, prevents undesirable side reactions, and allows for local compartmental optimization of operating conditions can have a large effect on performance. Although high activity and stability for covalently immobilized cascade systems have been observed (Chauhan & Pundir, 2011; Logan et al., 2007), sequential immobilization of INV, GOD, and HRP displayed poor enzyme spatial distribution when sequentially immobilized (Logan et al., 2007) and covalent bonding is typically only applied for 2-3 enzyme cascade systems due to incompatible immobilization procedures (particularly for co-immobilization). More suitable for cascade enzyme immobilization, affinity binding has been implemented successfully for sequential, spatially distributed (Grant et al., 2018; Fornera et al., 2012) and co-immobilized systems (Boehm et al., 2013), respectively. Similarly, entrapment has been successfully implemented for co-immobilized systems having high enzymatic activity (Xu et al., 2016; Liao et al. 2015) and as a proof-of-concept for simultaneously 3D-printed, sequentially immobilized, GOD and HRP in a PEG-DA hydrogel (Mandon et al., 2017).

Overall, current research has demonstrated the applicability and benefits of coupling additive manufacturing with enzyme immobilization for the development of highly customizable microfluidic reactors using a variety of immobilization methods. For 3D-printable supports, past research has primarily focused on simple, 2-3 enzyme, covalently immobilized systems which have limited scope and applicability. Although additive manufacturing does not fundamentally enhance affinity binding immobilization methods beyond the advantages relating to microfluidic reactor design, affinity binding immobilization procedures have been identified as having high activity, stability, good enzyme spatial distribution, and applicability for both co-immobilization and sequential immobilization with its only limitations relating to its cost and complexity. Most significant for the future outlook of 3D-printed cascade enzyme microfluidic reactors, developments in stereolithography and DLP have enabled simple and cheap simultaneous enzyme entrapment during reactor fabrication resulting in reduced enzyme degradation, high stability, and the ability for spatially distributed enzyme systems which have traditionally been impractical for soft lithographic entrapment immobilization methods. As the relevance of additive manufacturing technologies continues emerging as the new standard for microfluidic reactor fabrication, the field of cascade immobilized enzyme systems is expected to benefit as researcher focus shifts towards the promising outlook of affinity binding and entrapment for non-specific cascade enzyme immobilization.

2. Review of Isoprenoid Synthesis

2.1. Introduction

Isoprenoids are a large class of over 50,000 natural compounds, having significant industrial applications in a variety of fields including medicine, agriculture, cosmetics, and nutrition (Chandran et al., 2011). Some examples include artemisinin derived from amorphadiene, an anti-malaria drug; Taxol derived from taxadiene, an anti-carcinogenic drug used against cancer; farnesene, a precursor to renewable biofuels; and limonene, an insecticide, food additive, and anti-cancer agent (Chandran et al., 2011; Vickers et al., 2014). Despite their diversity, natural isoprenoids are all produced from two C_5 isomeric precursors, isopentenyl dIspHosphate (IPP) and dimethyl allyl diphosphate (DMAPP).

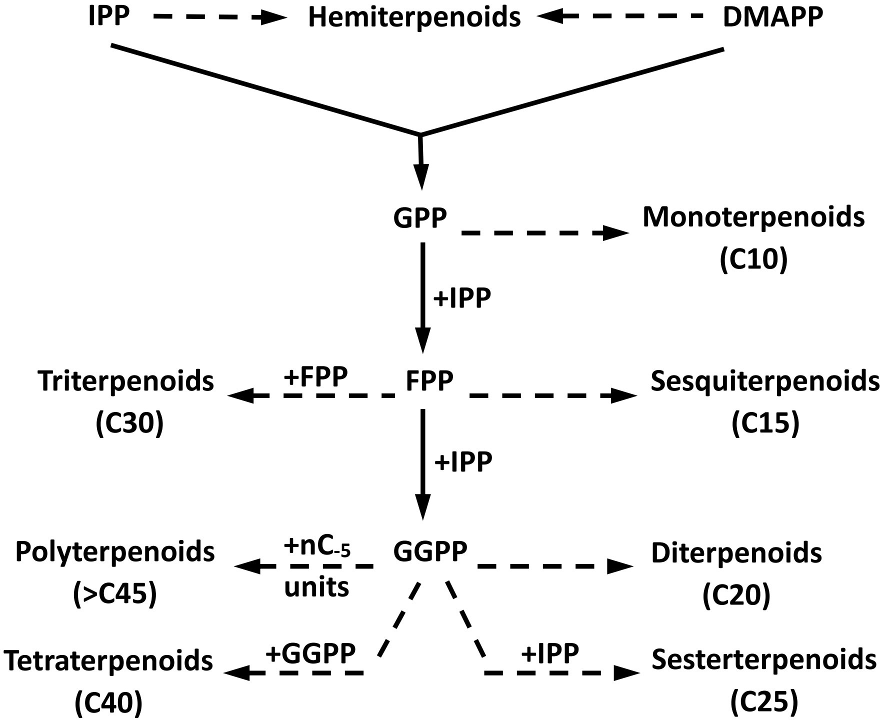

Figure 4: Terpene backbone synthesis of various isoprenoid classes.

These precursors can be used to form hemiterpenoids (C5) or larger isoprenoids via intermediates geranyl diphosphate (GPP), farnesyl diphosphate (FPP), and geranyl geranyl dIspHosphate (GGPP) which form the terpenoid backbone of larger isoprenoids as shown in Figure 4. The other families of isoprenoids include monoterpenoids (C10) produced from GPP, sesquiterpenoids (C15) and triterpenoids (C30) produced from FPP, and diterpenoids (C20), sesterterpenoids (C25), tetraterpenoids (C40), and polyterpenoids (<C45) produced from GGPP.

Isoprenoids are naturally produced in plants and are responsible for a variety of functions including pollinator attraction, herbivore repellent, pathogen resistance, and endogenous signalling (Vickers et al., 2014). Although plants produce a variety of high-value isoprenoids, they are not abundant and so natural procurement and recovery is often insufficient for industrial use (Vickers et al., 2014). Instead, isoprenoids are typically produced using metabolic engineering techniques such as enzyme overexpression, promoter engineering, endogenous control deregulation, and pathway manipulation to increase isoprenoid flux in microorganisms.

The two most common naturally occurring pathways for isoprenoid synthesis are the mevalonate (MVA) and methylerythritol phosphate (MEP) pathways which can be found in a variety of organisms such as eukaryotes, bacteria, and plants (Chandran et al., 2011). Over the past 20 years, metabolic engineering efforts have focused on increasing flux through the non-native MVA and native MEP pathways primarily in *Escherichia coli*. Significant improvements upwards of 15,000-fold relative to wild-type isoprenoid synthesis have been made (Ajikumar et al., 2010), however issues relating to enzyme inhibition, host toxicity, expensive cell-free synthesis, and competing endogenous pathways remain a challenge. Recently the development of the synthetic isopentenol utilization pathway (IUP) has shown significant promise for both *in vivo* and cell-free synthesis due to its simplicity and decoupling from central carbon metabolism (Chatzivasileiou et al., 2019). Research relating to isoprenoid synthesis has typically focused on the upstream supply of isoprenoid precursors, IPP and DMAPP, however removing this bottleneck would allow future engineering efforts to focus on downstream terpenoid backbone and product synthesis which are often equally challenging.

2.2. The MVA Pathway

The MVA pathway exclusively produces isoprenoids in archaea, as well as many bacteria and eukaryotes (Chandran et al., 2011). It is also found in plants which have both the MVA and MEP pathways. The MVA pathway is found in the cytosol of plants and primarily produces FPP, sesquiterpenes, triterpenes, and C_{11} homoterpenes (Vickers et al., 2014).

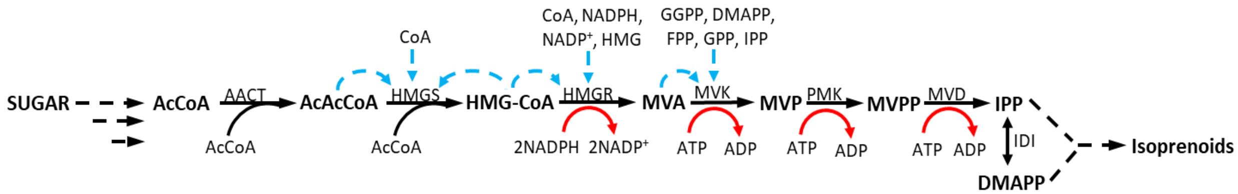

Figure 5: The MVA pathway for isoprenoid synthesis.

As depicted in Figure 5, acetyl coenzyme A (AcCoA) produced from the oxidation of pyruvate (PYR) in the glycolysis pathway undergoes a seven-step reaction to produce IPP and DMAPP in the MVA pathway. The reactions require both adenosine triphosphate (ATP) and reduced nicotinamide adenine dinucleotide phosphate (NADPH) as cofactors. In the first steps of the reaction two AcCoA molecules undergo condensation catalyzed by acetoacetyl-coenzyme A thiolase (AACT) to produce acetoacetyl-coenzyme A (AcAcCoA) which then undergoes subsequent condensation with AcCoA catalyzed by 3-hydroxy-3-methylglutaryl-coenzyme A synthase (HMGS) to produce 3-hydroxy-3-methylglutaryl-coenzyme A (HMG-CoA). The reaction is then catalyzed by 3-hydroxy-3-methylglutaryl-CoA reductase (HMGR) to produce MVA, before undergoing two sequential phosphorylation reactions catalyzed by mevalonate kinase (MVK) and phosphomevalonate kinase (PMK) to produce mevalonate-5-phosphate (MVP) and mevalonate-5-diphoshate (MVPP), respectively. In the final steps of the pathway, mevalonate diphosphate decarboxylase (MVD) catalyses the decarboxylation of MVPP to produce IPP. DMAPP is then produced using isopentenyl dIspHosphate isomerase (IDI) to catalyze the isomerization of IPP to DMAPP.

Over the past decades metabolic engineering has focused on improving the MVA pathway for isoprenoid synthesis by reducing enzyme inhibition, by-passing endogenous regulation, overexpressing cell genes, and identifying sources of toxicity causing cell growth inhibition. One of the main enzymatic regulators in the MVA pathway is HMGS which is inhibited by both its substrate AcAcCoA and its products HMG-CoA and free coenzyme A (CoA) (Nagegowda et al. 2004; Bach et al., 1986). HMGR has also shown to be inhibited by free CoA, as well as 3-hydroxy-3-methylglutaric acid (HMG) to a lesser degree with 50 % enzyme inhibition occurring at a concentration of 0.5 mM and 3 mM for free CoA and HMG, respectively (Brooker & Russel, 1975). More problematic for metabolic engineering efforts is the competitive inhibition of HMGR by cofactor NADPH and substrate inhibition of HMG-CoA by nicotinamide adenine dinucleotide phosphate (NADP) (Bach et al., 1986). If HMGR activity is too low, HMG-CoA accumulation occurs which is toxic in *E. coli* (Pitera et al., 2007), but overexpression of HMGR is equally problematic since increasing the cofactor requirement of NADPH can cause competition with essential anabolic pathways necessary for cell growth (Chen et al., 2015). Additionally, NADPH is unstable when used for *in vitro* synthesis and is uneconomical to feed continuously to meet cofactor requirements (Dudley et al., 2015; Zhang, 2011). These considerations make the MVA pathway, and particularly the HMGR bottleneck, highly complex since there are many sources of enzyme inhibition and several metabolic control systems that may affect pathway flux and implementation of *in vivo* cofactor regeneration.

Another bottleneck in the MVA pathway is MVK which is competitively inhibited at the ATP-binding site by GGPP, FPP, GPP, IPP, and DMAPP (in relative order with GGPP being the most inhibitory) (Redding-Johanson et al., 2011; Voynova et al., 2004; Hinson et al., 1997). There is also substrate inhibition caused by MVA with the inhibition of MVK from *Staphylococcus aureus* becoming apparent at MVA concentrations upwards of 0.5 mM (Voynova et al., 2004). Cell growth inhibition in *E. coli* was also observed when the concentration of MVA exceeded 40 mM (Morrone et al., 2010). Similar to the first phosphorylation reaction involving MVK, the second phosphorylation reaction was also identified as a bottleneck by proteomics (Redding-Johanson et al., 2011). Lastly the accumulation of IPP in engineered *E. coli* strains at concentrations above

40 mM have been shown to inhibit cell growth, reduce PMK production, and slow endogenous metabolic functions such as ATP regeneration (George et al., 2018; Martin et al., 2003).

Many recent research developments in metabolic engineering have substantially improved isoprenoid production in *E. coli* via the MVA pathway. Willrodt et al. (2014) identified that endogenous FPP synthase production in recombinant *E. coli* did not hinder monoterpene synthesis and instead production was limited by the availability of upstream IPP and DMAPP precursors. Reacting glycerol in two 3.1 L bioreactors to produce limonene via the MVA pathway resulted in high titres of 2700 mg/L, however the productivity was approximately 40 mg/L·h which is below the minimum, generally accepted, industrial profitability threshold of 100 mg/L·h for fine chemicals (Willrodt et al., 2014; Straathof et al., 2002).

Martin et al. (2003) engineered the MVA pathway from *S. cereviseae* into *E. coli* to avoid issues relating to metabolic regulation. Since the MVA pathway is not native to *E. coli* (Boronat & Rodríguez-Concepción, 2015), overexpression of the engineered pMevT and pMBIS plasmids, responsible for the reactions of AcCoA to MVA and MVA to FPP respectively, were able to produce an increased artemisinin yield of 24 mg β-caryophyllene equivalent/L with minimal optimization (Martin et al., 2003).

Morrone et al. (2010) used an engineered plasmid pMBI, analogous to pMBIS, to produce IPP and DMAPP from MVA. By overexpressing the pMBI plasmid from *S. cereviseae* in *E. coli* similar to Martin et al. (2003), yields upwards of 200 mg/L of abietadiene were obtained using a bioreactor in combination with MVA feeding. Comparing this engineered pathway using MVA feeding to the full MVA pathway encoded by the pMevT and pMBI plasmids cultivated in shake flasks, abietadiene yields were significantly reduced from 51.5 mg/L to 12.0 mg/L (Morrone et al., 2010). Incorporation of an additional truncated HMGR gene, as shown by Pitera et al. (2007) to eliminate the HMGR bottleneck, slightly improved yields of the full MVA pathway from 12.0 mg/L to 22.3 mg/L, however it remained lower than the bottom-operon MVA pathway with MVA feeding (Morrone et al., 2010). It is apparent that the use of bioreactors with high substrate levels can significantly increase isoprenoid yields, however due to the cost of MVA supplementation, using a bottom-operon MVA pathway is impractical at industrial scale despite having increased yields relative to the full MVA pathway.

Newman et al. (2006) used a recombinant *E. coli* strain similar to Martin et al. (2003) that was engineered to have the full MVA pathway from *S. cereviseae* encoded by the pMevT and pMBIS plasmids. Additionally, a pADS plasmid for amorphadiene synthesis was included. Increasing substrate levels using a 10 L bioreactor resulted in a 20-fold increase in the yield of amorphadiene to 480 mg/L (Newman et al., 2006). Redding-Johanson et al. (2011) obtained high amorphadiene titres by using proteomics to identify MK and PMK from *S. cereviseae* as bottlenecks in recombinant *E. coli* which resulted in titres upwards of 500 mg/L after codon-optimization. High amorphadiene titers of 27.4 g/L were also obtained by implementing the MVA pathway in recombinant *E. coli* and supplementing known HMGS and HMGR bottlenecks

(Nagegowda et al. 2004; Bach et al., 1986; Pitera et al., 2007) with equivalent genes from *S. aureus* and controlling down-regulation by ammonia in a 2.0 L bioreactor (Tsuruta et al., 2009). Recently Shukal et al. (2019) used transcriptional, translational, and strain engineering to develop an autotropic *E. coli* capable of producing 375 mg/L·h of amorphadiene in a 250 mL fed-batch bioreactor via the MVA pathway. Instead of using recombinant *E. coli* having genes from *S. cereviseae*, Ro et al. (2006) and Westfall et al. (2012) engineered the native MVA pathway in *S. cereviseae* directly and were able to obtain high titres up to 100 mg/L and 41 g/L of artemisinic acid and amorphadiene, respectively; the latter of which is the highest reported amorphadiene productivity in the literature at a rate of 390 mg/L·h (Westfall et al., 2012).

2.3. The MEP Pathway

The MEP pathway is responsible for isoprenoid production in most bacteria such as *E. coli*, as well as in plant chloroplasts where products GPP and GGPP, among other monoterpenes, C_{16} homoterpenes, diterpenes, and tetraterpenes are produced (Chandran et al., 2011).

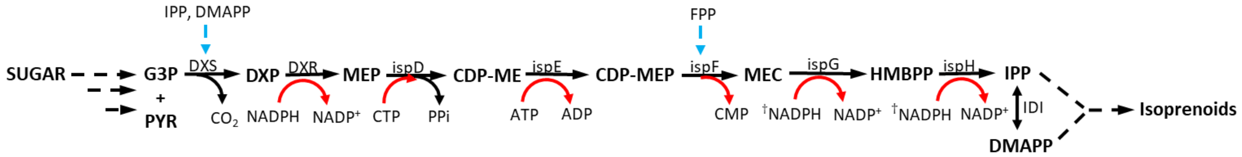

†NADPH cofactors catalyzing IspG and IspH are only required for cell-free synthesis since *in vivo* synthesis has electrons available from the electron transport chain.

Figure 6: The MEP pathway for isoprenoid synthesis.

As shown in Figure 6, pyruvate (PYR) and D-glyceraldehyde 3-phosphate (G3P) produced from the glycolysis pathway undergo an eight-step reaction in the MEP pathway to produce IPP and DMAPP in an approximately 5:1 ratio for *E. coli* (Boronat & Rodríguez-Concepción, 2015). The reaction requires ATP, NADPH, and cytidine triphosphate (CTP) as cofactors. In the first step of the reaction, 1-deoxy-D-xylulose-5-phosphate synthase (DXS) catalyzes the condensation of PYR and G3P to form 1-deoxy-D-xylulose-5-phosphate (DXP). Subsequent isomerization and reduction of DXP catalyzed by 1-deoxy-D-xylulose-5-phosphate reductase (DXR) produces 2-C-methyl-D-erythritol-4-phosphate (MEP). The enzymes MEP cytidylyl-transferase (IspD) and CDP-ME kinase (IspE) then catalyze the formation of 4-diphosphocytidyl-2-C-methyl-D-erythritol (CDP-ME) and 4-diphosphocytidyl-2-C-methyl-D-erythritol-2-phosphate (CDP-MEP), respectively. Cyclization catalyzed by 2-C-methyl-D-erythritol-2,4-cyclodiphosphate synthase (IspF) to produce 2-C-methyl-D-erythritol-2,4-cyclodiphosphate (MEC) followed by ring-opening reduction catalyzed by 1-hydroxy-2-methyl-2-E-butenyl-4-diphosphate synthase (IspG) then produces the final pathway intermediate 1-hydroxy-2-methyl-2-E-butenyl-4-diphosphate (HMBPP). Finally, 1-hydroxy-2-methyl-2-E-butenyl-4-diphosphate reductase (IspH) catalyzes the reduction of HMBPP to produce IPP and IDI catalyzes the isomerization of IPP to DMAPP adjusting the relative amount of IPP and DMAPP required to meet downstream isoprenoid synthesis requirements.

One of the benefits of the MEP pathway is that it is energetically balanced, whereas the MVA pathway produces excess NADH which diverts carbon away from isoprenoid synthesis pathways in favour of endogenous regulation (Yadav et al., 2012). To produce 1 mol of IPP, the MVA pathway requires 1.5 mol of glucose or 3 mol of glycerol, whereas the MEP pathway only requires 1.255 mol of glucose or 2.151 mol of glycerol (Yadav et al., 2012). Although higher carbon efficiencies are a major advantage of the MEP pathway, native isoprenoid flux produced by *E. coli* for metabolic regulation is typically very low (Ajikumar et al., 2010, Morrone et al., 2010). Metabolically engineering the MEP pathway for increased isoprenoid synthesis therefore has to consider several factors such as enzyme inhibition, bottlenecks, and competing endogenous pathways when increasing pathway flux.

Several of the issues discussed relating to the MVA pathway are also present for the MEP pathway. Examples of these include the inhibition of cell growth by IPP accumulation and competition with anabolic pathways due to the overexpression of NADPH dependant enzymes such as DXR. Additionally, IPP and DMAPP provide feedback inhibition to DXS at both the genetic and protein levels which makes overexpression of DXS challenging (King et al., 2017). Several enzymes have been identified as bottlenecks including DXS, IDI, IspD, IspF, and IspG (Ajikumar et al., 2010; Leonard et al., 2010; Zhou et al., 2012). Studies have shown that overexpression of these enzymes can significantly increase isoprenoid yields with DXS and IDI having the largest effects on pathway flux (Yuan et al., 2006; Banerjee et al., 2013).

Wang et al. (1999) focused on downstream optimization and identified IPP isomerization and the conversion of FPP to GPP as two potential pathway bottlenecks with GGPP synthase being the rate-limiting step. Overexpression of IDI and GGPP synthase in *E. coli* increased astaxanthin yields to a value of 1.25 mg/g dry cell weight (DCW) which was 50-fold higher than previously reported (Wang et al., 1999).

Yuan et al. (2006) used promoter engineering and replaced the native *E. coli* promoters with strong bacteriophage T5 promoters. Enzymes DXS and IDI were identified as rate-limiting steps and independent overexpression of each enzyme led to a 2.0- and 1.4-fold increase in the production of β-carotene, respectively (Yuan et al., 2006). Further promoter engineering resulted in a 6 mg/g DCW titre of β-carotene for recombinant *E. coli* having combinatory overexpression of DXS, IDI, ispD, and IspF (Yuan et al., 2006).

Morrone et al. (2010) were also able to obtain increased yields using recombinant *E. coli* by overexpressing IDI, DXS, and DXR which resulted in an abietadiene titre of 7.3 mg/L however yields were much lower than for recombinant *E. coli* utilizing the MVA pathway. Unlike the results of Yuan et al. (2006) who used bacteriophage promoters for enzyme overexpression, Morrone et al. (2010) observed reduced isoprenoid yields when DXS was the sole enzyme overexpressed.

This demonstrates the complexity of the DXS bottleneck and how variations in the method of gene overexpression can affect metabolic control and downstream pathway flux.

Farmer and Liao (2000) identified IDI and phosphoenolpyruvate synthase, which controls flux through the native isoprenoid pathway by regulating the balance of PYR and G3P, as rate-limiting steps. Engineering a dynamic regulatory system in *E. coli* capable of overexpressing genes in response to changing metabolic conditions resulted in high lycopene titres upwards of 150 mg/L and a threefold increase in productivity up to 0.16 g/L·h (Farmer & Liao, 2000). Alper et al. (2005) were also able to obtain increased lycopene yields upwards of 18 mg/g DCW by using combinatorial gene knockout on engineered *E. coli* having strong T5 bacteriophage promoters for the DXS, IDI, IspD, and IspF genes. Sun et al. (2014) utilized a 7.0 L fed-batch bioreactor and engineered *E. coli* overexpressing DXS, IDI, and central metabolic modules (α-ketoglutarate dehydrogenase, succinate dehydrogenase, and transaldolase B) responsible for increased NADPH and ATP supply, which led to increased lycopene titers up to 50.6 mg/g DCW.

Leonard et al. (2010) identified downstream processing relating to the enzymes GGPP synthase and levopimaradiene synthase (LPS), which catalyzes the conversion of GGPP to levopimaradiene, as rate-limiting for *E. coli* having overexpressed DXS, IDI, IspD, and IspF genes. Further strain optimization to include GGPP synthase and LPS overexpression resulted in a 2600-fold increase in levopimaradiene levels compared to wild-type *E. coli* with the engineered strain reaching titres up to 700 mg/L after 169 h in a 3 L bioreactor (Leonard et al., 2010).

Ajikumar et al. (2010) used multivariate pathway engineering to optimize taxadiene synthesis by overexpressing DXS, IDI, IspD, IspF, GGPPS, and taxadiene synthase in *E. coli*. Additionally, indole was identified as an inhibitory metabolite at concentrations above 100 mg/L (Ajikumar et al., 2010). Fermentation in a 1 L bioreactor using the optimized *E. coli* strain resulted in a taxadiene productivity of 8.5 mg/L·h and titres up to 1.02 g/L which was a 15000-fold improvement relative to native *E. coli* (Ajikumar et al., 2010).

2.4. Combinatory Pathways and By-Passes

Due to the limitations of the MVA and MEP pathways such as competing metabolic pathways, host toxicity, pathway inhibition by intermediate metabolites, and the need for extensive strain engineering relating to enzyme overexpression and adaptive metabolic regulation, several attempts to find alternative synthesis methods have been explored. Examples of synthesis alternatives to the traditional metabolic engineering of the MVA and MEP pathways include *in vitro* cell-free biosynthesis, multi-modular combinatory pathway engineering, and identifying potential entry points and by-passes in the MVA and MEP pathways to circumvent rate-limiting bottlenecks.

Korman et al. (2017) used a 27-enzyme, *in vitro*, cell-free system to continuously produce limonene, pinene, and sabinene via the glycolytic Embden-Meyerhof-Parnas (EMP) pathway in combination with the MVA pathway. The system fully recycled all cofactors *in situ* and was not limited by cellular toxicity limits or competing endogenous pathways which resulted in high product titres of 12.5, 14.9, and 15.9 g/L for limonene, pinene, and sabinene, respectively (Korman et al., 2017). Although using cell-free biosynthesis allowed for increased product titres, the productivity was relatively low at only 0.1 g/L·h (Korman et al., 2017) which was at the lower acceptable industrial limit for fine chemicals (Straathof et al., 2002). Since the costs of product purification and enzyme maintenance would be highly expensive for a system having so many enzymes, the productivity levels are too low to justify using cell-free isoprenoid biosynthesis at an industrial level for such a complex system and further improvement is necessary.

Liu et al. (2013) used the traditional EMP pathway, along with the Entner-Doudoroff pathway (EDP), Pentose Phosphate pathway (PPP) and Dahms pathway (DP) in combination with the MEP pathway to investigate the known feeding bottleneck associated with the imbalanced supply of PYR and G3P to the MEP pathway (Farmer & Liao, 2000). The highest isoprene titres of 219 mg/L were obtained for a minimally engineered strain of *E. coli* utilizing the EDP feeding module to simultaneously produce PYR and G3P from the cleavage of pathway intermediate 2-keto-3-deoxy-gluconate-6-P (Liu et al., 2013). The EMP, PPP, and DP feeding modules had significantly lower isoprene titres in the range of 20-71 mg/L (Liu et al., 2013) which suggests that the native EMP pathway primarily responsible for isoprenoid synthesis in *E. coli* is not the most efficient pathway and further work relating to optimization of the glycolytic MEP feeding module is required.

King et al. (2017) circumvented the feedback inhibition of DXS by IPP and DMAPP by utilizing a 2-step DXS by-pass in engineered *E. coli* to produce DXP from D-arabinose and hydroxyacetone (HA). Attempts further simplifying DXP synthesis using the methylglyoxal pathway to produce HA *in vivo* were also investigated, however the highest lycopene titres of 882 mg/L were obtained using 30 mM HA feeding which limits the application of the by-pass since HA inhibits cell growth at concentrations of 50-100 mM (King et al., 2017).

Importing the MVA pathway into *E. coli* has shown to increase product yields by reducing endogenous regulation commonly associated with the native MEP pathway (Morrone et al., 2010). Kang et al. (2016) investigated further reducing endogenous regulation and product toxicity in *E. coli* by developing an IPP by-pass to eliminate the inhibition of MVK and IPP toxicity (Banerjee et al., 2013; George et al., 2018). The by-pass utilized the promiscuous activity of MVD and required five enzymes for the decarboxylation of MVP to isopentenol which resulted in a productivity of 0.022 g/L·h, and increased titers up to 1.08 g/L once optimized (Kang et al., 2017).

2.5. The IUP

The pathways discussed thus far have all relied on entry points within the naturally occurring MVA and MEP pathways. Despite improving pathway productivity by metabolically engineering pathway bottlenecks and reducing endogenous regulation, the MVA and MEP pathways still have several limiting factors such as host toxicity, enzyme inhibition, complex strain engineering requirements, and uneconomical cell-free synthesis. The recently developed IUP is a promising synthetic pathway with the potential to alleviate many of these issues (Chatzivasileiou et al., 2019; Ward et al., 2019)

The IUP is based on isopentenyl phosphate kinase (IPK) which has been known to catalyze the phosphorylation of isopentenyl monophosphate (IP) to IPP (Lange & Croteau, 1999). More recently, IPK has been identified as part of an alternative MVA pathway among several bacteria and eukaryotes which utilize mevalonate phosphate decarboxylase (MPD) in combination with IPK to catalyze MVP decarboxylation and subsequent IPP synthesis (Dellas et al., 2013). Instead of following this alternative MVA pathway, the IUP uses promiscuous enzyme activity to develop a synthetic pathway that is independent of the native MVA and MEP pathways.

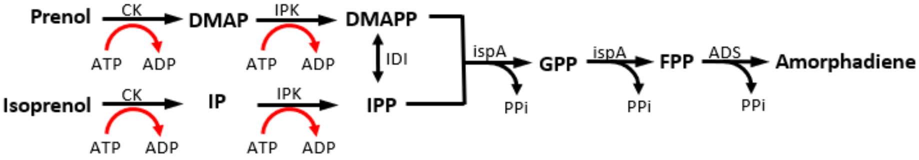

Figure 7: The IUP for isoprenoid synthesis.

As shown in Figure 7, the constitutional isomers of isopentanol, isoprenol and prenol, undergo a two-step reaction to produce IPP and DMAPP respectively in the IUP. The reactions only require ATP as a single cofactor. In the first step of the reaction isoprenol (ISP) and prenol are catalyzed by a promiscuous kinase (usually chlorine kinase [CK]) (Chatzivasileiou et al., 2019; Ward et al., 2019) to produce IP and dimethylallyl monophosphate (DMAP), respectively. IPK then catalyzes the synthesis of IPP from IP and DMAPP from DMAP, respectively. Finally, IDI is included in the reaction pathway to balance the ratio of IPP and DMAPP (or produce IPP/DMAPP if an enantiomerically pure feed is used). Compared to the MVA and MEP pathways which have multiple cofactors and require glycolysis followed by a subsequent seven or eight-step reaction pathway to produce IPP and DMAPP, the IUP only requires three enzymes and one cofactor, making it very simple.

Analogous to importing the non-native MVA pathway into *E. coli* for reduced metabolic regulation of the isoprenoid pathway, the IUP is decoupled from central carbon metabolism due to the promiscuous activity of CK (Chatzivasileiou et al., 2019). This prevents competing endogenous pathways required for cell growth from decreasing flux through the isoprenoid pathway. The simplicity of the IUP also makes cell-free synthesis a more economically viable option for not only eliminating competing endogenous pathways and metabolic control present *in vivo*, but also issues relating to strain engineering and host toxicity limits.

Chatzivasileiou et al. (2019) increased flux through the IUP in *E. coli* using promoter engineering to overexpress pathway enzyme activity and found that downstream flux for the synthesis of lycopene and taxadiene was limiting due to the accumulation of IPP, DMAPP, and

GGPP, respectively. The enzyme CK from *S. cereviseae* was also noted to have a much higher affinity for isoprenol than prenol, having a substrate binding affinity of 4.53 and 1.11 mM, respectively (Chatzivasileiou et al., 2019). The optimal IPP productivity achieved was high having a value of 0.430 µmol/g_{DCW}·min, which makes the IUP not only advantageous due to its simplicity relative to the MVA and MEP pathways, but also for its increased upstream precursor synthesis efficiency (Chatzivasileiou et al., 2019).

Ward et al. (2019) investigated the feasibility of cell-free synthesis utilizing the IUP for the production of taxadiene in a 3.0 L bioreactor. Optimization of the enzyme concentrations resulted in a taxadiene titer of 220 mg/L and an average productivity of 24.4 mg/L·h (Ward et al., 2019) which was significantly higher than the previously highest reported taxadiene productivity of 8.5 mg/L·h for a highly optimized strain of *E. coli* utilizing the MEP pathway (Ajikumar et al., 2010). *In vitro* isoprenoid synthesis using the IUP eliminated the need for extensive metabolic engineering relating to issues such as competing endogenic pathways and host toxicity, however the concentration of ATP proved to be limiting at concentrations above 10 mM for cell-free systems due to solubility limitations (Ward et al., 2019).

2.6. Conclusion

Over the last 20 years, significant improvements to the upstream synthesis of isoprenoids precursors have been made. The MVA and MEP pathways have been extensively engineered to overexpress known enzymatic bottlenecks, reduce endogenous regulation, and develop new by-pass mechanisms. Despite these improvements, MVA and MEP dependant pathways remain fundamentally complex and issues such as low isoprenoid flux, host toxicity, uneconomical cell-free production, and enzyme inhibition remain a challenge. Recently the development of the IUP has shown to decouple *in vivo* isoprenoid synthesis from central carbon metabolism resulting in increased isoprenoid yields. The simplicity of the IUP also enables more cost-effective cell-free synthesis and eliminates competing endogenous pathways and host toxicity which resulted in the highest taxadiene flux reported to date of 24.4 mg/L·h (Ward et al., 2019); a 2.9-fold increase relative to the results of Ajikumar et al. (2010) who used a highly engineered MEP pathway in *E. coli*. Future research relating to isoprenoid precursor synthesis involves using metabolic engineering to further optimize the IUP pathway *in vivo*, investigating the use of enzyme immobilization and ATP regeneration systems for cell-free synthesis, and optimizing downstream bottlenecks such as terpenoid backbone synthesis to accommodate increased isoprenoid precursor flux via the IUP.

3. Project Proposal

The purpose of this project is to investigate the use of additive manufacturing for the development of sequentially immobilized enzyme microfluidic reactors for the synthesis of isoprenoids. A review of enzyme immobilization methods for 3D-printable supports and cascade enzyme immobilization identified affinity binding and entrapment as largely uninvestigated cascade immobilization methods having many potential benefits. Advantageous for sequential enzyme immobilization, entrapment was selected for investigation in this study due to its simple immobilization procedure and intuitive coupling with additive manufacturing for immobilization without the requirement for enzyme or support specific optimization; the latter of which is required for affinity binding.

Alternative to the simple cascade immobilized systems commonly investigated in the literature such as HRP-GOD and β-gal-HRP-GOD, a review of isoprenoid synthesis methods identified the recently discovered, synthetic, IUP as a promising pathway for upstream isoprenoid precursor synthesis. Despite extensive metabolic engineering efforts increasing isoprenoid flux through the MVA and MEP pathways, the simplicity of the IUP having only three enzymatic steps instead of seven or eight respectively, greatly reduces the complexity of the pathway for *in vitro* isoprenoid synthesis. Cell-free synthesis of taxadiene via the IUP has also been shown to have enhanced productivity, 2.9-fold higher, than the highest reported value for *in vivo* taxadiene synthesis by the MVA or MEP pathways (Ward et al., 2019; Ajikumar et al., 2010). In addition to the promising literature results for cell-free isoprenoid synthesis via the IUP, the application of sequential enzyme immobilization has the potential to increase enzyme stability, reusability, and enhance product recovery relative to the enzymes free in solution.

$$ISP + ATP \xleftrightarrow{CK} IP + ADP \qquad \text{Equation 1}$$

$$IP + ATP \xleftrightarrow{IPK} IPP + ADP \qquad \text{Equation 2}$$

$$IPP \xleftrightarrow{IDI} DMAPP \qquad \text{Equation 3}$$

$$IPP + DMAPP \xleftrightarrow{IspA} GPP + PPi \qquad \text{Equation 4}$$

$$IPP + GPP \xleftrightarrow{IspA} FPP + PPi \qquad \text{Equation 5}$$

$$FPP \xleftrightarrow{ADS} AD + PPi \qquad \text{Equation 6}$$

Therefore, the enzymatic pathway summarized by Equations 1-6 for the synthesis of amorphadiene, a precursor to the anti-malaria drug artemisinin, via the IUP was selected for the development of a sequentially immobilized cascade microfluidic reactor in this study. In addition to the IUP enzymes previously discussed, farnesyl diphosphate synthase (IspA) and amorphadiene synthase (ADS) were required for terpene backbone synthesis and the production of amorphadiene, respectively.

Table 3: Productivity table for the synthesis of amorphadiene.

Pathway (*strain/plasmids*)	**Synthesis Conditions**	**Productivity (mg/L·h)**	**Reference**
MVA (*pAM322)*	2.0 L Fed-batch bioreactor	390	Westfall et al. (2012)
MVA (p15A-*spec-aroC-hmgS-atoB-hmgR* [L2-8], p15A-*cam-aroB-mevK-pmk-pmd-idi* [L2-5], p15A-*kan-aroA-ads-IspA)*	250 mL Fed-batch bioreactor	375	Shukal et al. (2019)
MVA (*pAM52, pMBIS, pADS)*	2.0 L Fed-batch bioreactor	211	Tsuruta et al. (2009)
MVA (*pBbA5c-MevT-T1- MBIS[CO]*)	Shake flasks	20.8	Redding-Johanson et al. (2011)
MVA (*pMevT, pMBIS, pADS*)	10.0 L batch bioreactor	13.3	Newman et al. (2006)
MVA (pDR111, pHCMC04G)	Shake flasks	8.7	Pramastya et al. (2021)
MEP (*pETA-TM2-galP-glk and pACM-T7-dxs-T7-idi-ADS-IspA*)	Shake flasks	8.4	Zhang et al. (2015)
MVA (pYLXP'- AaADSx2-tYlHMG1-ERG12)	Shake flasks	3.6	Marsafari & Xu (2020)
MVA (*pMevT, pMBIS, pADS*)	Shake flasks	2.2	Martin et al. (2003)
MVA (*EPY224*)	Shake flasks	1.1	Ro et al. (2006)
IUP (p5T7IspA-ads)	Serum bottles	0.02	Chatzivasileiou et al. (2019)
IUP (Cell-free)	Microplate wells	0.007	Ward et al. (2019)

Table 3 summarizes the current literature studies for amorphadiene synthesis with the highest productivity levels reaching 390 mg/L·h for recombinant *S. cerevisiae* overexpressing the entire MVA pathway cultivated and synthesizing amorphadiene in a 2.0 L fed-batch bioreactor.

The scope of this study will focus on the kinetic characterization of the IUP enzymes free in solution and entrapped within 3D-printed PMMA matrices. Additionally, COMSOL Multiphysics will be utilized for modelling of the enzymes free in solution and sequentially immobilized along the walls of a microfluidic channel to reduce the requirement for labour intensive surface-response methodology experiments. Due to the commercial unavailability of the IUP enzymes, a proof-of concept using the widely characterized, model enzyme, ALP will also be investigated prior to the pathway given by Equations 1-6 to determine the feasibility of using stereolithographic polymerized PMMA supports for enzyme entrapment. Although the selected pathway focuses on the synthesis of amorphadiene, the intended purpose of this study is to model and develop complex sequentially immobilized microfluidic reactors extendable for the synthesis of other isoprenoids or cascade enzyme systems.

The research objectives of this study were as follows:

1. Determine a suitable, robust, immobilization procedure for the entrapment of enzymes within 3D-printed PMMA matrices.
2. Characterize the immobilized enzyme kinetics of the model enzyme ALP to investigate the effects of enzyme concentration and the SAV ratio on the modelled enzyme immobilization efficiency.
3. Design and simulate an ALP microfluidic reactor in COMSOL Multiphysics to compare the steady-state COMSOL model with experimental results and experimentally monitor the enzyme stability during continuous operation and storage.
4. Quantify the immobilized enzyme kinetics of the IUP enzymes for the design, COMSOL Multiphysics simulation, and experimental testing of a sequentially immobilized microfluidic reactor to investigate the productivity and stability of amorphadiene synthesis.

It is hypothesized that the use of entrapment during stereolithographic 3D-printing will limit enzyme degradation during immobilization due to low UV-exposure rates such that enzyme activity is retained, no significant shift in the modelled substrate binding affinity kinetic parameters is observed, and the modelled immobilization efficiency values are enzyme-specific. Additionally, if the enzyme concentration or SAV ratio of the tested immobilized enzyme assay wells or microfluidic reactors are increased, then the enzyme activity and modelled immobilization efficiency are expected to increase proportionally. It is also hypothesized that the enzyme stability of entrapped enzymes will be relatively high based on literature references of similar systems (Schmieg et al., 2019; Xu et al., 2006; Heo & Crooks, 2005) and that the productivity of amorphadiene synthesis will be dependant on accurate quantification and balancing of the IUP enzyme kinetics to reduce the accumulation of intermediate metabolites and promote increased pathway flux.

4. Methods & Materials

Prefacing details of the methods and materials used in this study, a brief overview of the experimental methodology and workflow will be discussed.

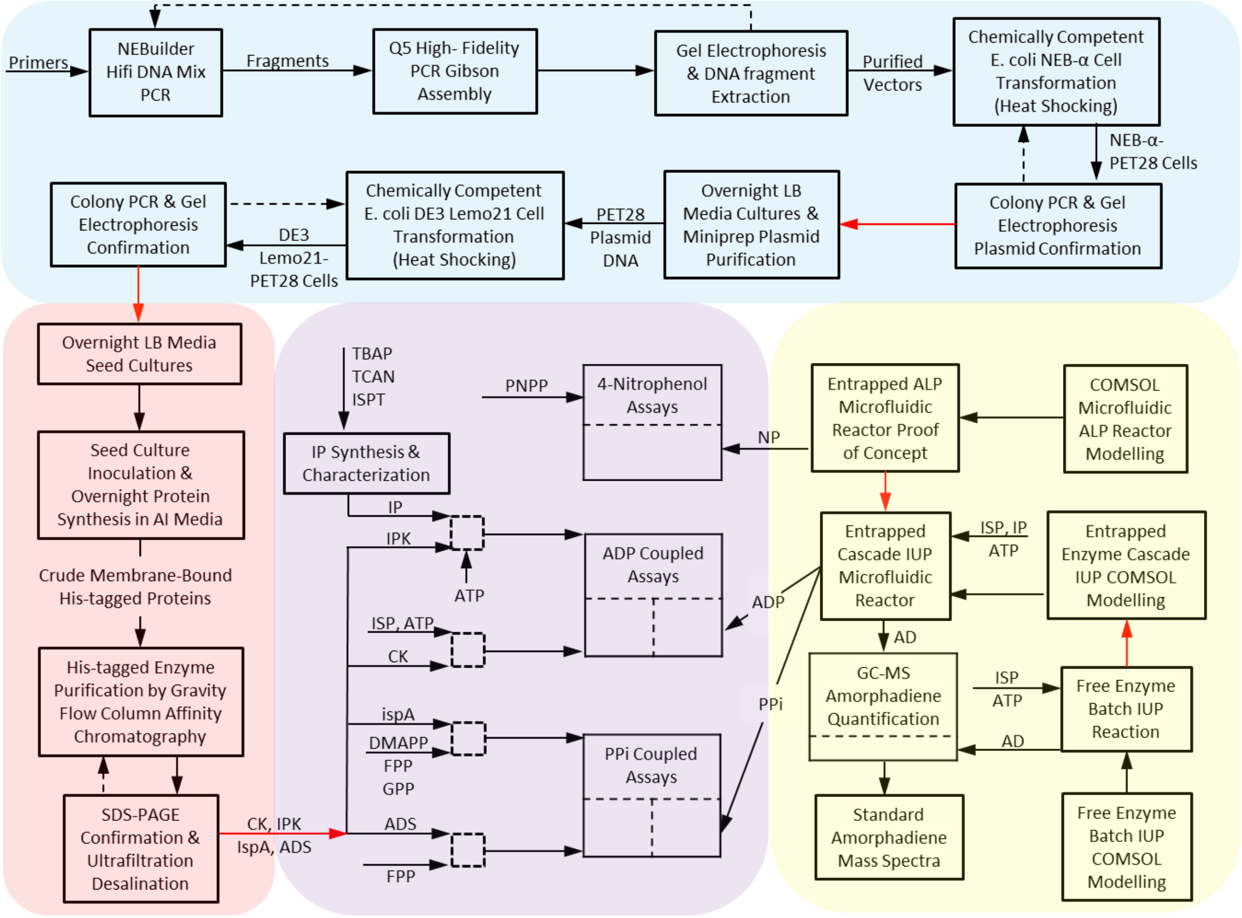

Figure 8: Simplified experimental workflow diagram. Red arrows and dashed arrows represent limiting steps and result-dependant steps, respectively. Colourized subsections are as follows: Cloning and cultivation (blue); Protein synthesis and purification (red); Free/immobilized enzyme assays (purple); and COMSOL Multiphysics modelling and immobilized microfluidic reactor experimentation (yellow).

As shown in Figure 8, the experimental workflow was compartmentalized into four sections: 1. Cloning and cultivation (blue), 2. Protein synthesis and purification (red), 3. Free/immobilized enzyme assays (purple), and 4. COMSOL Multiphysics modelling and immobilized microfluidic reactor experimentation (yellow). The workflow diagram has several key limiting steps shown by red arrows. The first limiting step has been previously mentioned and investigates entrapping ALP in 3D-printed PMMA supports to access the feasibility of the immobilization method by first characterizing the activity of ALP using free and immobilized kinetic assays followed by modelling and continuous operation of an immobilized ALP microfluidic reactor to adjust the immobilization procedure if necessary. This was performed before commencing with cloning and cultivation of the IUP enzymes as a proof-of-concept before increasing the complexity of the immobilized enzyme systems studied. Similarly, for both individual and cascade reactions, the enzymes free in solution were tested and characterized before the immobilized enzymes to address any issues with the coupled enzyme assays or experimental method before proceeding. During the cloning and cultivation section there were two limiting steps after colony PCR to ensure that the transformation of plasmid DNA into NEB-α and DE3-Lemo21 *E. coli* cells respectively were successful. Similarly at the end of protein synthesis and purification, positive identification of each enzyme by sodium dodecyl sulphate–polyacrylamide gel electrophoresis (SDS-PAGE) was a limiting step before proceeding with the free and immobilized enzyme assays of the IUP enzymes.

In the cloning and cultivation section, CK, IPK, IDI, IspA, and ADS primers were amplified using polymerase chain reactions (PCR) and the fragments were purified and individually transformed into chemically competent *E. coli* NEB-α cells. The transformation was confirmed by colony PCR and then the enzyme specific PET28 plasmid DNA samples were purified from overnight cultures and transformed again into *E. coli* DE3-Lemo21 cells. The transformation was again confirmed using colony PCR and liquid glycerol stocks were created before proceeding with protein synthesis and purification.

Using overnight lysogeny broth (LB) cultures inoculated with the previously made glycerol stocks, autoinduction (AI) media was inoculated and incubated overnight resulting in individual cultures of crude, membrane-bound, his-tagged proteins. Following incubation, the cells were lysed and gravity flow column affinity binding with a Ni-resin was used to purify the resulting lysates. The purified enzymes were then characterized using SDS-PAGE and desalted using ultrafiltration to prevent ionic interference with the free and immobilized kinetic assays.

Prior to performing enzyme kinetic characterization, isopentenol (ISPT), tetrabutylammonium dihydrogenphosphate (TBAP), and trichloroacetonitrile (TCAN) were used to synthesize IP which was then purified by ion-exchange gravity flow chromatography for use as a substrate for the characterization of IPK. As shown in Figure 8, in addition to IP, commercially available ISP, IPP, DMAPP, GPP, FPP, and ATP were required for the coupled ADP and PPi kinetic assays which both monitored NADH consumption spectrophotometrically for the characterization of CK/IPK and IspA/ADS, respectively. Kinetic assays were run individually for both the enzymes free in solution and entrapped in 3D-printed PMMA microwells for modelling of the enzyme turnover rates, substrate binding affinity values, and the immobilization efficiencies.

After fully characterizing the kinetics of CK, IPK, IspA, and ADS, COMSOL Multiphysics modelling and immobilized microfluidic reactor experimentation were performed for the IUP cascade reaction to investigate pathway flux and the stability of the upstream/downstream immobilized enzyme compartments. The cascade IUP free in solution was first modelled in COMSOL Multiphysics and tested in a batch reaction to ensure the correct activity of IDI and obtain a standard gas chromatography-mass spectroscopy (GC-MS) chromatogram for amorphadiene due to its commercially unavailability. The batch COMSOL Multiphysics model was then extended for the design of a sequentially immobilized IUP enzymatic microfluidic reactor prior to 3D-printing and continuous operation. The concentration of amorphadiene was measured using GC-MS and the concentrations of ADP and PPi leaving the reactor were monitored using the coupled NADH-dependant assays previously used for kinetic characterization.

4.1. Strains and Cloning

All plasmids were individually constructed using PCR and Gibson assembly to assemble the pET28 vector backbone with CK from *S. cerevisiae*, IPK from *Arabidopsis thaliana*, IDI and IspA from *E. coli*, and ADS from *Artemisia annua*, respectively. The constructed plasmids were designed with a 6x his-tag allowing for simple recombinant protein purification and the potential for affinity binding immobilization. Detailed information including the sequence and melting temperature of the primers used for Gibson assembly and colony PCR are provided in Table 9 in *Appendix I*.

To construct the plasmid backbone and gene inserts, PCR was performed using a Q5 High-Fidelity 2X Master Mix and the assembled fragments were confirmed using gel electrophoresis. For PCR, a master mix containing Q5 High-Fidelity 2X Master Mix, PCR forward primer, and ultrapure water was prepared. To prepare the backbone prior to PCR, DpnI was used to cleave undesired methylation sites by incubating the backbone for 1 h at 37 °C. The final concentrations of the 25 µL PCR reaction mixtures after the addition of the reverse primers to each PCR microtube were 0.5 uM forward and reverse primers, and 1X Q5 High Fidelity Master Mix. The samples were loaded into a Biorad T100 thermocycler and run with the following settings: Initial denaturation at 98 °C for 30 s; 35 annealing cycles consisting of 10 s at 98 °C, 30 s at the respective primer melting temperatures given in Table 9 in *Appendix I*, and 30 s at 72 °C; and finally, extension for 2 min at 72 °C.

Following PCR, the samples were prepared with loading dye and gel-electrophoresis was run on a 1 % agarose gel in TAE (Tris-base, acetic acid, and EDTA) buffer for 1 h at 90 V using a BioRad Mini-Sub Cell GT system electrophoresis chamber and BioRad Powerpac energy supply. The successfully assembled fragments were visible using UV-light and their size was confirmed by comparing their respective DNA bands with the reference DNA kilobase pair ladder. The successfully assembled fragments having the correct DNA kilobase pair length were then selectively cut from the rest of the agarose gel and purified using the GenepHlow Gel/PCR Kit (DFH300) and standard gel extraction protocol by Geneaid. The amount of each fragment purified was maximized by loading the entire 25 µL PCR product into the wells of the gel. The nucleic acid concentration of each purified sample was also determined spectroscopically at a wavelength ratio of 260/280.

Gibson assembly was performed using the NEBuilder HiFi DNA Assembly Master Mix protocol. Briefly, 10 µL of the master mix was added to PCR microtubes on ice along with approximately 100 ng of *E. coli* MG1665 template DNA and a 2-fold excess of the required insert fragments previously assembled by PCR. The reaction mixtures were brought to a 20 µL reaction volume using ultrapure water and incubated for 15 min at 50 °C using a BioRad T100 thermocycler. Following incubation, the samples were stored on ice.

The Gibson assembly products were individually transformed into T1 phage-resistant, NEB 5-alpha chemically competent *E. coli* cells. Heat-shocking was used for the transformation by adding a small amount of DNA to the *E. coli* cell cultures and placing the samples on ice for 30 min. The cell cultures were then heat-shocked in a water bath for 45 s at 42 °C and immediately placed back on ice for 2 min. Super optimal broth media was then added to the cell cultures and the samples were incubated for 90 min at 37 °C with 250 RPM of shaking.

The transformation into NEB 5-alpha was confirmed using colony PCR and the successfully transformed cultures on LB-agar plates with kanamycin were inoculated into LB media and grown overnight in Erlenmeyer flasks at 37 °C with shaking at 250 RPM. Plasmid DNA from the overnight cultures was extracted using a Presto Mini Plasmid Kit and standard protocol. The concentration of plasmid DNA was quantified spectroscopically at a wavelength ratio of 260/280 and the purified plasmids were transformed into DE3 Lemo21 chemically competent *E. coli* using the heat-shock procedure previously described. Colony PCR was performed to confirm the success of the transformation and the resulting DE3 Lemo21 *E. coli* cultures having the PET28 plasmid with individual CK, IPK, IDI, IspA, and ADS genes were stored short term at 4 °C on re-streaked LB-agar plates with kanamycin until subsequently used for glycerol stock preparation or as seed cultures for protein production and purification.

4.2. Colony PCR

To confirm the successful transformation of purified DNA plasmids into NEB 5-alpha and DE3 Lemo21 chemically competent *E. coli* cells, colony PCR and gel electrophoresis were performed. The transformed cells were grown overnight in liquid cultures by inoculating 1 % of the transformed cells into LB media and incubating at 37 °C with a shaker speed of 250 RPM. The cells were then plated onto LB plates containing kanamycin and incubated at 37 °C overnight to grow cell colonies. The selected colonies (typically 5-7) for performing PCR were then re-streaked onto additional LB-kanamycin plates to grow seed cultures for any successfully transformed colonies.

Colony PCR was performed using a routine protocol with Taq DNA Polymerase and Buffer (NEB-M0273L). A small amount of template DNA (<1000 ng) for each colony from the re-streaked plates was suspended in 10 µL of ultrapure water and heated at 95 °C for 10 min to lyse the cells. The template DNA samples and respective reverse PCR primers were then added to a pre-made PCR mastermix in PCR microcentrifuge tubes resulting in a final concentration of 200 µM dNTPs, 1 uM forward primer, 1 µM reverse primer, 1.25 U Taq DNA polymerase, and variable amounts of template DNA in 1X Taq Buffer. The microcentrifuge tubes were mixed by centrifugation at 5000 RPM for 1 min prior to beginning PCR and the samples were then loaded into a BioRad T100 thermocycler and reacted using the following settings: Initial denaturation at 95 °C for 30 s; 30 annealing cycles consisting of 30 s at 95 °C, 45 s at 55 °C, and 60 s at 68 °C; and finally, an extension time of 5 min at 68 °C.

After completing colony PCR, gel electrophoresis was performed to confirm the successfully transformed colonies. The colony PCR products were loaded into a 1 % agarose gel in TAE buffer and run for 1 h at 90 V using a BioRad Mini-Sub Cell GT system electrophoresis chamber and BioRad Powerpac energy supply. The successfully transformed colonies were visible using UV-light and their size was confirmed by comparing their respective DNA bands with the reference DNA kilobase pair ladder.

4.3. Protein Production and Purification

Individual plasmids with the necessary genes for the protein synthesis of CK, IPK, IDI, IspA, and ADS were transformed into DE3-Lemo21 *E. coli* cells and suitable seed cultures grown from individual colonies were selected using colony PCR and gel electrophoresis. The re-streaked seed cultures grown on LB-kanamycin plates were used to inoculate liquid LB seed cultures which were incubated overnight in Erlenmeyer flasks at 37 °C with shaking at 250 RPM.

Table 4: Autoinduction media composition.

Reagent	Concentration
β-Lactose	1 % (w/v)
Glucose	0.05 % (w/v)
Yeast Extract	0.5 % (w/v)
Glycerol	0.5 % (w/v)
KH_2PO_4	50 mM
$MgSO_4$	2 mM
N-Z Amine	1 % (w/v)
Na_2HPO_4	50 mM
Na_2SO_4	5 mM
NH_4Cl	50 mM
ATCC 1000X Trace Metals (Sigma Aldrich)	0.2X

The proteins were synthesized by inoculating AI media with 1 % of the liquid LB seed cultures and incubating for 16-24 h in Erlenmeyer flasks at 28 °C with shaking at 250 RPM. The composition of the AI media used is provided in Table 4. After a sufficient incubation period, the AI media was centrifuged at 3000 RPM and 4 °C for 15 min using an Eppendorf 5810 R centrifuge to form cell pellets which were frozen at -20 °C until purified further.

The purification of his-tagged proteins was performed using affinity chromatography by selectively binding NEB Express Ni-Resin to his-tagged proteins in a gravity flow column. The lysis, wash, and elution buffers required for purification were all prepared in deionized (DI) water and adjusted to a pH of 7.4 using concentrated sulphuric acid or sodium hydroxide. The final concentrations of the three buffers were 10 mM sodium phosphate, 300 mM sodium chloride, as well as 5 mM imidazole for the wash buffer, and 300 mM imidazole for the elution buffer, respectively.

To prepare samples for protein purification, the previously frozen cell pellets containing crude, membrane-bound, proteins were resuspended by vortex in approximately 5 mL/g of lysis buffer and lysed by repeated freeze thaw cycles. A total of 5-8 freeze-thaw cycles consisting of freezing at -20 °C for 30 min followed by thawing at 37 °C for several min were performed with intermittent vortexing as needed. Due to relatively low protein yields for CK using freeze-thaw cell lysis, 0.5 mg/mL of lysozyme was also included in the lysis buffer and an incubation period of 30 min on ice was allowed prior to additional freeze-thaw cycles. Glass beads were also added to the CK lysate to shear excess intracellular DNA released during cell lysis and reduce the viscosity which was greatly increased by the addition of lysozyme. After cell lysis, the samples were centrifuged at 3900 RPM for 15 min at 4 °C to pellet the residual cellular debris. The clarified lysate supernatants were then transferred to new 15 mL centrifuge tubes on ice and an aliquot of the clarified lysates were retained for SDS-PAGE analysis.

To prepare the gravity column for protein binding, the Ni-Resin was resuspended using gentle shaking and 1 mL of the resin slurry was transferred to a 5 mL polypropylene column fitted with a polyethylene separator to support the resin bed. The resin bed was equilibrated by adding 5 mL of lysis buffer and allowing the buffer to flow through. The clarified protein lysate samples were then individually loaded into columns and 5-10 min were allowed for the his-tagged proteins to bind to the resin. After sufficient time for binding, the columns were emptied, and the binding flow-through solutions were collected for SDS-PAGE analysis. The bound his-tagged proteins were then washed with approximately 15 mL of wash buffer and three flow-through samples corresponding to the successive addition of wash buffer to the column were collected for SDS-PAGE analysis. Finally, the his-tagged proteins were eluted in fractions by the successive addition of 1 mL of elution buffer with three aliquots of each eluate set aside for SDS-PAGE analysis.

Since the NEB Express Ni-resin can be reused several times before requiring regeneration, individual columns for each protein required were used to enhance the purity of the eluted proteins. For storage of the columns when not in use, 5 mL of 30 % isopropanol was added to the columns and allowed a contact time of 20 min to remove any residual proteins, lipids, or lipoproteins bound to the resin. The column was then rinsed with 10 mL of DI water and 5 mL of 20 % ethanol was added to the columns for long-term storage at 4 °C.

To prevent the imidazole in the elution buffer from interfering with downstream processing, the enzyme solutions were also purified using ultrafiltration to remove salts and any potential low molecular weight impurities. The elution samples were thawed on ice and loaded into Vivaspin 10K MWCO 20 mL filter centrifuge columns and spun at 3900 RPM for 30 min at 4 °C using a swing bucket, Eppendorf 5810 R centrifuge. The concentrated enzymes in the membrane compartment were then resuspended in 1 mL of deionized water, transferred to microcentrifuge tubes, and stored at -20 °C.

4.4. SDS-PAGE

To confirm successful endogenous protein synthesis, cell lysis, and his-tagged protein purification using gravity flow Ni-binding, SDS-PAGE was performed. Samples of the clarified protein lysate, protein binding effluent, column wash flow-through, and protein eluate were prepared using 4x Laemmli Sample Buffer and β-mercaptoethanol. A stock solution of 4x Laemmli Sample Buffer with 5 % β-mercaptoethanol was used to dilute the samples 4:1 in PCR microtubes. The samples were mixed briefly by centrifugation before being incubated at 95 °C for 5 min in a BioRad T100 thermocycler to denature the proteins.

SDS-PAGE gels were cast using a TGX FastCast acrylamide kit by mixing the resolver and stacker reagents together along with tetramethylethylenediamine and freshly prepared 10 % ammonium persulfate solution according to the kit instruction manual for 1.0 mm BioRad glass plates. The resolving and stacker gels were cast simultaneously by loading the glass plates with resolver gel up to 1 cm below the wells and then gently overlaying the stacker solution ensuring to prevent bubbles and minimize mixing between the resolver and stacker gels solutions. The solutions were left for 1 h to polymerize and were then stored in 0.3 M Tris-HCl (pH 8.8) at 4 °C to keep the gels hydrated until use.

The prepared protein samples were loaded into the wells along with a 10-250 kDa protein ladder and SDS-PAGE was run on a BioRad Mini-PROTEAN Tetra tank at 200 V for 35-45 min. The SDS-PAGE running buffer was prepared from a 10x stock solution for a final concentration of 25 mM Tris, 192 mM glycine, and 0.1 % sodium dodecyl sulphate at pH 8.3. After electrophoresis, the gels were stained overnight using Biotium One-Step Blue Protein Gel Stain with gentle rocking. Optionally, the gels were also de-stained using the same procedure in deionized water to selectively remove the unbound stain from the gel and enhance the colour of the protein bands.

4.5. IP Synthesis

A synthesis procedure for the commercially unavailable intermediate IP was derived from Lira et al. (2013) and Chatzivasileiou et al. (2019) based on the phosphorylation of various alcohols to produce phosphate monoesters with relatively high yields ranging from 43-86 %.

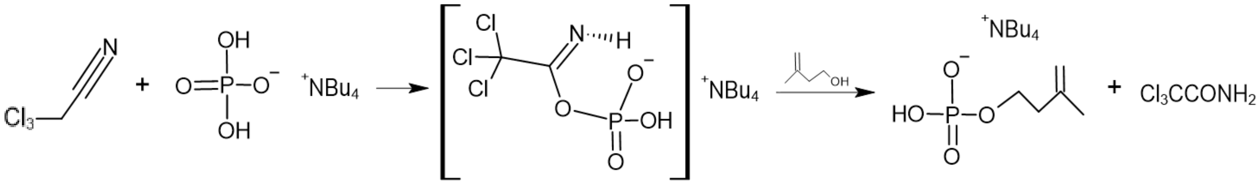

Figure 9: Reaction mechanism for the synthesis of IP using TBAP, TCAN, and ISPT.

The reaction shown in Figure 9 uses TBAP as a phosphate donor and TCAN as an esterification agent to produce IP from ISPT.

In preparation for synthesis, stock solutions of 0.4 M TBAP, 0.4 M TCAN, and 1 M ISPT in acetonitrile were prepared. The stock solutions were used to prepare the reaction mixture in a beaker by adding ISPT to TBAP and TCAN such that the final concentrations were 1 equivalent ISPT, 1.66 equivalents TBAP, and 2.26 equivalents TCAN. The reaction mixture was stirred for 4 h at ambient temperature to allow sufficient time for the reaction to occur. The reaction mixture was then transferred to a boiling flask fit with a condenser and was heated to 88 °C to evaporate the acetonitrile solvent and any unreacted TCAN. The reaction mixture was then resuspended in water equal to the amount of acetonitrile displaced during evaporated and cooled overnight at 4 °C to crystallize the trichloroamide-based by-product which was removed using vacuum filtration.

The IP in the reaction mixture was purified by gravity chromatography using a DOWEX 50WX8 50-100 mesh ion-exchange resin. The resin was loaded into a 5 mL polypropylene column fit with a polyethylene separator to support the resin bed. The DOWEX-50WX8 50-100 mesh resin had a total exchanger capacity of 1.7 meq/mL and was loaded in excess such that the theoretical maximum amount of IP synthesized could fully bind to the resin with a conservative operating efficiency of 50 %. The reaction mixture was loaded into the column and allowed a contact time of 30 min with periodic mixing/backwashing to allow IP to bind with the resin. The column was then percolated using several column volumes of 0.025 M ammonium bicarbonate followed by elution of the bound IP using a 7:2:1 ratio solution of isopropanol, ammonium hydroxide, and water, respectively. The eluate containing IP was then frozen at -80 °C and recovered as a powder by lyophilization using a Labconco FreeZone 2.5 Plus freeze-dryer and Welch 8917 vacuum pump system set at 0.10 mbar and -85 °C.

4.6. Kinetic Modelling and Statistical Analysis

The kinetics of ALP and the IUP enzymes were modelled using well known kinetic models having available literature data for the turnover rate and substrate binding affinity values. Since the IUP enzymes are compartmentalized for sequentially immobilized cascade systems, and the intermediate metabolite concentrations are relatively low, it is reasonable to assume that the individual kinetic models sufficiently describe the system without considering secondary interaction terms associated with the upstream intermediate metabolites.

Table 5: Kinetic models for ALP and IUP enzymes free in solution.

Rate Law Equation	Reference
$v(ALP) = \dfrac{k_{cat,0}[ALP_o][PNPP]}{K_{M,0} + [PNPP]}$	Chappelet-Tordo et al., 1974
$v(CK) = \dfrac{k_{cat,1}[CK_o]\left(\frac{[ISP]}{K_{M,1a}}\right)\left(\frac{[ATP]}{K_{M,1b}}\right)}{\left(1 + \frac{[ISP]}{K_{M,1a}}\right)\left(1 + \frac{[ATP]}{K_{M,1b}}\right) - 1}$	Leibermeister & Klipp, 2006
$v(IPK) = \dfrac{k_{cat,2}[IPK_o]\left(\frac{[IP]}{K_{M,2a}}\right)\left(\frac{[ATP]}{K_{M,2b}}\right)}{\left(1 + \frac{[IP]}{K_{M,2a}}\right)\left(1 + \frac{[ATP]}{K_{M,2b}}\right) - 1}$	Leibermeister & Klipp, 2006
$v(IDI) = \dfrac{k_{cat,3}[IDI_o]\left(\frac{[IPP]}{K_{M,3a}}\right) - k_{cat,3}[IDI_o]\left(\frac{[DMAPP]}{K_{M,3b}}\right)}{\left(1 + \frac{[IP]}{K_{M,3a}}\right)\left(1 + \frac{[ATP]}{K_{M,3b}}\right) - 1}$	Leibermeister & Klipp, 2006
$v(ispA) = \dfrac{k_{cat,4}[ispA_o]\left(\frac{[IPP]}{K_{M,4a}}\right)\left(\frac{[DMAPP]}{K_{M,4b}}\right)}{\left(1 + \frac{[IPP]}{K_{M,4a}}\right)\left(1 + \frac{[DMAPP]}{K_{M,4b}}\right) - 1} + \dfrac{k_{cat,5}[ispA_o]\left(\frac{[IPP]}{K_{M,5a}}\right)\left(\frac{[GPP]}{K_{M,5b}}\right)}{\left(1 + \frac{[IPP]}{K_{M,5a}}\right)\left(1 + \frac{[GPP]}{K_{M,5b}}\right) - 1}$	Leibermeister & Klipp, 2006
$v(ADS) = \dfrac{k_{cat,6}[ADS_o][FPP]}{K_{M,6} + [FPP]}$	Weaver et al., 2015

Where…

$k_{cat,k}$ – Turnover rate of enzyme k (1/s)

$K_{M,ki}$ – Binding affinity of enzyme k for substrate i (μM) (a and b are used generically for reactions having multiple substrates)

As shown in Table 5, ALP and ADS were modelled using Michaelis-Menten kinetics (ALP was selected as a model enzyme specifically for this reason), and CK, IPK, IDI, and IspA were modelled based on applied convenience rate laws which were adapted to reflect the stoichiometry and enzyme regulation by inhibitors for each reaction (Leibermeister & Klipp, 2006). The convenience rate laws also become saturated at high substrate concentrations which allows them to be used for any substrate concentration without limitation.

The kinetic assay parameters for the free enzymes in solution were modelled by first plotting the corrected absorbance readings obtained by UV-vis spectrophotometry for each trial as a function of time and performing linear regression over a linear region of 3-5 min where the rate was highest.

$$SSE = \sum_{m=1}^{n} (v_{exp,k} - v_{pred,k})^2 \qquad \text{Equation 7}$$

Where…
SSE – Sum of squared estimates of error (µM^2/s^2)
$v_{exp,k}$ – Experimental rate of reaction for enzyme k (µM/s)
$v_{pred,k}$ – Predicted rate of reaction for enzyme k (For non-linear regression the rates in Table 5 were used) (µM/s)
n – Number of observations (dimensionless)

Both linear, and non-linear regression were performed by minimizing the sum of least squares function given by Equation 7.

$$R^2 = 1 - \frac{SSE}{SST} \qquad \text{Equation 8}$$

$$SST = \sum_{m=1}^{n} (v_{exp,k} - \bar{v}_{exp,k})^2 \qquad \text{Equation 9}$$

Where…
R^2 – Coefficient of determination (dimensionless)
SST – Total sum of squares (µM^2/s^2)
$\bar{v}_{exp,k}$ – Average experimental rate of reaction (µM/s)

Additionally, the coefficient of determination was calculated using Equations 8 and 9 to estimate the fraction of the variance explained by the change in the respective substrate concentrations for each assay.

$$\frac{1}{\nu_k} = \frac{1}{k_{cat,k} \cdot [E_{o,k}]} + \frac{K_{m,k}}{k_{cat,k} \cdot [E_{o,k}]} \cdot \frac{1}{[S_i]} \qquad \text{Equation 10}$$

Where…
$[E_{o,k}]$ – Initial concentration of enzyme k (μM)
$[S_i]$ – Substrate concentration of component i (μM)

For the ALP and ADS kinetic models following simple Michaelis-Menten kinetics, the 95 % confidence intervals of the fitted parameters were also estimated by first confirming the order of the kinetic models using Lineweaver-Burk linearization given by Equation 10 on the models available in Table 5.

$$k_{cat,k} \pm \frac{\dot{t}_{\alpha/2,n-2}}{E_{0,k}} \cdot \sqrt{\frac{SSE}{n-2}} \qquad \text{Equation 11}$$

$$K_{m,k} \pm \dot{t}_{\alpha/2,n-2} \cdot \sqrt{\frac{SSE}{(n-2) \cdot SST}} \cdot k_{cat,k} \cdot E_{0,k} \qquad \text{Equation 12}$$

Where…
$\dot{t}$ – Critical t-distribution value (dimensionless)
α – significance level (dimensionless)

The confidence intervals of the turnover rates and binding affinities for the simple linearized models were then calculated using Equations 11 and 12, respectively. It should be mentioned that Lineweaver-Burk linearization was not used for regression due to its inaccuracy at low substrate concentrations and its definition in Equation 10 is only presented to support the use of Equations *11* and 12 for the linearizable ALP and ADS kinetic models. Due to the complexity estimating the confidence intervals for non-linear kinetics such as for CK, IPK, and IspA, the mean values of the turnover rate and substrate binding affinity values were fitted without consideration for the confidence intervals. For both linear and non-linear regression, the Microsoft Excel generalized, reduced gradient, non-linear solver with forward-looking derivatives was applied with a tolerance of 0.0001.

$$\frac{d[i]}{dt} = \sum_{m=1}^{k} \left(\upsilon_{i,k} \cdot \nu_k\right)$$ Equation 13

$$t = 0, \qquad [i] = [i_0]$$ Equation 14

Where…
$[i]$ – Concentration of species i (μM)
$[i]_0$ – Initial Concentration of species i (μM)
t – Time (s)
$\upsilon_{i,k}$ – Stoichiometic coefficient of species i for reaction k (dimensionless) (See Equations 1-6)

For modelling of the IUP enzymes free in solution to estimate the concentration profile of each species throughout the reaction, the mass balance of each species was derived and solved simultaneously using Equation 13 and the initial value conditions given by Equation 14. The system of equations were modelled and solved in COMSOL Multiphysics as a fully coupled zero-dimension, time dependant study with an absolute tolerance of 10^{-5}.

For the immobilized enzyme assays, the enzyme kinetics were modelled using a modified form of the kinetics available in Table 5.

$$\left[\nu_{Immobilized,k} = \eta_k \cdot \nu_{Free\ Enzyme,k}\right]\Big|_{[S_i],[E_{o,k}],T}$$ Equation 15

Where…
η_k – Immobilization Efficiency of enzyme k (dimensionless)
T – Temperature (K)

To account for the reduced activity due to internal substrate diffusion limitations associated with enzyme entrapment, an immobilization efficiency defined in Equation 15 was applied to the kinetic models of the enzymes free in solution.

$$\mathrm{SE}(\bar{\nu}_{Immobilized,k}) = \sqrt{\frac{\sum_{m=1}^{n}(\eta_{k,m} - \bar{\eta}_k)^2}{n(n-1)}}$$ Equation 16

Where…
SE – Standard Error of the Mean (dimensionless)

The immobilized enzyme kinetics were modelled similar to the free enzyme kinetics by minimizing the sum of least squares and the standard error of the mean immobilization efficiency was calculated using Equation 16 to estimate the uncertainty of the immobilized enzyme kinetics relative to the true immobilization efficiency. This was selected instead of the standard deviation for estimating the uncertainty of the fitted immobilization efficiency parameters since individual immobilized enzyme assays were prone to relatively high experimental error, however by performing a sufficiently large number of assays, the standard error of the mean immobilization efficiency for the samples is minimized giving a good estimate of the true value for the population. Having an aggregate immobilization efficiency is convenient for quantifying the overall reduction in activity due to entrapment, however the immobilization efficiency on a volumetric basis should be interpretated with care since several factors affect its overall value. The principal factors are the operating conditions which must be kept constant for comparison of the immobilized enzyme kinetics with the free enzyme kinetics. These factors include the substrate concentration range, temperature, pH, and enzyme concentrations (although the enzyme concentration can be corrected using a suitable scaling factor since it is linearly proportional to the rate of reaction based on the kinetic models summarized in Table 5). All else being equal, the reaction rate on a volumetric basis is highly dependant on the available surface area for the immobilized enzyme assays. Since it is not meaningful to compare volumetric reaction rates of the free enzymes with the surface reaction rates of the immobilized enzymes directly, volumetric reaction rates will be compared for a given SA:V ratio. Since internal diffusion limitations are intrinsically considered in the definition of the immobilization efficiency due to the challenges previously mentioned regarding its experimental quantification, the only other variable to control during the characterization of the immobilization efficiencies using immobilized assay wells is external substrate diffusion limitations from the bulk solution to the immobilized surfaces. With the operating conditions being held constant, the external diffusion is dependant on the spatial configuration of the immobilized enzymes relative to the bulk fluid. For this reason, the immobilized assay wells for kinetic characterization and immobilized microfluidic reactors for the continuous monitoring of enzyme activity were designed to be kinetically limiting such that only internal diffusion limitations were accounted for when characterizing the immobilization efficiency using Equation 15.

4.7. Individual Free Enzyme Assays

The individual activity of each constituent enzymatic reaction in the IUP (except for IDI which has no spectrophotometric method of detection) were measured using kinetic assays to determine the substrate binding affinity and turnover rate values governing the rate laws summarized in Table 5 for each enzyme at 37 °C. The kinetics of the enzymes free in solution were determined as a reference to compare with the immobilized enzyme assays and determine the immobilization efficiency. Additionally, since the enzymes were produced and purified from a bacterial host, it was useful to analyze the kinetics of the enzymes free in solution to compare with literature values and ensure proper enzymatic activity. A proof-of-concept characterizing the model enzyme ALP was also performed prior to the IUP enzymes to quantify the immobilization efficiency and enzyme activity of a widely reported, commercially available, enzyme. Finally, a protein assay was performed for each purified enzyme stock to determine the enzyme concentration under the assumption that the his-tagged IUP enzymes and ALP had no protein impurities (this assumption was necessary for use of a generalized protein assay). All the free enzyme activity assays were performed in duplicate and protein assays were performed in triplicate.

The activity of ALP was characterized spectroscopically based on a diethanolamine (DEA) assay which monitored the formation of 4-nitrophenol (NP) from substrate 4-nitrophenyl phosphate (PNPP) at a wavelength of 405 nm. The assay was performed by preparing a fresh solution of 1.0 M DEA buffer (Alfa Aesar: A13389) with 0.5 mM magnesium chloride at a pH of 9.8 and adding 4-nitrophenyl phosphate disodium salt hexahydrate (Alfa Aesar: A12310) to make a 150 mM stock solution used for serial dilutions. The kinetic assay was initiated by the addition of ALP (New England Biolabs: SM0371S) and the absorbance was monitored in 96-well plates at a wavelength of 405 nm using a Biotek Synergy 4 spectrophotometer with Gen5 software set to maintain a temperature of 37 °C. Using a similar procedure, serial dilutions of NP (Alfa Aesar: A14376) were prepared to generate a standard curve for estimation of the molar extinction coefficient of NP at a wavelength of 405 nm.

The activity of CK and IPK were characterized spectroscopically using a coupled enzymatic assay dependant on the formation of adenosine diphosphate (ADP) which is a by-product from the reaction cofactor ATP. The coupled assay was catalyzed by pyruvate kinase (PK) to convert phosphor(enol)pyruvate (PEP) and the generated by-product ADP to produce pyruvate and ATP, followed by catalysis by lactate dehydrogenase (LDH) to catalyze the reaction of PYR and β-NADH to produce lactate and β-nicotinamide adenine dinucleotide (β-NAD) which can be monitored spectroscopically at a wavelength of 340 nm. A stock solution of 1.0 M Tris-HCl buffer with 10 mM magnesium chloride at a pH of 7.5; a PEP solution containing 32 mM Phosphor(enol)pyruvic acid monopotassium salt (Sigma Aldrich: P7127), 83 mM magnesium sulfate, and 135 mM potassium chloride; and a β-NADH solution containing 3.8 mM B-nicotinamide adenine dinucleotide, reduced form disodium salt hydrate (Sigma Aldrich: N8129) were prepared for the assay. The final concentration of the assay components was 91 mM triethanolamine, 1.6 mM PEP, 4.2 mM magnesium sulfate, 6.8 mM potassium chloride, 0.13 mM β-NADH, 4.1-6.8 U/mL PK (one unit converts 1.0 µmol of PEP to PYR per min at pH 7.6 and 37 °C) and 6.1-9.6 U/mL LDH (one unit reduces 1.0 µmol of PYR to lactate per min at pH 7.5 and 37 °C) (Sigma Aldrich: P0294). Variable concentrations of the substrate and cofactors were prepared by serial dilution from stock solutions using ISP (Alfa Aesar: B23398) or synthesized IP respectively with adenosine 5'-triphosphate disodium salt (Biobasic: AB0020) depending on whether the activity of CK or IPK was being assayed. Serial dilutions of B-nicotinamide adenine dinucleotide reduced form disodium salt hydrate (Sigma Aldrich: N8129) were also prepared to generate a standard curve. Additionally, adenosine 5'-diphosphate disodium salt (Alfa Aesar: A14029) standards were prepared by serial dilution to check the assay was working correctly. Prior to running the assays, the activity of the PK-LDH reagent was screened using sodium pyruvate (Biobasic: SB0884) and ATP as substrates to ensure the assay was consuming ATP and that the concentrations used were within the range suitable for spectrophotometric monitoring. The absorbance of β-NAD was monitored at 340 nm similar to the procedure previously described for the Biotek Synergy 4 spectrophotometer with the exception that an initial reading was also taken prior to the addition of either CK or IPK since the assay monitored the consumption of β-NAD.

The activity of IspA and ADS were characterized spectrophotometrically using a coupled assay dependant on the formation of pyrophosphate (PPi). PPi was produced as a by-product during the consumption of DMAPP and GPP with IPP catalyzed by IspA and during the formation of amorphadiene from FPP which was catalyzed by ADS. The coupled assay to monitor PPi was catalyzed by fructose-6-phosphate kinase, aldolase, triosephosphate isomerase, and glycerophosphate dehydrogenase which consume a net one mole of PPi per two moles of β-NAD produced which can be monitored spectrophotometrically at a wavelength 340 nm similar to the coupled ADP assay which also monitored the consumption of β-NAD. The reconstituted pyrophosphate reagent (Sigma Aldrich: P7275) was used as supplied and variable amounts of DMAPP, IPP, GPP, and FPP were prepared by serial dilutions depending on whether the activity of IspA or ADS was being assayed. Similar to the previous assays, a 96-well microplate was used with a Biotek Synergy 4 spectrophotometer and an initial reading was taken before the addition of IspA or ADS as a reference for the concentration of β-NAD before beginning the assay. The same multienzyme buffer consisting of 1.0 M Tris-HCl and 10 mM magnesium chloride at a pH of 7.5 was also used along with a standard curve generated from B-nicotinamide adenine dinucleotide, reduced form disodium salt hydrate (Sigma Aldrich: N8129) standards. Additionally, sodium pyrophosphate decahydrate (Sigma Aldrich: 221368) standards were also prepared and tested to ensure the assay was working correctly.

To determine the total protein concentration of each purified enzyme, the Bio-Rad detergent compatible (DC) protein assay was used. The DC protein assay is based on the Lowry assay and utilizes the reaction of protein amino acids with copper in alkaline copper tartrate, followed by the reduction of Folin reagent which results in several reduced species that have a characteristic blue colour and can be monitored spectrophotometrically at a wavelength of 750 nm. The assay was run using the standard microplate assay protocol for samples containing detergent. A standard curve was also generated using the Bio-Rad Protein Assay Standard II (BSA) by performing serial dilutions and monitoring the absorbance at a wavelength of 750 nm. Since the enzymes used in the IUP were not commercially available, the BSA standard curve was applied to all the IUP enzymes under the assumption that the colour development by different proteins was similar. The validity of this assumption cannot be tested without commercially available protein standards for the IUP enzymes, however the relative error caused by this assumption was negligible. Although the values determined for the enzyme concentration and modelled turnover rates may be affected to an unknown degree relative to reported literature values, the immobilization efficiency is not affected by this assumption since it is relative between the free and immobilized assays for each enzyme.

4.8. 3D-Printing and Enzyme Entrapment

For the immobilization of ALP and the IUP enzymes, the B9Creator 3D-printer was selected for use with a methyl methacrylate-based printing resin (B9Creations: B9R-2-Black). The B9Creator is a high-resolution stereolithographic printer capable of printing with a maximum precision of 30.00 ± 0.03 µm which makes it suitable for the development of microfluidic devices with high SA:V features. Additionally, it was ideal for enzyme entrapment since it polymerizes the methyl methacrylate monomer solution layer-by-layer only exposing the enzymes to UV-vis radiation for 1-3 s per layer which prevents enzyme degradation during printing and polymerization of the monomers to PMMA. The build volume selected was 30x50x200 mm which allows for printing at the highest resolution without having to compromise high resolution for increased build volumes.

The process of using 3D-printing to entrap enzymes is simple since the enzymes free in solution can be added directly to the monomer solution prior to printing. However, several steps are required to develop a file compatible with the B9Creator software outlining the specific geometry to be printed. The general procedure for this process involves the creation of a CAD file, meshing and exporting to a standard tessellation language (STL) file, configuring a suitable layout for printing, and finally slicing the STL file into compartmentalized layer-by-layer instructions recognizable by the 3D-printer. To develop the 3D CAD files, Autodesk Fusion 360 was used along with its built-in meshing features and ability to export to STL files. Autodesk Fusion 360 has support for adjusting the mesh density, inversing the mesh normal, and fixing mesh errors, however it lacks the ability to edit or combine meshed bodies effectively and so the open-source software Blender was often used for post-processing of STL-files when significant mesh editing was required. The B9Creator software has built in features capable of configuring STL files and slicing which were used to format the STL files for printing. Typically, the 3D-printed PMMA is washed with isopropanol to dissolve any residual printing resin, however, to prevent enzyme degradation, the 3D-printed PMMA with entrapped enzymes was washed with deionized water and multienzyme assay buffer.

4.9. Immobilized Enzyme Assays

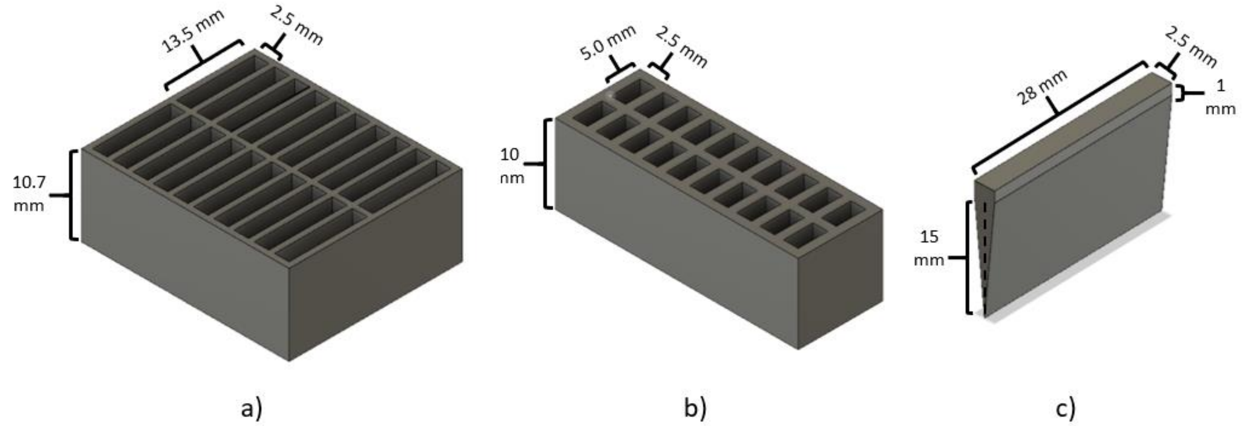

Figure 10: Example CAD files of 3D-printed wells for immobilized enzyme assays. a) 13.5x2.5x10.7 mm square wells having a reaction volume of 360 µL and a SA:V ratio of 1041 m^2/m^3. b) 5x2.5x10 mm square wells having a reaction volume of 120 µL and a SA:V ratio of 1283 m^2/m^3. c) Enlarged 28x3x15 mm triangle well cut-out having a reaction volume of 620 µL and a SA:V ratio of 1340 m^2/m^3 (includes a 1 mm weir to prevent overflow).

Immobilized enzyme assays were conducted using the same spectrophotometry protocols and reagents previously described for the enzymes free in solution. Figure 10 shows examples of assay wells which were 3D-printed with entrapped enzymes by adding the enzymes free in solution to the monomer printing resin. After printing, the wells were washed with either DEA buffer for immobilized ALP or the multienzyme, Tris-HCl buffer previously specified for the IUP enzymes. Since the buffer solutions were less effective at washing the excess resin compared to isopropanol which only required a couple min of rinsing, the wells were typically submerged in buffer and left to rinse overnight at 4 °C before running the assays.

Due to the configuration of the B9Creator printer vat which holds the resin, often a large amount of resin upwards of 100 mL had to be loaded to ensure effective printing. This was problematic for running immobilized enzyme assays since it caused a large dilutionary effect when adding enzymes to the resin. The assay activity was also reduced relative to the free enzymes due to internal diffusion limitations associated with entrapped enzymes and so there was increased potential for low spectroscopic detection and high experimental error if the assay activity was too low. To reduce these effects and promote high assay enzyme activity, the immobilized enzyme wells were designed to have relatively high SA:V ratios and the B9Creator vat was modified with a 3D-printed slab attached to the bottom of the vat to provide void space allowing for smaller resin volumes to be loaded. Additionally since a relatively large amount of enzyme dilution was inevitable to maintain the resin volumes required for stereolithographic 3D-printing, the kinetic assay procedures for the free enzymes were replaced with overnight end-point assays for the immobilized enzyme assays to allow enough time for significant product formation to occur (before considering the effect of internal diffusion on the immobilized enzyme activity, the enzyme activity of the immobilized enzymes were already approximately 20-100 times lower than the free enzyme assays due to enzyme dilution). The immobilized enzyme assays were incubated at a temperature of 37 °C and fit with a 3D-printed lid to limit evaporation from the assay wells. Additionally, the immobilized assays were ensured to be kinetic limiting by providing gentle mixing to ensure a well mixed reaction volume and prevent any external diffusion limitations.

4.10. COMSOL Multiphysics Modelling, Assumptions, and Constraints

COMSOL Multiphysics is a software package used to simulate chemical phenomena, fluid flow, and heat transfer, among other available physics modules. It is useful as a simulation tool to compare predicted simulations with experimental results, and as a method of simulation for experiments that would be impractical or laborious using conventional surface response methodology experimentation. COMSOL Multiphysics simulations are particularly useful when considering the extensive laboratory work and enzyme purification required to optimize a sequentially immobilized enzymatic pathway by surface response methodology experiments. By developing a COMSOL Multiphysics model capable of simulating experimental results, the overall cost of experimentation is greatly reduced since surface response experiments can be simulated and only the optimal design has to be tested experimentally. Although the kinetics and geometry of the COMSOL Multiphysics models used to simulate immobilized ALP and the IUP enzymes vary between models, the underlying constraints, assumptions, and design are similar and will be covered generally in this section.

The COMSOL Multiphysics models were developed using incremental coupling starting with a 2D-geometry and the laminar flow module. The chemistry and transport of diluted species modules were then added and coupled with the reacting flow interface. This approach was selected to address any potential computational limitations before extending the model to use 3D-geometries. Through preliminary modelling, the use of high-resolution 3D-geometries with coupled chemistry, transport of dilute species, laminar flow, and coupled reacting flow modules were found to be computationally intensive and caused memory allocation errors. While increasing the available RAM or changing the solver configuration may have a significant effect towards reducing the overall degrees of freedom to be solved within the model, the geometry was first simplified.

To reduce the computational complexity of the model, extra course meshes were used for imported 3D geometries and where possible, a plane of symmetry was used to reduce the size of the model. For simulations of microfluidic reactors having a winding flow path with no radial variability, using an axial plane of symmetry along the longitudinal length of the reactor reduced the system degrees of freedom by 50 %. The default COMSOL Multiphysics meshing tools were also suitable for meshing the geometry using tetrahedrals, prisms, and triangles at an extra course resolution without having any under-resolved regions. The geometry was imported in DWG binary file format instead of a pre-meshed STL file to avoid the geometry from being re-meshed when imported to COMSOL Multiphysics. By simplifying the microfluidic reactor COMSOL Multiphysics models to have a plane of symmetry and lower mesh resolution, the model solvers were able to be run without having to increase the available RAM or use less favourable iterative/segregated solvers to avoid memory allocation errors.

Having defined the basic module couplings, meshing requirements, and geometry design of the COMSOL Multiphysics models for microfluidic reactor simulations, the general details of each individual module will be covered.

$$\left[\hat{v}_{Immobilized,k} = \frac{\hat{\eta}(a)_k \cdot v_{Free\ Enzyme,k}}{a}\right]\Bigg|_{[S_i],[E_{o,i}],T} \qquad \text{Equation 17}$$

Where…

$\hat{v}$ – Normalized reaction rate (µmol/m^2·s)

$\hat{\eta}$ –Mean normalized immobilization efficiency (dimensionless)

a – Surface to Volume ratio of reaction volume (m^2/m^3)

*Normalized values take into account the effect of surface area.

In the chemistry module, the reactions and species used throughout the model were defined. Based on the expected COMSOL Multiphysics model to be developed utilizing entrapped enzymes along the walls of a microfluidic reactor, each of the products and reactants were defined as bulk species having surface reaction kinetics. Equation 17 was derived by normalizing Equation 15 to account for the effects of surface area and was used along with the kinetics given in Table 5 to model the ALP and IUP enzyme kinetics as surface reactions in COMSOL Multiphysics. Additionally, a solvent species for the buffer solution was defined having the transport properties of water, and a non-reactive surface species was defined as a proxy variable to allow the bulk species to react as if they were surface species. By coupling the reaction of the substrates with the proxy surface species, the enzymatic reactions only take place along the surface of the reactor and not in the bulk fluid which is characteristic of immobilized enzymes. This was done instead of defining a second surface species for each substrate since the kinetics given by Equation 17 depend on the bulk concentration of the substrates and the surface concentrations are only of interest for modelling the internal diffusion which is already accounted for by the immobilization efficiency.

Dependant on the chemistry module, the transport of diluted species module was used for defining regions of reactivity, specifying transport by diffusion and convection, and defining concentration boundary conditions.

$$\left[J_{i,0} = \sum_{m=1}^{k} \upsilon_i \cdot \nu([E_{o,k}], [S_i])_{Immobilized}\right]\Bigg|_T \qquad \text{Equation 18}$$

Where…
$J_{i,0}$ – Boundary molar flux rate of component i (µmol/m^2·s)

The surface reactions simulating the immobilized enzyme reactions were modelled using Equations 17, 18, and the kinetic models given in Table 5 such that the inward boundary flux of the bulk species along the walls of the reactor were set to the reaction rate of the immobilized surface kinetics accounting for the effects of internal diffusion due to enzyme entrapment. Additionally, an insignificantly small concentration constraint was applied to the entire reaction volume using the internal COMSOL Multiphysics constant (eps) such that the minimum acceptable concentration of all species within the model was 10^{-15} µM. This constraint had no effect on the predicted model output since the modelled concentrations were orders of magnitude larger, however it served two practical purposes. The first is that it prevented the kinetic models for CK, IPK, IDI, and IspA given in Table 5 from dividing by zero when the substrate concentrations modelled would otherwise be zero. Additionally, it prevented the solvers using automatic scaling from applying negative concentration values between iterations which could occur if the applied step size was too large for species at low concentrations.

$$\bar{u}[S_{0,i}] = \bar{u}[S_i] - D_{ij} \cdot \frac{d[S_i]}{dy} \qquad y = 0 \qquad \text{Equation 19}$$

$$\frac{d[S_i]}{dy} = 0 \qquad y = L \qquad \text{Equation 20}$$

Where…
$\bar{u}$ – Mean longitudinal velocity (m/s)
D_{ij} – Diffusivity coefficient of component i in solvent j (m^2/s)
y – Longitudinal distance (m)
L – Length of the microfluidic reactor (m)

For the inlet and outlet concentration boundary conditions, the Danckwert flux conditions given by Equations 19 and 20 were applied (Danckwerts, 1953). For tubular reactors having a constant mean longitudinal velocity such as the microfluidic reactors modelled, and operating under laminar flow such that longitudinal diffusion cannot be neglected, the inlet Danckwert boundary condition given by Equation 19 states that the inlet flux at y = 0^- and concentration [$S_{0,i}$] is equal to the flux at y = 0^+ and concentration [Si] by combined convection and diffusion (Danckwerts, 1953). Consequently, for the outlet boundary flux condition given by Equation 20 at y = L^+ to not increase or decrease relative to the concentration of [S_i] at y = L^-, the diffusion term must be set to zero at y = L. The mean longitudinal velocity in Equation 19 was coupled to the laminar flow module, however the diffusivity coefficient of each component required estimation.

$$D_{ij} = \frac{1.173 \times 10^{-16} \cdot (\varphi M_B)^{0.5} \cdot T}{\mu \cdot \hat{v}_A{}^{0.6}} \qquad \text{Equation 21}$$

Where…
M_B – Molecular weight of solvent (kg/kmol)
μ – Viscosity of solution (kg/m·s)
v_A – Solute molal volume at normal boiling point (m^3/kmol)
φ – Association factor for solvent (2.26 for water) (Dimensionless)

Since estimating the diffusivity coefficient of specific species in solution is often done empirically and most of the metabolites used in this study are uncommon in the literature, a generic, empirically derived, correlation for dilute solutions given by Equation 21 was used to estimate the diffusivity of each species (Wilke & Chang, 1955). For the species that were not readily available in the literature, the solute molal volume at normal boiling point was estimated based on the solute molal volume at ambient temperatures. Although this assumption has the tendency to overestimate the diffusion coefficients of each species, it is an assumption made from necessity and one that will be accounted for by applying a conservative margin of error when determining whether external diffusion is a limiting factor within the model.

The final module of the COMSOL Multiphysics model to define is the laminar flow module which is required for coupling with the transport of diluted species to model reacting flow throughout the microfluidic reactor.

$$\rho \nabla \cdot u = 0 \qquad \text{Equation 22}$$

$$\rho \frac{\partial \mathrm{u}}{\partial \mathrm{t}} + \rho (u \cdot \nabla) u = \nabla \cdot [-PI + \mu(\nabla u + (\nabla u)^T)] + F \qquad \text{Equation 23}$$

Where…
ρ – Fluid density (kg/m^3)
u – Velocity vector (m/s)
I – Identity matrix (dimensionless)
P –Pressure (Pa)
F – Volume force vector (N/m^3)

Since the enzymatic microfluidic reactors modelled were operating at ambient pressures and relatively low temperatures (37 °C), the single-phase Navier-Stokes continuity and momentum equations for incompressible flow given by Equations 22 and 23 respectively were selected to model flow through the reactor.

$$N \cdot u = 0 \qquad \text{Equation 24}$$

$$[-PI + \mu(\nabla u + (\nabla u)^T)]N = 0 \qquad \text{Equation 25}$$

Where…
N – Outward pointing normal vector of the boundary (dimensionless)

To define the fluid flow boundary conditions, the reactor walls were first defined using the no-slip boundary conditions given by Equations 24 and 25. The no-slip boundary condition was selected to set the radial boundaries of the microfluidic channel since slip-flow typically only becomes significant at characteristic lengths below 300 nm (Rapp & Bastian, 2017) which is much smaller than the diameter of the proposed microfluidic reactor designs. With the fluid flow contained within the walls of the microchannel by the no-slip boundary condition, the inlet and outlet boundary conditions were defined. Since experimentally the inlet flow rate was a controllable variable and the reactor outlet exits at atmospheric pressure, these operating conditions were implemented as suitable boundary conditions.

$$\left[-PI + \mu\left(\nabla u + (\nabla u)^T - \frac{2}{3}\mu(\nabla \cdot u)I\right)\right]n = -\widehat{P_0}n \qquad \text{Equation 26}$$

$$[-PI + \mu(\nabla u + (\nabla u)^T)]n = -\widehat{P_0}n \qquad \text{Equation 27}$$

$$u \cdot n \geq 0 \qquad \text{Equation 28}$$

$$\widehat{P_0} \leq P_0 \qquad \text{Equation 29}$$

Where…
$\widehat{P_0}$ – Inlet pressure (Pa) (adjusted tangential-stress condition)
P_0 – Inlet Pressure (Pa) (no tangential-stress condition)

For the reactor outlet, the pressure boundary condition was modelled using the incompressible, single-phase flow, boundary conditions given by Equations 26, 27, and the constraints given by Equations 28 and 29. Equations 26 and 27 were selected to be constrained using a normal boundary vector adjusted to satisfy the inequality given by Equation 28 instead of using a tangential velocity condition since it suppressed backflow. Using the tangential velocity condition can result in non-unidirectional flow along the boundary which causes inflow back into the reactor. By adjusting the normal boundary vector, all the points that satisfy Equation 28 have a pressure P_0 similar to if the no tangential-stress condition were used, however the points where Equation 28 is not satisfied become adjusted to have a lower pressure denoted as $\widehat{\mathrm{P}_0}$ in Equation 29, such that backflow is suppressed. Since an outlet boundary condition was specified, the laminar flow module was fully resolved by defining an inlet flow rate as the final boundary condition. This both defines the fluid velocity vector at all points based on the geometry of the microchannel, as well as the inlet pressure based on Equations 26 and 27.

With the chemistry, transport of dilute species, and laminar flow modules all defined and coupled to each other, the microfluidic reactors were simulated by configuring the study node containing options for running parametric studies, defining solving conditions for the dependant variables, and setting the solver configuration and tolerances. To model the microfluidic reactors at steady-state, the stationary solver set to a tolerance of 0.001 was selected. A direct, fully coupled stationary solver which solves a single large system of equations to determine all the unknowns and coupled multi-physic effects at once within a single iteration was selected. This was chosen in alternative to the segregated solver which subdivides the solution into individual modules or even partial modules and solves each step sequentially. Although the segregated solver requires less memory compared to the fully coupled solver, it is often less robust and requires more iterations which increases the probability of the solver diverging from the solution. The specific solver selected for the fully coupled solution was the direct MUMPS solver which used LU factorization on a sparse linear matrix that fully described the coupled system. To represent the model as a system of linear equations, discretization was necessary to transform continuous, non-linear functions into discrete linear equations. COMSOL Multiphysics has built in features capable of performing discretization to form a discrete linear matrix based on an initial discretization specification by the user. For the transport of diluted species and chemistry modules, quadratic discretization was selected since the concentration profiles of each species are the most sensitive dependant variables within the model. For the laminar flow module, the discretization responsible for the pressure and velocity profiles were selected to be linear. The method selected for the iterative solver was the automatic highly non-linear option which uses the damped Newton method to converge at a solution. This iterative solver was selected instead of the constant Newton method which keeps the damping factor constant since increasing the damping factor slowly allows for more robust convergence. With that said, the automatic highly non-linear Newton iterative solver remains highly dependant on the initial guess values selected. Since the initial guess values for the species concentration profiles throughout the reactor were largely unknown beyond using an intuitive guess, and solver convergence was not ensured, two methods promoting a more dynamic, robust, iterative solver were implemented. The first method implemented was to adjust the immobilized enzyme kinetics given by Equation 17 with a ramping function that gradually increased the non-linearity of the model.

$$v\big([E_{o,k}],[S_i],\delta\big)_{Immobilized} = \begin{matrix}(1-\delta)\cdot k_{cat,k}\cdot E_{o,k} + \\ \delta\cdot v\big([E_{o,k}],[S_i]\big)_{Immobilized}\end{matrix} \qquad \text{Equation 30}$$

Where…

δ – Ramping variable (dimensionless)

This was implemented using Equation 30 and an auxiliary sweep that increased the ramping variable (δ) over the range [0,1]. By ramping the solution, when $\delta = 0$, the immobilized enzyme kinetics became linear, equal to the maximum velocity, and decoupled from the local substrate concentration profiles which ensured initial solver convergence. As the ramping variable was gradually increased, the non-linear term of the kinetics in Equation 30 was increased accounting for the varying substrate concentrations throughout the reactor until a value of $\delta = 1$ was reached and Equation 17 was recovered. Although the final solution using Equation 17 or 30 were the same after ramping the solution to $\delta = 1$, by decoupling the immobilized enzyme kinetics from the spatially-dependent substrate concentration profiles for the first iterative solution, the solver becomes more robust by assuming a reasonable linear initial rate of reaction instead of relying on arbitrary initial concentration guesses. With the iterative solver set up to converge robustly, the second method implemented to improve the solver aimed at increasing the computation efficiency required for high tolerance solutions. This was done by configuring a second study node having all the same solver characteristics as the first study node, but with an increased relative tolerance and no auxiliary sweep decoupling the enzyme kinetics from the substrate concentrations for the first iterative solution. Instead of using a ramping function to gradually increase the non-linearity of the model and ensure initial convergence, the second study node was coupled to the solution of the first study node to ensure that the initial guess variables selected were reasonably close to the true model solution calculated at higher relative tolerances. By setting the first study node to a relative tolerance of 0.05, and the second study node to a relative tolerance of 0.001, the first study node, having a robust solver, did most of the computational work at a reasonable tolerance to ensure convergence, while the second study node served as a refinement step to increase the relative tolerance without having to use the computationally extensive auxiliary sweep at high tolerances.

4.11. Preparation and quantification of amorphadiene samples by GC-MS

Although the concentration of amorphadiene can be measured indirectly using coupled enzyme assays, this method was only applicable when considering the formation of amorphadiene from FPP which produced PPi as a by-product. When amorphadiene was synthesized via the IUP pathway using ISP as a substrate, both IspA and ADS formed PPi as reaction by-products and so the coupled assay could no longer be used as a measurement for the concentration of amorphadiene. For this reason, the concentration of amorphadiene was quantified using GC-MS with β-caryophyllene (TRC: C-184725) as an internal standard due to the unavailability of commercial amorphadiene standards.

Due to the low concentrations of amorphadiene synthesized in this study and the necessary use of β-caryophyllene as an internal standard, the amorphadiene samples which were synthesized in buffer solution had to first be prepared for GC-MS. To do this, C-18 (octadecyl) resin (Supelco: 67202) was used to capture the amorphadiene and remove it from the bulk solution containing mainly polar components which were unreactive towards the resin. For batch systems, the resin was added directly to the reaction mixture to capture amorphadiene as it was synthesized. However, for continuous operation, this method would be impractical due to the requirement for a constant supply of the resin. Instead, for continuous operation, the resin was loaded into a gravity flow column supported by a polyethylene spacer and the buffer solution containing amorphadiene was continuously passed through allowing for the C-18 resin to capture amorphadiene. For both batch and continuous operation, the C-18 resin was collected and dried in gravity flow columns by centrifuging the samples at a speed of 13000 RPM until all the residual buffer had flowed through. Once dried, the C-18 resin was washed with DI water and centrifuged again until dry. The amorphadiene captured by the C-18 resin was then eluted with a prepared internal standard solution containing 90 mg/L of β-caryophyllene in ethyl acetate.

Samples analyzed by GC-MS were run on a low polarity, fused silica HP-5 capillary column (30 m, 320 μm, 0.25 μm) (Agilent Technologies: 19091J-413) using a Varian 3800 GC coupled with a Varian 2000 MS. A Varian 8400 autosampler was also used for automation of sample testing and consistent sample injection. All the modules including the GC-MS and autosampler were programmed and controlled using the auxiliary Varian MS Workstation software. Before each method for the analysis of one or more samples was initiated through the MS Workstation software, a series of calibrations and tests were performed to ensure reliable and consistent operation of the GC-MS.

Before calibrating the GC-MS, the system was purged of residual water, air, and other impurities by running several ethyl acetate wash samples through the column followed by an extended bakeout period of several hours. The bakeout temperatures were set to be as high as possible based on the maximum operating conditions specified for the column and detectors. The bakeout procedure was performed under the following conditions: inlet temperature of 280 °C, constant helium carrier gas inlet pressure of 115.8 kPa, column oven temperature of 280 °C, MS transfer line temperature of 280 °C, and a MS trap temperature of 120 °C. After baking out the system, the levels of water and air in the trap were tested to ensure they were minimal and would not interfere with the subsequent mass calibration steps.

The first calibration performed was to ensure the RF tuning was suitable for the entire range of ions detectable. After this step, the axial modulation voltage was adjusted between 2.0-4.0 V and the electron multiplier gain was monitored. For the range of axial modulation voltages tested, a value of 3.0 V was selected to be the optimal condition. At this voltage, the peak threshold was satisfied and the low and high voltage ranges where a 10^5 gain was achieved were found. Despite the electron multiplier voltage being stable at 2150 V (well below the fuse replacement threshold of 3000 V), the final gain setting responsible for optimal sensitivity and resolution was inadequate regardless of the axial modulation voltage tested, and consequently the chromatogram peaks were relatively broader than would be otherwise. After RF tuning and axial modulation voltage calibration, the mass spectrum was calibrated using perfluorotributylamine gas which has characteristic fragmentation peaks at masses of 69, 131, 264, 414, 502, and 614 which were used to generate a standard curve within the MS Workstation software. Finally, the trap function calibration was performed following mass spectrum calibration to ensure consistent ion preparation and fragmentation. Due to the gradual accumulation of water and air within the trap during normal use of the GC-MS, the water and air levels in the trap were monitored after each use and the system was baked out and recalibrated, as necessary. Additionally, the system was recalibrated when changing the temperature of the MS transfer line or trap.

For amorphadiene and β-caryophyllene samples diluted with ethyl acetate, chromatography was performed under the following conditions: 1 µL splitless injection, inlet temperature of 280 °C, constant inlet helium carrier gas pressure of 115.8 kPa, trap temperature of 80 °C, and a MS transfer line temperature of 250 °C. The column oven temperatures were programmed to start at 100 °C for 1 min, increase by 15 °C/min until 200 °C, hold at 200 °C for 2 min, increase by 30 °C/min until 250 °C, hold at 250 °C for 2 min, increase by 30 °C/min until 280 °C, and finally hold at 280 °C for 2 min. The MS was operated using electron ionization (EI) with ions scanned between 40-210 m/z at a rate of 0.5 s per scan. Since the β-caryophyllene standards were at a high concentration of 90 mg/mL, the chromatogram peaks were easily visible while scanning for all ions from 40-210 m/z. However, the amorphadiene samples synthesized from both FPP using ADS or isoprenol using the cascade IUP enzymes were near the detection limit of the GC-MS and so the signals had to be post-processed for better peak identification and resolution. For amorphadiene synthesized from FPP using ADS, the chromatogram noise was filtered out by selectively screening for the fragmentation pattern of amorphadiene within ± 2 m/z to better identify the chromatogram peak and increase resolution by excluding ions contributing to signal noise. For amorphadiene synthesized from FPP, the screened ions within a range of ± 2 m/z were selected based on literature references which had the following mass spectrum peaks: 41, 55, 67, 79, 93, 105, 119, 113, 147, 162, 175, 189, and 204 (Ward et al., 2019; Baadhe et al., 2013). This screening procedure was utilized to generate the mass spectrum of amorphadiene for comparison with literature references to confirm the correct activity of ADS and identify the expected retention time for amorphadiene. For quantification of the amorphadiene concentration relative to the β-caryophyllene internal standard, the parent ion at 204 m/z and the primary amorphadiene fragmentation ion at 189 m/z corresponding to the loss of a methyl group were selectively scanned for based on conventional procedures given in the literature for amorphadiene quantification (Martin et al., 2003; Newman et al., 2006; Rodriguez et al., 2014; Weaver et al., 2015). The concentration of amorphadiene was then determined by integrating the chromatogram peak of amorphadiene and normalizing it to the integrated peak of the β-caryophyllene internal standard.

5. Discussion and Results

5.1. Enzyme Characterization

After protein synthesis and purification, SDS-PAGE was run for the purified enzyme samples and intermediate lysate, resin binding effluent, and wash samples collected during the protein purification process. Figure 11 shows the results of SDS-PAGE after gel staining for IPK, IDI, IspA, ADS, and CK, respectively. Based on preliminary SDS-PAGE results, the protein purification protocol previously described for large batch processing was modified as needed for low yield proteins to increase the concentration of the enzyme elution samples. For SDS-PAGE of the IDI and IspA samples this was not necessary since the enzymes were readily observed in both the clarified lysate samples and the enzyme elution fractions as shown in Figure 11b and Figure 11c, respectively. Based on the results of Figure 11, the molecular weight of IDI and IspA were determined to be approximately 22 and 32 kDa respectively which match the literature values reported for *E. coli* sourced IDI of 20.5-24.5 kDa (Berthelot et al., 2012; Hahn et al., 1999) and *E. coli* sourced *IspA* of 32.1-36 kDa (Fujisaki et al., 1990). Due to the lower relative protein yields of IPK and ADS, the protein purification procedure was modified by an increased number of freeze-thaw cycles, using glass beads to facilitate mechanical shearing of residual DNA and lower the viscosity between lysis cycles, increasing the lysate loading volumes, and reducing the elution volume. These modifications to the protein purification procedure had the effect of increased protein yields after cell lysis, increased protein binding to the Ni-Resin, and increased enzyme concentrations of the elution samples by use of smaller elution volumes. Although these enhanced the detection of IPK and ADS as shown in Figure 11a and Figure 11d, the increased lysate viscosity from improved cell lysis, as well as increased lysate loading on the Ni-Resin, caused the enzyme elution samples to have residual DNA impurities from cell lysis. Although the purified enzyme samples in Figure 11a and Figure 11d would result in a shift in the turnover rate of IPK and ADS if used for kinetic studies, the modified protein purification procedure described above which caused increased impurities in the elution fractions of IPK and ADS were only used for enzyme quantification by SDS-PAGE to ensure the correct enzymes were produced. The elution bands in Figure 11a and Figure 11d for IPK and ADS respectively were pronounced relative to the impurity bands and the molecular weight of IPK and ADS were determined to be approximately 38 and 62 kDa, respectively. These values match the literature values reported of 35.7 kDa for IPK sourced from *A. thaliana* (Uniprot, 2021) and 62-63.9 kDa for ADS sourced from *A. annua* (Chang et al., 2000; Kim et al., 2006; Mercke et al., 2000). Although improving the lysis procedure and concentrating the enzyme elution worked for IspA and ADS, CK had much lower enzyme yields and was undetectable by SDS-PAGE using this procedure. To enhance the protein purification of CK, 0.2 mg/mL of lysozyme, 1 % triton, and glass beads were added to the lysis buffer to improve cell lysis. Additionally, a large batch of CK was purified and concentrated by ultrafiltration before SDS-PAGE was performed.

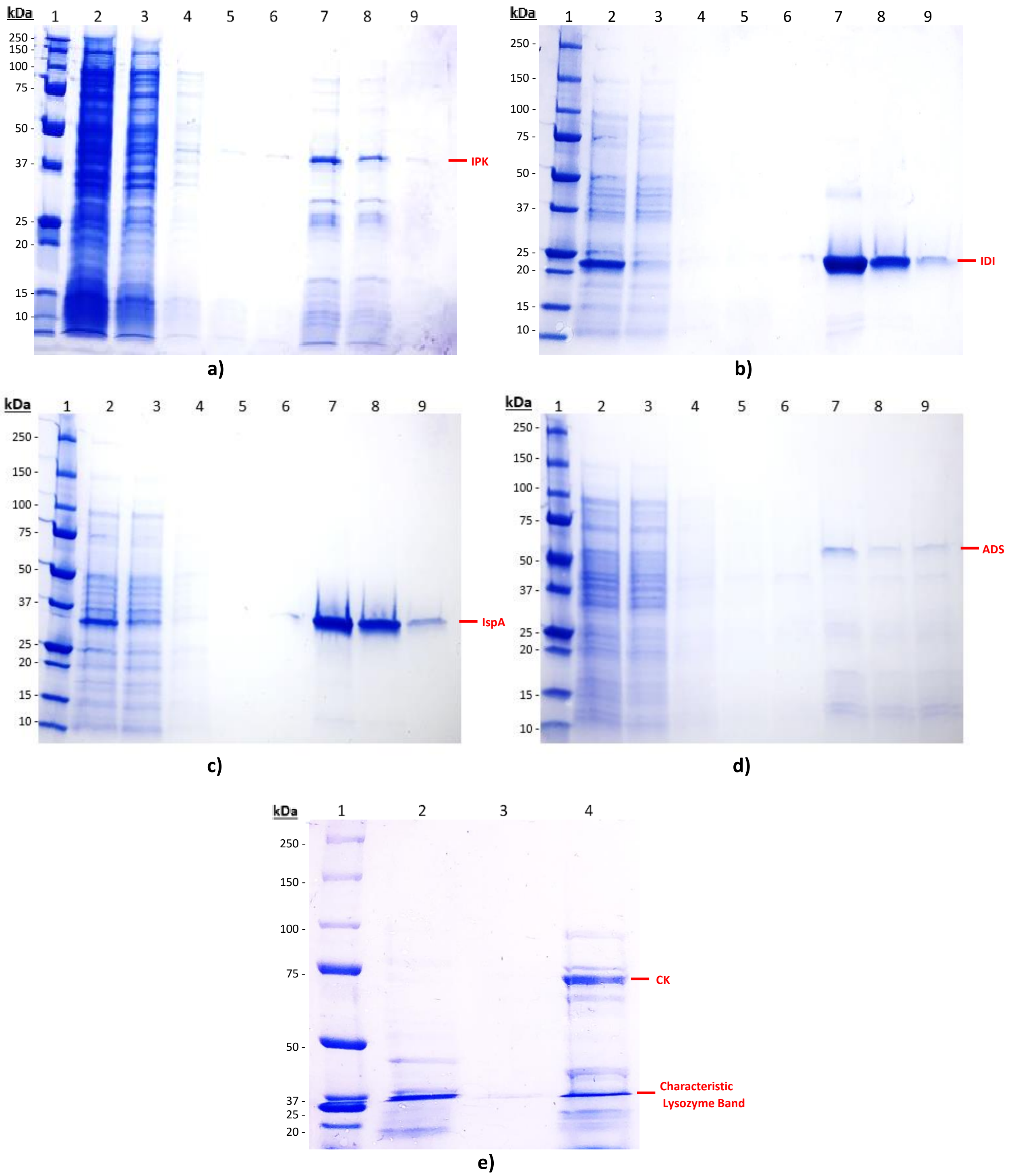

*Figure 11: SDS-PAGE gels of enzyme samples during protein purification for a) IPK, b) IDI, c) IspA, d) ADS, e) CK. The well numbers for gels a-d) correspond to the following: **1** – DNA ladder, **2** - Clarified protein lysate, **3** – Resin binding effluent, **4** – Wash fraction 1, **5** – Wash fraction 2, **6** – Wash fraction 3, **7** – Enzyme elution 1, **8** – Enzyme elution 2, **9** – Enzyme elution 3. For gel e) the well numbers correspond to the following: **1** – DNA ladder, **2** – Clarified lysozyme lysate, **3** – Enzyme elution, **4** – Highly concentrated enzyme elution.*

The resulting gel shown in Figure 11e, had an elution band at approximately 70 kDa which matches the values reported of 67-73 kDa for CK sourced from *S. cereviseae* in the literature (Brostrom & Browning, 1973; Kim et al., 1998). Due to the use of lysozyme, the lysate viscosity was greatly increased causing protein purification to be less specific. The gel shown in Figure 11e had several faint impurity bands and a relatively strong band in the range of 50-75 kDa which was compared with the lysis of native DE3 Lemo21 *E. coli* cells and determined to be characteristic of *E. coli* cell lysis by lysozyme rather than undesirable or incorrect protein synthesis. Unlike the other enzymes purified, lysozyme was used for batch protein cultivation of CK due to its low yields, however, to reduce the impurities shown in Figure 11e, the clarified protein lysate was diluted before loading with the Ni-Resin during purification to mitigate the negative effects of enhanced viscosity on the efficiency and selectivity of purification.

5.2. IP characterization

A sample of previously synthesized IP was resuspended in deuterium oxide and run on a Bruker Ascend 300 MHz nuclear magnetic resonance (NMR) spectrometer to obtain ^{1}H and ^{31}P spectra.

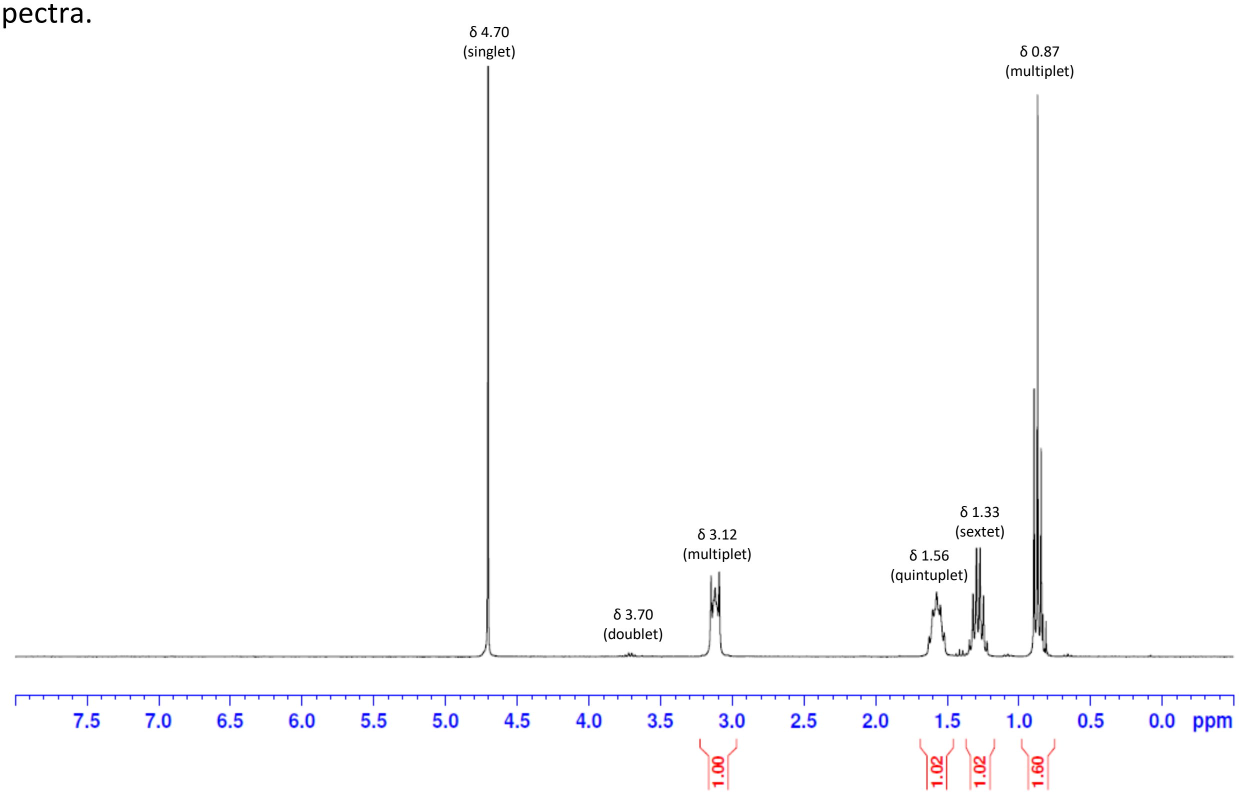

Figure 12: ^{1}H NMR spectra for synthesized IP.

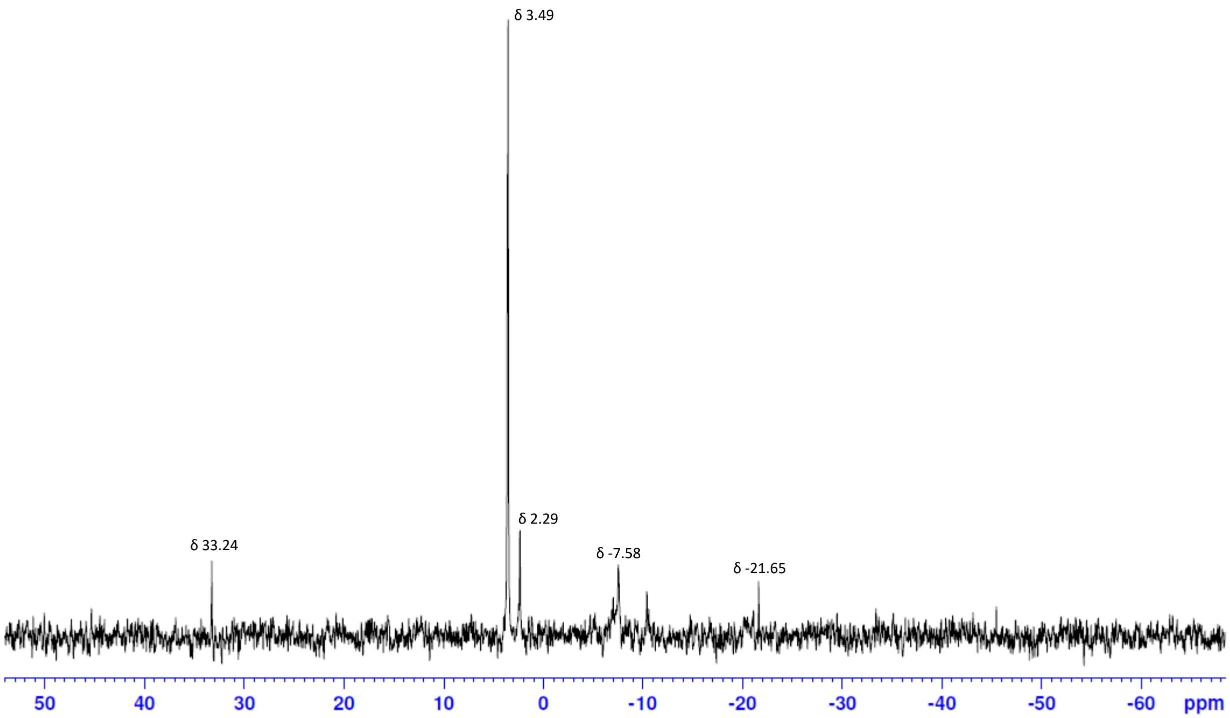

Figure 13: ^{31}P NMR spectra for synthesized IP.

The proton and phosphorous NMR spectra are available in Figures 12 and 13 and chemical shifts (δ) are quantified in parts per million relative to the internal standards tetramethylsiline and trimethyl phosphate, respectively. The following significant ^{1}H NMR signals were identified in Figure 12: δ 0.87 (multiplet), δ 1.33 (sextet), δ 1.56 (quintuplet), δ 3.12 (multiplet), δ 3.70 (doublet), and δ 4.70 (singlet). Although many of the signals were highly coupled making them difficult to interpret, the chemical shifts observed are consistent with the type of bonds present in IP. The δ 0.87, and δ 1.33 chemical shifts are characteristic alkyl bonds for methyl and methylene groups, respectively. The δ 1.56 chemical shifts correspond to the allylic carbon atoms adjacent to double bonded carbon atoms and the δ 3.70 chemical shift is caused by the carbon-oxygen bonds. Finally, there is the signal at δ 4.70 which is the deuterium oxide solvent and the signals at δ 3.12 which are likely aliphatic hydroxyl groups caused by residual isopentenol from the IP recovery and purification steps.

In addition to ^{1}H NMR, ^{31}P NMR was also used to quantify the structure of IP by analyzing the phosphate group. The following ^{31}P NMR signals were identified in Figure 13: δ 33.24, δ 3.49, δ 2.29, δ -7.58, δ -10.44, and δ -21.65. Although ^{31}P NMR features a larger range for signals compared to ^{1}H NMR, the signals in Figure 13 are all within the range suitable for a phosphate group bound to four oxygen atoms. While the ^{1}H and ^{31}P NMR results cannot conclusively confirm the success of IP synthesis, the results in Figures 12 and 13 corroborate the NMR signals expected for IP, and preliminary enzymatic assays utilizing IP as a substrate were successful and so the synthesis procedure was presumed to be successful. Additionally, the recovered IP was weighed and determined to have a 43.2 % yield relative to the theoretical maximum which is similar to other phosphate monoesters synthesized by the phosphorylation of alcohols which ranged from 43-86 % (Lira et al., 2013). However, it should be noted that the yield based on gravimetric analysis does not account for the purity of IP.

5.3. The Effects of Enzyme Entrapment on ALP Activity

Before studying the effects of enzyme entrapment on the IUP enzymes which are not commercially available or abundantly characterized in the literature, ALP was selected as a model enzyme to characterize the effects of enzyme entrapment due to its simple Michaelis-Menten kinetics given in Table 5, as well as its vast coverage in the literature and ease of spectrophotometric product detection.

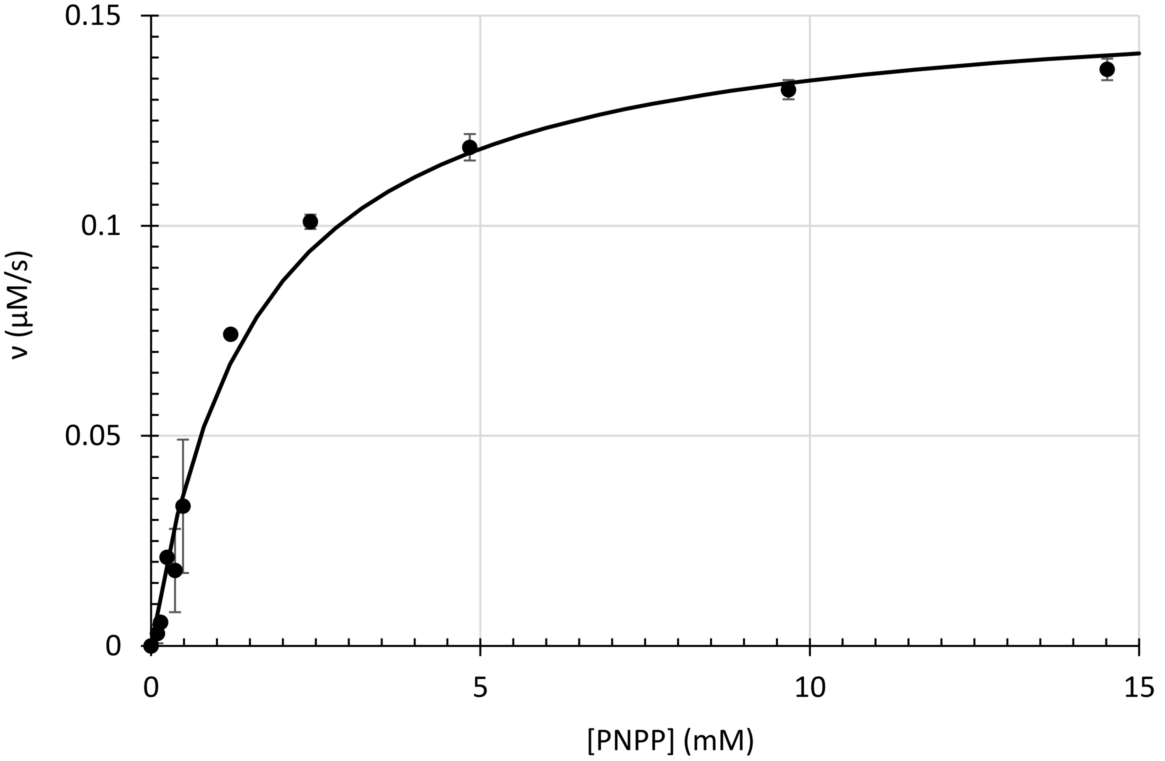

Figure 14: Michaelis-Menten plot of free ALP at an enzyme concentration of 0.6 µM in 1.0 M DEA, 0.5 mM $MgCl_2$ buffer at 37 °C and a pH of 9.8. The kinetic parameters were fit using the ALP kinetic model given in Table 5 and the fitted $kcat_0$ and Km_0 parameters were $0.26 \pm 0.02\ s^{-1}$ and 1.59 ± 0.01 mM respectively. Each data point is the average of two samples (error bars 1 σ).

Before characterizing the activity of the immobilized enzymes and determining the immobilization efficiency, the activity of free ALP in solution was characterized using PNPP as a substrate and spectroscopically monitoring the formation of NP at a wavelength of 405 nm. As shown in Figure 14, the simple Michaelis-Menten kinetic model for ALP given in Table 5 was able to model the experimental rate of reaction with a high degree of correlation. The coefficient of determination calculated using Equations 7-9 was high at a value of 0.98 and the confidence intervals calculated using Equations 11 and 12 for the turnover rate ($k_{cat,0}$) and binding affinity ($K_{m,0}$) parameters respectively were narrow at only 0.26 ± 0.02 s^{-1} and 1.59 ± 0.01 mM. The experimentally determined substrate binding affinity of ALP in 1.0 M DEA, 0.5 mM $MgCl_2$ buffer at 37 °C and a pH of 9.8 also agrees reasonably well with the assay literature value. Chappelet-Tordo et al. (1974) tested the activity of intestinal ALP with the substrate PNPP in 0.16 M ethanolamine, 0.4 M NaCl buffer at 25 °C, and a pH of 10.0, and found the binding affinity to be 1.5 mM. Although the operating conditions available in the literature vary slightly from those used in this study, the effect of temperature on the substrate binding affinity, while largely unpredictable for different enzyme-substrate pairings, is often minimal below the enzyme degradation temperature and negligible compared to more pronounced effects caused by the buffer and pH (Scopes, 1995). These varying factors explain why the reported substrate binding affinity varies from the literature value, however since the variation is small, the activity of the ALP tested in this study was said to follow the expected kinetics given in the literature (Chappelet-Tordo et al., 1974). Since the value of the turnover rate depends highly on the substrate, temperature, enzyme source, and enzyme purity, its values are highly variable throughout the literature and so any meaningful interpretation of the turnover rate should be relative between kinetic studies using the same enzyme source and operating conditions. Due to the immobilization efficiency defined in Equation 15 assuming a constant turnover rate for both the free and immobilized enzyme assays, any shift in the turnover rate due to improved enzyme stability from immobilization would be accounted for by the immobilization efficiency and so the modelled turnover rate does not require interpretation beyond its use for kinetic modelling or its contributory effect on the value of the immobilization efficiency which is minimal relative to the predominant internal diffusion limitations.

To quantify the kinetics of immobilized ALP, the enzyme free in solution was added to the B9R-2-Black methyl-methacrylate-based monomer resin and 3D-printed by stereolithography to produce an entrapped ALP-PMMA matrix of microwells for batch immobilized enzyme assays.

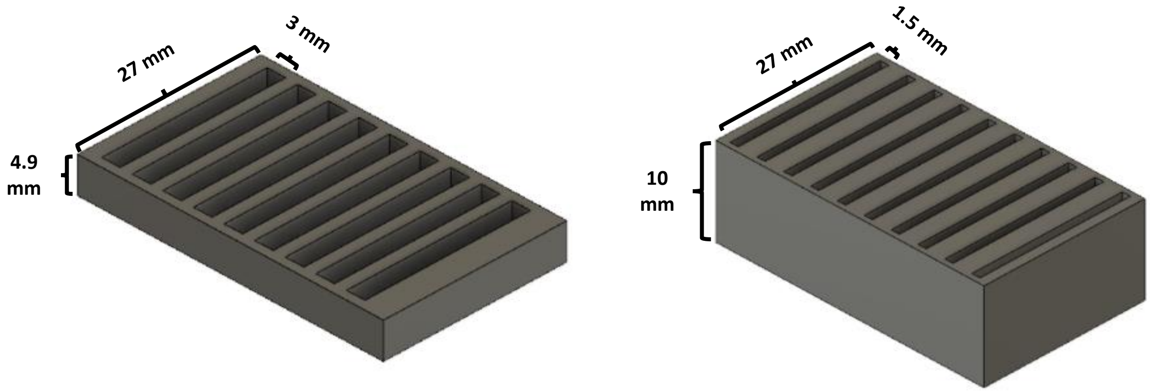

a)

b)

Figure 15: CAD files of 3D-printed wells for immobilized ALP assays. a) 27x3x4.9 mm square wells having a reaction volume of 400 µL and a SA:V ratio of 943 m²/m³. b) 27x1.5x10 mm triangle wells having a reaction volume of 210 µL and a SA:V ratio of 2666 m²/m³.

Two microwell configurations shown in Figure 15 were designed having a SAV ratio of 943 and 2666 m^2/m^3, respectively.

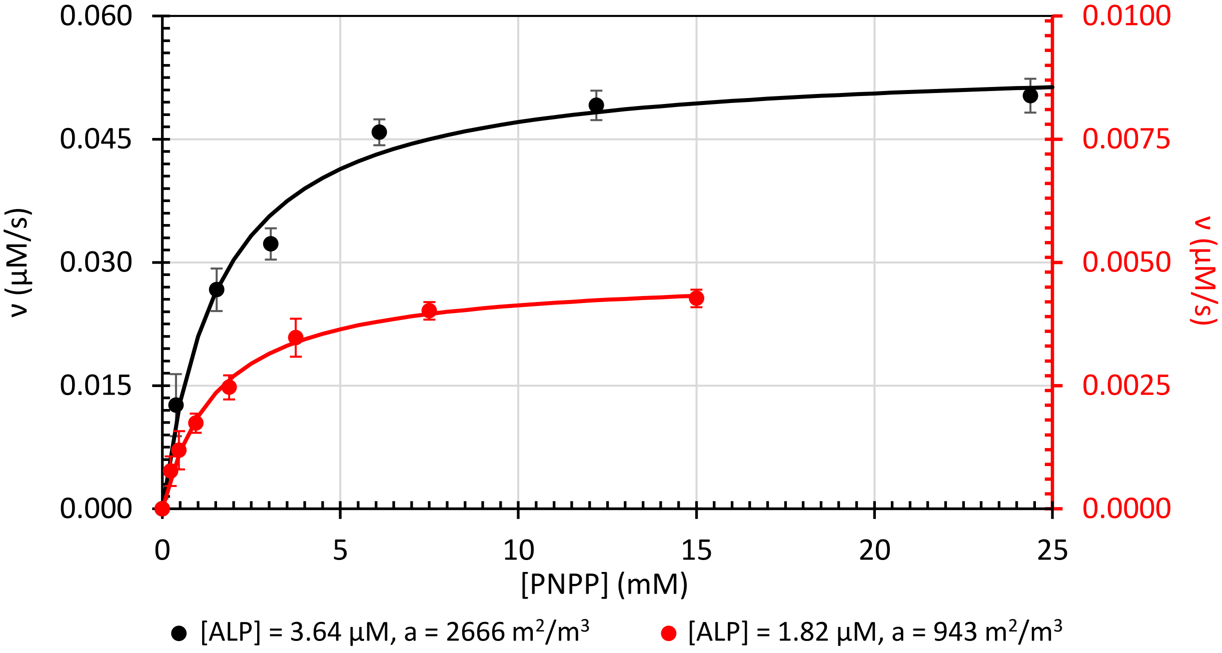

Figure 16: Michaelis-Menten plot of immobilized ALP assays having varying SA:V ratios and enzyme concentrations in 1.0 M DEA, 0.5 mM $MgCl_2$ buffer at 37 °C and a pH of 9.8. The fitted value of the immobilization efficiencies and the binding affinity of PNPP were estimated using Equations 15 and 17 respectively, along with Equations 7-9 for regression. The modelled immobilization efficiency, substrate binding affinity, and coefficient of determination were 0.010 ± 0.001, 1.54 ± 0.03 µM, 0.996 and 0.057 ± 0.002, 1.60 ± 0.01 µM, and 0.998 for the 3.64 µM and 1.82 µM ALP assays, respectively. Each data point is the average of two samples (error bars 1 σ).

The immobilized enzyme assays were additionally tested at two different enzyme concentrations to investigate the effects of the SA:V ratio and enzyme concentration simultaneously. Finally, the substrate binding affinity parameter was included along with the immobilization efficiency during the regression of Equation 15 to evaluate if any significant shift in the binding affinity was observed during immobilization.

Table 6: Summary of immobilized ALP kinetic assay fitted parameters.

[ALP] (μM)	**a (m^2/m^3)**	**$K_{m,0}$ (μM)**	$\boldsymbol{\eta_{ALP}}$	$\boldsymbol{\hat{\eta}(a)_{ALP}}$ **a = 2666 m^2/m^3**	**R^2**
1.82	943	1.54 ± 0.03	0.010 ± 0.001	0.028 ± 0.003	0.996
3.64	2666	1.60 ± 0.01	0.057 ± 0.002	0.057 ± 0.002	0.998

The immobilized Michaelis-Menten kinetic plots from the ALP immobilized enzyme assays are given in Figure 16, and the assay variables, fitted kinetic parameters, and coefficients of determination are summarized in Table 6. Comparing the values for the fitted immobilized substrate binding affinities of 1.54 ± 0.03 and 1.60 ± 0.01 μM to the free enzyme assay having a value of 1.59 ± 0.01 μM, there was no significant shift in the substrate binding affinity associated with the immobilization procedure. This was the expected result based on the entrapment immobilization method utilized since the enzyme is encapsulated preserving its conformation, unlike other immobilization procedures such as covalent bonding which alter the conformation and affect the substrate binding affinity. Although a slight, favourable shift in the substrate binding affinity from 1.59 ± 0.01 μM to an average of 1.54 ± 0.03 μM was observed for the kinetics derived in Figure 16, the difference was only 3.1 % which is small. Since enzyme entrapment is expected to have a negative effect, if any, on the substrate binding affinity, the improvement in the binding affinity was likely caused by experimental uncertainty within the derived kinetic models. Therefore, the assumption made in Equation 15 that the immobilized kinetics are described by the free enzyme kinetics having a constant binding affinity and an applied immobilization efficiency to account for internal diffusion limitations, was a reasonable assumption corroborated by the ALP immobilized enzyme assays summarized in Table 6.

With the immobilization procedure having a negligible effect on the substrate binding affinity, the factors affecting the immobilization efficiency (and therefore immobilized kinetics) such as the enzyme concentration and SA:V ratio were investigated. For Equation 15 to be applicable for the estimation of the immobilization efficiency, external diffusion effects must be negligible and only the internal diffusion effects caused by enzyme entrapment considered. Since the immobilized enzyme kinetics were based on the free enzyme kinetics given in Equation 15, the rate of reaction was expected to increase linearly with the enzyme concentration as long as the saturation threshold preventing ALP from becoming entrapped in the polymer matrix was not reached. Additionally, as shown in Equation 17, as the SA:V ratio is increased, the immobilization efficiency must increase proportionally to maintain the same rate of reaction.

Intuitively this is equivalent to the volumetric rate of reaction varying linearly with the surface area since there are proportionally more enzyme active sites available for the substrates to react at as the SA:V ratio is increased. Taking the proper precautions during the immobilized kinetic assays such as using high reaction SA:V ratios and gentle shaking to promote mixing, the fitted immobilization efficiencies are expected be linearly extrapolatable with respect to the enzyme concentration and SA:V ratio if no external diffusion effects are significant.

For the immobilized enzyme assays summarized in Table 6, the immobilization efficiency was 0.010 ± 0.001 at a low SA:V ratio of 943 m^2/m^3 and enzyme concentration of 1.82 µM, whereas the immobilization efficiency at double the enzyme concentration and a high SA:V ratio of 2666 m^2/m^3 was over 5-fold higher at 0.057 ± 0.002. By normalizing the immobilization efficiency of the low SAV assay to a value of 2666 m^2/m^3 for comparison between the assay conditions, the normalized immobilization efficiency at an enzyme concentration of 1.82 µM was 0.028 ± 0.003. This value is half of that determined experimentally for an enzyme concentration of 3.64 µM and SA:V ratio of 2666 m^2/m^3 which supports that external diffusion effects were negligible and both the enzyme concentration and SA:V ratio are linearly proportional to the immobilization efficiency. The effects of increasing surface area having a linear effect on entrapped enzyme activity was also observed by Blanchette et al. (2016) while studying the entrapment of PMMO in a PEG-DA based hydrogel. Although using the volumetric rate of reaction to evaluate the effects of internal/external diffusion is not ideal such as quantitatively measuring the experimental diffusivity coefficients and applying a dimensionless group such as the Damköhler Number for analysis, experimentally estimating the diffusivity coefficients was outside the scope of this project and literature data was not readily available for many of the substrates and products used in this study. With that stated, all else being equal between the two immobilized ALP assays with regards to external diffusion such as the substrate concentration range, operating conditions, and species transport properties, the main contributing factor towards external diffusion limitations was the mean diffusion path length throughout the wells. Considering the geometry of the wells in Figure 15, and assuming 1-dimensional diffusion from the center of the well, the average minimum diffusion path length based on the geometry in Figure 15 was 1.5 mm for a SA:V ratio of 943 m^2/m^3 and 0.374 mm for a SA:V ratio of 2666 m^2/m^3 (the triangle well ranges from 0 at the tip of the well to 0.748 mm at the base of the triangle). Although simplified to only consider optimal 1-dimensional diffusion of the diffusion-limiting substrate molecules furthest from the immobilized enzymes, the well configuration having a high SA:V ratio is notably preferable due to shorter diffusion pathlengths. If diffusion limitations were present, all else being equal or normalized such as the SA:V ratio and enzyme concentration, the low SA:V ratio well configuration would be expected to have a significantly reduced immobilization efficiency relative to the high SA:V ratio wells due to longer mean substrate diffusion lengths throughout the wells. Since this effect was not observed, and the immobilization efficiency varied linearly with the enzyme concentration and SA:V ratio, as expected, the ALP assays were kinetically limited and suitable for estimating the immobilization efficiencies.

The calculated ALP immobilization efficiency of 0.057 ± 0.002 for an enzyme concentration of 3.64 µM and a SA:V ratio of 2666 m^2/m^3 was similar to literature values which had an immobilization efficiency ranging from 0.06-0.14 for ADH, BFD, and β-galactosidase immobilized in a PEG-DA polymer matrix (Shmieg et al., 2019). Based on the results of the immobilized ALP enzyme assays, to achieve increased immobilization efficiencies, the design of an immobilized enzyme microfluidic reactor for monitoring enzyme stability should use the maximum SA:V ratio possible to limit external diffusion limitations and promote increased product yields.

5.4. COMSOL Multiphysics Modelling of Immobilized ALP Microfluidic Reactor

Having experimentally characterized the free and immobilized enzyme kinetics of ALP to model the values of the turnover rate, substrate binding affinity, and immobilization efficiency (for a given SA:V ratio), a COMSOL Multiphysics model was developed to predict the initial steady-state product concentration of NP. The motivation to develop an immobilized ALP microfluidic reactor model in COMSOL Multiphysics was not necessarily for the intuitive reasons such as predicting concentration profiles or running simulations, albeit useful, but rather to access the validity of the COMSOL Multiphysics model assumptions and constraints previously outlined by comparing the COMSOL Multiphysics model with experimental results. If the COMSOL Multiphysics model matches the experimental results within an acceptable margin of error, then the model is validated and may be extended to more complex cascade reactions such as the sequentially immobilized IUP. However, if the COMSOL model does not accurately predict the experimental results for the immobilized ALP microfluidic reactor then the model assumptions and constraints must be reviewed and revised in pursuit of a suitable model corroborating the experimental results.

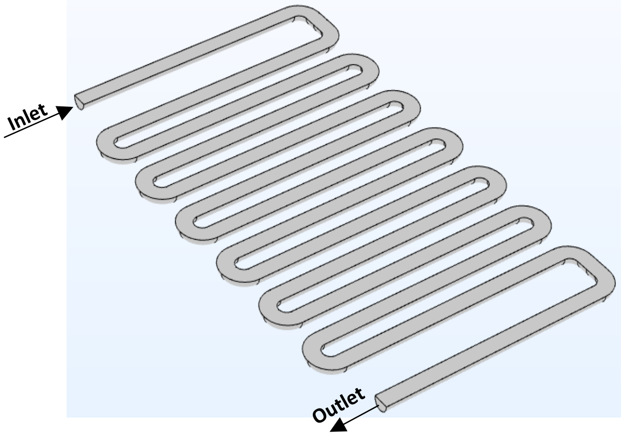

Figure 17: Geometry of the modelled microfluidic reactor in COMSOL Multiphysics with a reactor length of 388 mm, diameter of 1.5 mm, and 90 ° elbows (A radial plane of symmetry along the longitudinal length of the reactor was used to split the modeled geometry in half).

For modelling in COMSOL Multiphysics, the microfluidic reactor CAD file prepared for 3D-printing was split axially along the longitudinal length of the reactor as shown in Figure 17 and a plane of symmetry was applied to simplify the complexity of the model. The boundary conditions were specified as previously described in the *COMSOL Multiphysics Modelling, Assumptions, and Constraints* section. The molar flux boundary condition along the reactor walls was defined using Equation 18 with the previously determined mean kinetic parameters ($k_{cat,0} = 0.26\ s^{-1}$ and $K_{m,0} = 1.59\ \mu M$) along with the mean extrapolated immobilization efficiency ($\hat{\eta}_0 = 0.028$) at an enzyme concentration of 1.82 µM and SA:V ratio of 2666 m^2/m^3.

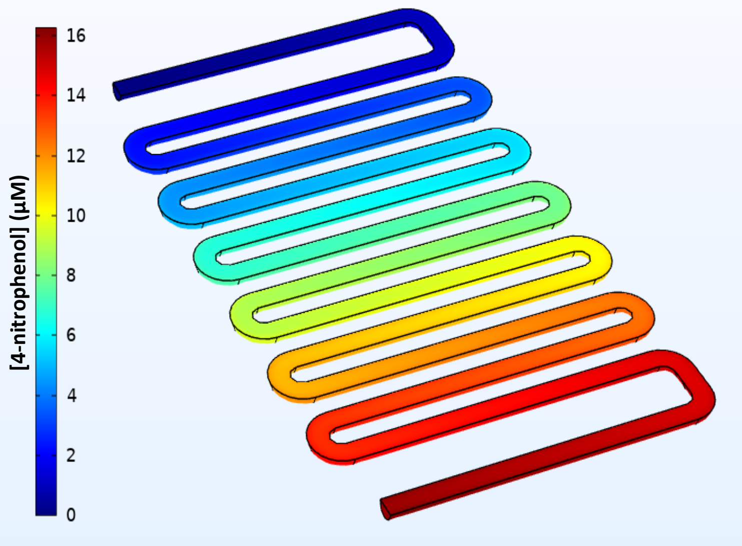

Figure 18: Modelled COMSOL Multiphysics concentration profile of NP for the microfluidic reactor tested experimentally having a SA:V ratio of 2666 m^2/m^3 and a 15 mM PNPP feed stream at 37 °C (see Figure 17 for reactor details).

As shown in Figure 18, the predicted concentration of NP increased throughout the microfluidic reactor as PNPP from the feed stream reacted with the immobilized ALP modelled as a boundary flux condition along the walls of the reactor. Since the reactor was designed to be kinetically limited by selecting a high SA:V ratio and a relatively long residence time of 2 h, the predicted concentration of NP at steady-state was approximately constant along a given reactor cross section and variable radial diffusion was not observed. The predicted productivity and outlet NP concentration of the COMSOL Multiphysics model were 0.133 µM/min and 16.0 µM, respectively.

5.5. Experimental Results of Immobilized ALP Microfluidic Reactor

To test the stability of the immobilized ALP, a microfluidic reactor was designed in CAD and 3D-printed for continuous operation.

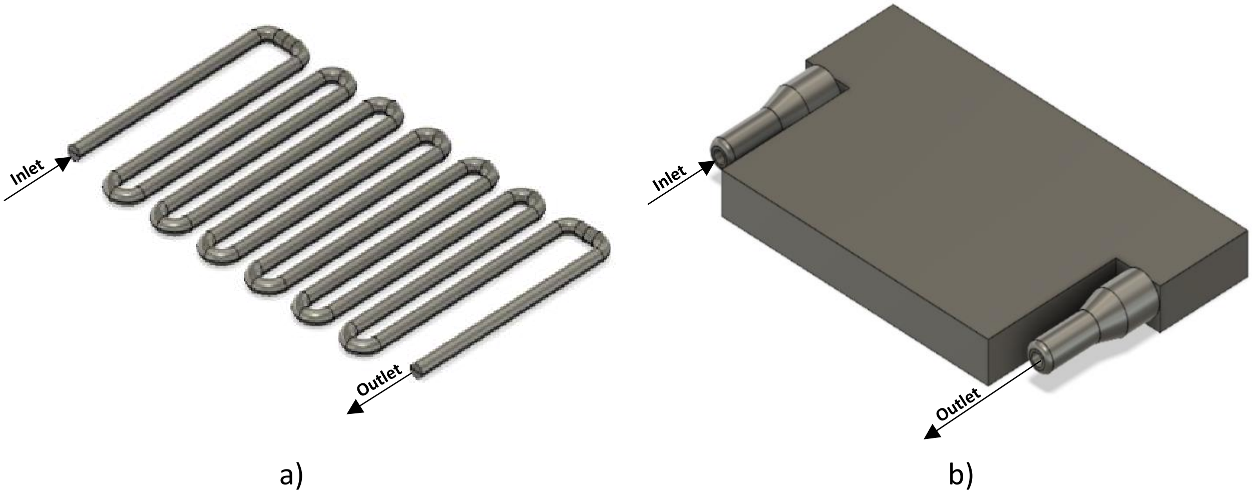

a) b)

Figure 19: a) CAD of a microfluidic reactor having a reactor length of 388 mm, diameter of 1.5 mm, and 90 ° elbows b) CAD of encased microfluidic reactor from a) with barbed fittings for piping connections.

The geometry and configuration of the 3D-printed microfluidic reactor are shown in Figure 19. Preliminary tests investigating the precision of the 3D-printer found that short 500 µm diameter microchannels could be printed without any blockage, however for the proposed microfluidic reactor having a length of 358.4 mm, rinsing and removing the residual monomer solution from the microchannel proved problematic for narrow diameter microchannels. For this reason, a diameter of 1.5 mm was selected since it has a relatively high SA:V ratio of 2666 m^2/m^3 but was wide enough to effectively wash the residual monomer solution from the reactor. The length and winding configuration of the reactor were designed to maximize the length of the reactor within the 2-dimensional build area of the B9Creator 3D-printer. ALP was entrapped simultaneously during 3D-printing at a concentration of 1.84 µM and the microfluidic reactor was washed in

1.0 M DEA, 0.5 mM $MgCl_2$ buffer at a pH of 9.8 for 36 h at 4 °C prior to beginning continuous operation. The microfluidic reactor was connected to a Harvard Apparatus 11 Plus syringe pump using 1.6 mm silicone tubing at the reactor inlet and samples were collected at the reactor outlet for analysis by UV-Vis spectrophotometry at a wavelength of 405 nm to monitor the concentration of NP. To reduce experimental error, the flowrate was set to a low value of 5.28 µL/min resulting in a relatively long residence time of 2 h which was selected to ensure that the reactor did not have external diffusion limitations and that sufficient NP would be produced to avoid increased experimental error due to low product detection. For the quantification of NP leaving the reactor, 2 µL samples were collected and the absorbance was measured similar to the free and immobilized assays previously described with the exception that a Biotek Take3 micro-volume plate was used instead of a 96-well plate. Periodic blank samples were also collected using a tee valve at the reactor inlet to account for changes in the feed composition caused by the natural reaction of PNPP to slowly produce NP at 37 °C. Additionally vials of the feed stream were monitored over the course of 2 h at 37 °C corresponding to the residence time of the reactor to determine if the natural reaction of PNPP to produce NP was significant. However, its effect were negligible compared to the kinetics of ALP which produced NP an average of two orders of magnitude faster (data not shown). Therefore, the natural reaction of PNPP to NP had a minimal effect on the inlet composition over the course of a few hours but became significant over the span of several days so blank samples were conservatively monitored a few times daily.

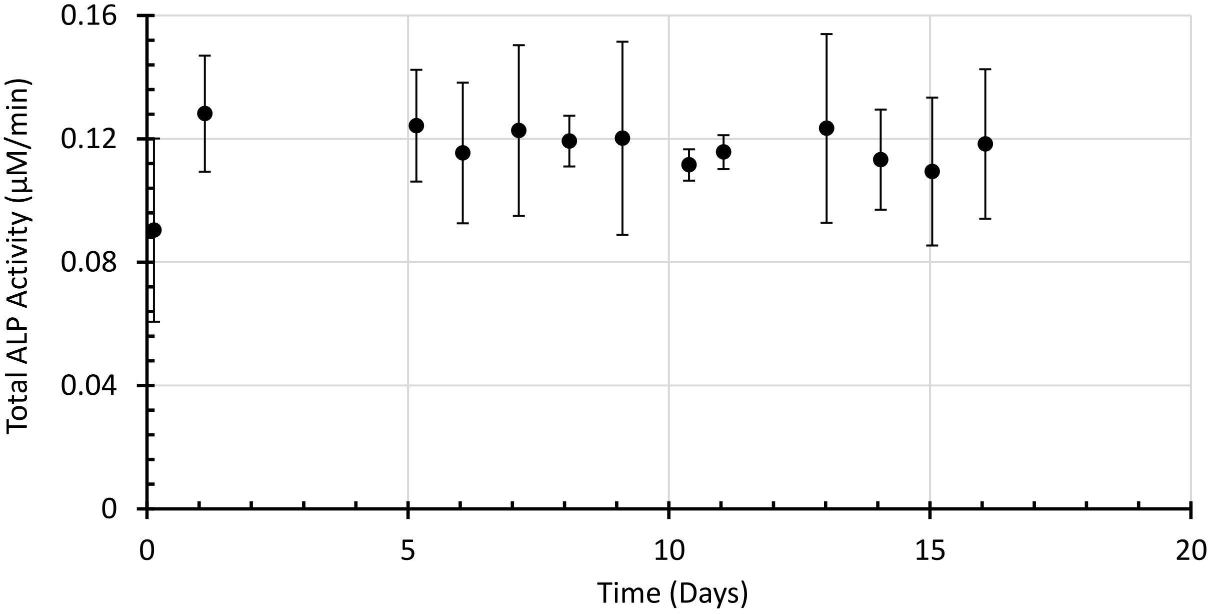

Figure 20: Immobilized ALP microfluidic reactor enzyme stability plot for a 15 mM PNPP feed stream in 1.0 M DEA, 0.5 mM $MgCl_2$ buffer at a pH of 9.8 and temperature of 37 °C (see Figure 19 for reactor details). Each data point is the average of 12-28 readings except for Days 11 and 12 which only had 8 readings each (error bars 1 σ).

To test the stability of ALP, a feed stream of PNPP at a concentration of 15 mM (approximately 10 times the modelled substrate binding affinity) was selected to ensure saturated kinetics. This prevented external substrate diffusion limitations within the reactor since the bulk concentration of PNPP remained approximately constant, while also achieving the highest rate of NP formation for a given ALP concentration and reactor configuration. A time series plot of the total volumetric ALP activity based on the quantification of NP at the microfluidic reactor outlet is given in Figure 20. Based on the results in Figure 20, the initial transient phase lasted over 8 h during initial monitoring which was due to the long residence time of 2 h and the presumably slow displacement rate of the residual wash buffer with fresh PNPP from the feed stream diffusing within the pores of the immobilized polymer matrix. By the first day of operation steady-state had been reached achieving a maximum mean ALP activity of 0.128 ± 0.030 µM/min and outlet NP concentration of 15.4 ± 3.6 µM. Despite the experimentally determined results having relatively large uncertainties due to the sampling and detection methods used, the COMSOL Multiphysics model having a mean ALP activity of 0.133 µM/min and outlet concentration of 16.0 µM accurately predicted the mean experimental productivity and outlet concentration of NP with only a 3.9 % relative error. This supports the use of COMSOL Multiphysics as an effective modelling tool for the simulation of immobilized enzymatic microfluidic reactors and validates the model assumptions and constraints outlined in the *COMSOL Multiphysics Modelling, Assumptions, and Constraints* section. Additionally, since the modelling of a sequentially immobilized cascade enzymatic microfluidic reactor is simply a series of partitioned single enzymatic steps, the single enzyme model developed for ALP can be extended to include cascade reactions by simply adjusting the spatial surface flux boundary conditions to reflect each spatially distributed sequential enzymatic step and considering any possible inhibitory effects from upstream metabolites on downstream enzymatic reactions. It should be mentioned that the validity of the immobilized ALP COMSOL Multiphysics model is contingent on the primary assumption that external diffusion is negligible, and the system is kinetically limited. For this reason, extension of the developed ALP COMSOL Multiphysics model to a sequentially immobilized cascade enzymatic system must be taken with care and a reasonable margin of safety to ensure that external diffusion, intrinsic to the definition and application of the immobilization efficiency given in Equation 15, remains negligible.

As shown in Figure 20, after 16 days of continuous operation, the mean ALP activity was reduced to 0.118 ± 0.024 µM/min, however a slightly lower value of 0.109 ± 0.023 µM/min was observed the day before. The average activity retained during continuous use for ALP over the span of 16 days was relatively high at 85.4-92.3 % of its initial mean activity. The activity was also monitored after continuous operation during a period of extended storage at 4 °C in 1.0 M DEA, 0.5 mM $MgCl_2$ buffer at a pH of 9.8. After storage for 82 days, the reactor was run continuously again with a feed stream of 15 mM PNPP and monitored until steady-state was reached. The activity of ALP was then monitored by the concentration of NP at the reactor outlet and was determined to retain 54.2 % of its initial activity before storage having a mean enzyme activity of 0.064 µM/min. Overall the immobilized enzyme reactor had high stability and only lost approximately 0.48-0.91 % and 0.55 % enzyme activity per day during continuous operation and low-temperature storage, respectively. Assuming that the combined rate of enzyme degradation and/or leaking from the reactor was approximately linear with respect to time (based on the results given in Figure 20), the observed activity half-life which estimates the lifespan of the immobilized microfluidic reactor before it should be replaced, was 55-104 days during continuous operation (equivalent to a minimum of 660 reactor cycles) and 91 days during storage.

Although utilizing entrapment as the method of immobilization introduced significant internal diffusion limitations resulting in relatively low immobilization efficiencies, the immobilized ALP maintained excellent stability during operation and storage. Relative to other enzyme entrapment studies, the stability of immobilized ALP was consistent with the immobilization of dehydrogenases in an alginate-silicone dioxide composite gel which retained up to 76.2 % activity after 60 days of storage (Xu et al., 2006), and was much improved relative to the entrapment of PMMO in a PEG-DA-based hydrogel which lost approximately 43.5 % of its activity after 20 cycles (80 min of intermittent operation) (Blanchette et al., 2016), and the co-immobilization of GOD and HRP in a PEG-DA-based hydrogel which lost approximately 12 % of its initial activity after 7 days of storage at 4 °C (Heo & Crooks, 2005). The stability of entrapped ALP was also much higher than many of the covalent bonding immobilization procedures for 3D-printable supports which were typically prone to poor stability due to undesirable enzyme conformational changes and binding during operation (Cerqueira et al., 2015; Cerdeira Ferreira et al., 2013; Ogończyk et al., 2012; Su et al., 2016). With that said, optimized covalent binding immobilization procedures for specific enzyme-support systems such as the covalent co-immobilization of cholesterol esterase, cholesterol oxidase, and peroxidase on PVC had excellent enzyme stability with an activity half-life of 100 days (Chauhan & Pundir, 2011) similar to the activity half-life of 55-104 days determined for ALP in this study.

5.6. Activity and Kinetic Modelling of Free IUP Enzymes

After synthesizing and purifying CK, IPK, IDI, IspA, and ADS, the concentration of the IUP enzyme stock solutions were determined using a DC protein assay. Free enzyme assays were performed for the IUP enzymes to model the turnover rate and substrate binding efficiency values for each enzyme except for IDI which catalyzes an isomerization reaction that is not easily monitored by UV-vis spectroscopy. The free enzyme assays were performed to provide a comparative basis for the immobilized enzyme assays and to compare the determined free enzyme kinetic parameter values with literature references. The activity of CK and IPK were monitored using a coupled enzyme assay dependant on the concentration of the by-product ADP, and IspA and ADS were monitored using a coupled enzyme assay dependant on the concentration of the by-product PPi.

Table 7: Experimentally determined and literature values for the IUP kinetic parameters of the reaction rates given in Table 5.

Enzyme (*Origin*)	**Substrate(s)**	**Kinetic Parameter**	**Experimental Value**	**Reference Value**	**Reference**
Choline Kinase (*S. cerevisiae*)	ISP + ATP	$k_{cat,1}$ (s^{-1})	0.0037	0.0041	Chatzivasileiou et al., 2019
		$K_{M,1a}$ (μM)	3886	4539	
		$K_{M,1b}$ (μM)	139.7	140	Brostrom & Browning, 1973
Isopentyl pyrophosphate kinase (*A. thaliana*)	IP + ATP	$k_{cat,2}$ (s^{-1})	0.013	0.013	Ward et al., 2019
		$K_{M,2a}$ (μM)	21.5	21.7	
		$K_{M,2b}$ (μM)	43.8	43.5	
Isopentenyl delta isomerase (*E. coli*)	IPP/DMAPP	$k_{cat,3}$ (s^{-1})	-	0.33	Hahn et al., 1999
		$K_{M,3a}$ (μM)	-	9.5	
		$K_{M,3b}$ (μM)	-	14.3	
Farnesyl pyrophosphate synthase (*E. coli*)	IPP + DMAPP	$k_{cat,4}$ (s^{-1})	0.0068	0.0052[†]	Ku et al., 2005
		$K_{M,4a}$ (μM)	20.6	29.3	
		$K_{M,4b}$ (μM)	1.19	1.3	
	IPP + GPP	$k_{cat,5}$ (s^{-1})	0.0048	0.0115[†]	
		$K_{M,5a}$ (μM)	5.65	5.5	
		$K_{M,5b}$ (μM)	8.63	10.3	
Amorphadiene Synthase (*A. annua*)	FPP	$k_{cat,6}$ (s^{-1})	0.0035	0.0043	Picaud et al., 2005
		$K_{M,6}$ (μM)	1.91	2.0	

[†] Assuming the molecular weight of IspA to be 32 kDa.

The values of the experimentally determined fitted free enzyme kinetic parameters based on the kinetic models given in Table 5 are summarized and compared with the kinetic parameters determined under similar operating conditions from literature references in Table 7. The fitted free enzyme kinetic parameters modelled in this study had relatively high coefficient of determination values of 0.86, 0.99, 0.89-0.95, and 0.89 for CK, IPK, IspA, and ADS respectively which suggests the models proposed in Table 5 were effective for estimating the reaction rate of the IUP enzymes. Comparing the experimentally determined substrate binding affinity values with the literature values listed in Table 7, the values determined in this study agree with the literature reasonably well. All the experimentally determined substrate binding affinity values were on the same order of magnitude as their respectively literature value comparisons, with the largest differences occurring for IspA and the determination of $K_{M,4a}$ and $K_{M,5b}$. In both cases, the experimentally determined substrate binding affinities were lower than the literature values determined by Ku et al. (2005) which was expected since a higher concentration of magnesium (Mg^{2+}) was used in this study. Magnesium is an important cofactor required to form the ligated metal complexes required for the ternary complex of IspA (Hosfield et al., 2004) and has been shown to have a significant effect towards increasing isoprenoid pathway flux at increased concentrations (Ward et al., 2019). Although less quantitative for the purpose of comparison due to variations caused by enzyme purity and activity, the enzyme turnover rate of CK, IPK, IspA, and ADS were on the same order of magnitude and similar to those reported in the literature.

5.7. Activity and Kinetic Modelling of Immobilized IUP Enzymes

Similar to the free enzyme assays, the activity of immobilized CK and IPK were characterized using a coupled enzyme assay dependent on the concentration of ADP, and IspA and ADS were characterized using a coupled enzyme assay dependent on the concentration of PPi.

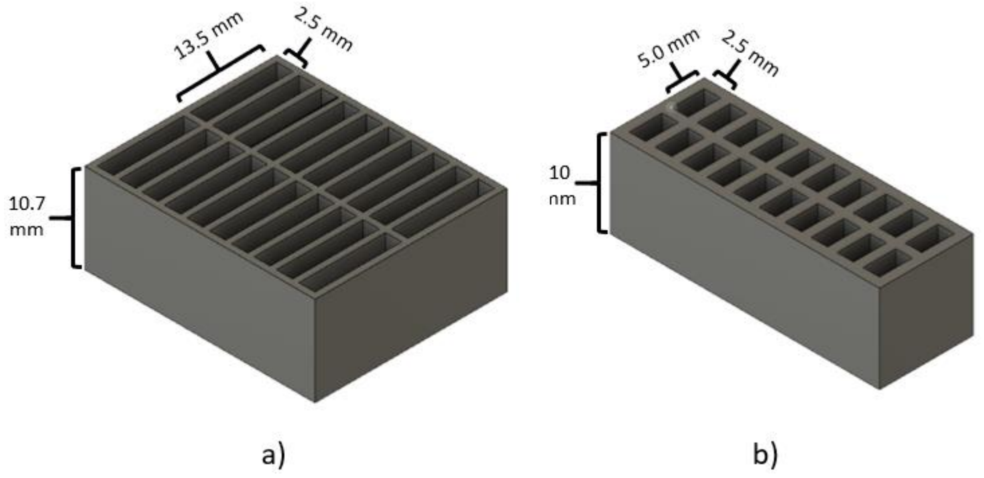

Figure 21: CAD well configurations for the immobilized IUP enzyme assays. a) 13.5x2.5x10.7 mm square wells having a reaction volume of 360 µL and a SA:V ratio of 1041 m^2/m^3. *b) 5.0x2.5x9.6 mm square wells having a reaction volume of 120 µL and a SA:V ratio of 1300* m^2/m^3.

Based on the assay protocols and desired assay volume, two well configurations for simultaneous 3D-printing enzyme entrapment were designed in Fusion 360 as shown in Figure 21. The ADP-coupled immobilized enzyme assays were run using a reaction volume of 360 µL and SA:V ratio of 1041 m^2/m^3 (Figure 21a), and the PPi-coupled immobilized enzyme assays were run using a reaction volume of 120 µL and SA:V ratio of 1283 m^2/m^3 (Figure 21b).

Table 8: Experimentally determined values for the immobilization efficiency and normalized immobilization efficiency defined in Equations 15 and 17 respectively for the IUP enzymes.

Enzyme	E_0 (µM)	a (m^2/m^3)	η	$\hat{\eta}(a)$ (a = 2666 m^2/m^3)	R^2
CK	0.21	1041	0.096 ± 0.010	0.249 ± 0.026	0.79
IPK	0.09	1041	0.085 ± 0.011	0.218 ± 0.028	0.78
IDI	-	-	-	0.186[†]	-
IspA	0.15	1283	0.069 ± 0.003	0.142 ± 0.006	0.90
ADS	0.11	1283	0.066 ± 0.005	0.135 ± 0.010	0.99

[†] This value was estimated based on the average normalized immobilization efficiencies of the other IUP enzymes for subsequent COMSOL Multiphysics modelling due to the absence of experimental or literature values.

The values of the experimentally determined immobilization efficiency and normalized immobilization efficiency for a microfluidic reactor having a diameter of 1.5 mm (equivalent to a SA:V ratio of 2666 m^2/m^3) are summarized for the IUP enzymes in Table 8. Since enzyme entrapment often results in significant internal diffusion limitations lowering enzyme activity, the observed mean immobilization efficiency values ranging from 0.066-0.096 were relatively low with less than 10 % activity retained during immobilization. These values are within the range reported in the literature for the enzyme entrapment of ADH, BFD, and β-galactosidase in a PEG-DA-based hydrogel which had immobilization efficiencies ranging from 0.060-0.140 (Schmieg et al., 2019). Although similar results were obtained in this study at the tested SA:V ratios of 1041 and 1283 m^2/m^3, the significant effect of the SA:V ratio on enzyme activity reported in this study, among others (Blanchette et al., 2016), was not considered by Schmieg et al. (2019); presumably due to the inconsistencies and defects associated with the soft lithography procedure used for hydrogel formation. The use of stereolithography in this study enabled precise 3D-printing and accurate enzyme support geometries. This allowed for reproducible results and reasonably high values of the regression coefficient of determination ranging from 0.78-0.99 for the immobilized enzyme assays as shown in Table 8. The immobilized enzyme assays were prone to slightly increased error relative to the free enzyme assays summarized in Table 7 due to difficulties washing the residual resin from the assay wells. The residual methyl methacrylate monomer is normally dissolved in isopropanol for removal, however, to preserve the activity of the immobilized enzymes, the wells were washed in buffer solution and consequently some methyl methacrylate remained in solution and interfered with the spectroscopic kinetic assays. Additionally, evaporation and the capillary action of the solution within the assay wells to form a convex meniscus increased the experimental error by reducing the reaction volume and causing fluctuations in the true SA:V ratio of the assay, respectively. Although the immobilized kinetic assays at 1041 and 1283 m^2/m^3 resulted in relatively low activity as observed by the immobilization efficiency values, by normalizing the immobilization efficiency to a higher SA:V ratio of 2666 m^2/m^3 consistent with an immobilized enzyme microfluidic reactor having a 1.5 mm diameter microchannel, the immobilization efficiencies in Table 8 increase over two-fold to more acceptable levels for reactor design ranging from 0.135-0.249 on average.

5.8. Quantification of β-caryophyllene and Amorphadiene by GC-MS

For quantification of amorphadiene synthesized from the cascade IUP enzymatic reaction, 90 mg/L β-caryophyllene was used as an internal standard during GC-MS. Due to the unavailability of commercial amorphadiene standards, the enzymatic reaction of FPP catalyzed by ADS previously characterized kinetically in Table 7 was used to synthesize amorphadiene for characterization by GC-MS.

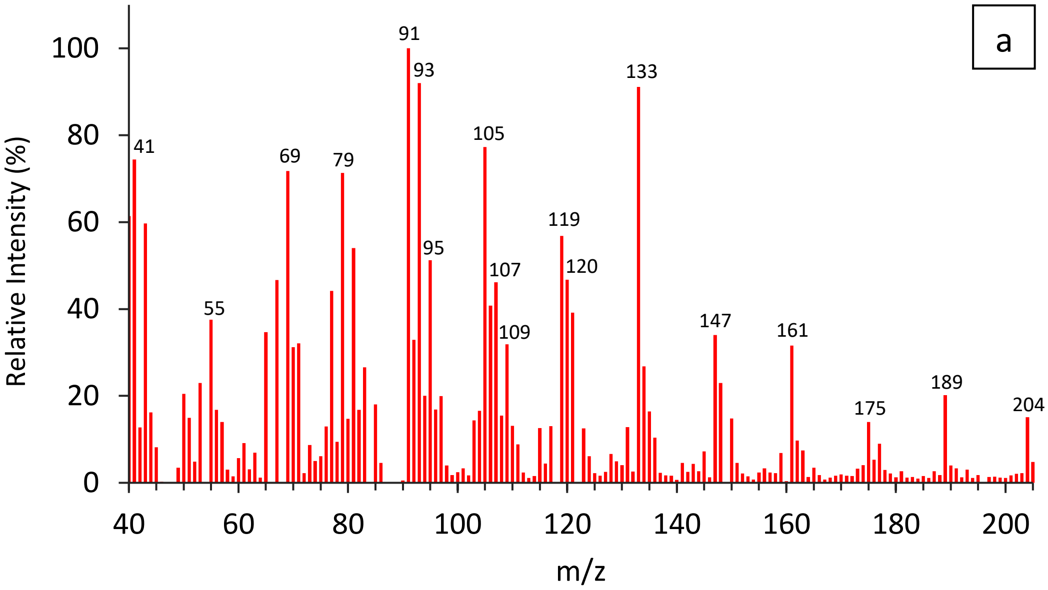

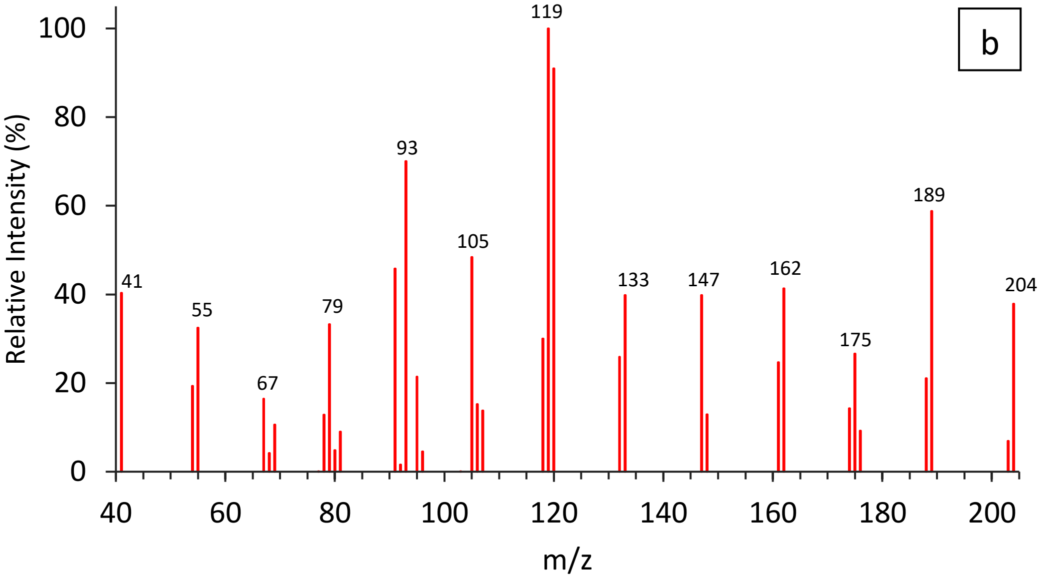

Figure 22: a) GC-MS electron ionization mass spectra of ϐ-caryophyllene internal standard (4.3 min retention time). b) Denoised GC-MS electron ionization mass spectra (selected ions ± 2 m/z: 41, 55, 67, 79, 93, 105, 119, 113, 147, 162, 175, 189, and 204) of amorphadiene synthesized from FPP using ADS (8.1 min retention time).

As shown in Figure 22, the mass spectra of the internal β-caryophyllene standard and synthesized amorphadiene from FPP (tested in duplicate) match well with the expected mass spectra given by the National Institute of Standards and Technology database and literature references respectively with characteristic peaks for quantification at 189 and 204 m/z (Ward et al., 2019; Baadhe et al., 2013). Although best practices baking out the GC-MS and calibrating the system were performed regularly to minimize bleed through and contaminants within the column, several low molecular weight ions caused by the solvent ethyl acetate, air/water (to a lesser degree), and pump oil vapour contaminants, among those potentially less identifiable were observed. Although negligible for the β-caryophyllene samples which were high in concentration, the amorphadiene samples had very low concentrations ranging from approximately 2.0-5.0 mg/L and were consequently near the common lower limits of detection for GC-MS (Underwood et al., 1997). Since the chromatogram peak for amorphadiene was masked by significant noise, the chromatogram was first selectively scanned for the characteristic mass spectra peaks of amorphadiene at 189 and 204 m/z to determine its average retention time of 8.1 min. The mass spectra given in Figure 22b was then produced by selectively screening for the fragment's characteristic to amorphadiene and filtering out noise and contaminants. Having successfully identified the correct synthesis of amorphadiene and an expected retention time of

8.1 min for the given operating conditions producing amorphadiene from FPP, a basis for the identification of amorphadiene using peaks at 189 and 204 m/z was confirmed. This method of detection was subsequently extended to more complex systems such as free/immobilized cascade reactions for the detection of amorphadiene where undesirable pathway by-products have the potential to further increase chromatogram noise.

5.9. Cascade IUP Reaction in Solution

Having determined the individual Michaelis-Menten parameters given in Table 7 and generated a standard amorphadiene GC-MS chromatogram, an *in vitro* cascade batch enzymatic reaction was simulated in COMSOL Multiphysics and tested experimentally to confirm the synthesis of amorphadiene from isoprenol. The cascade reaction was incubated in 1.0 M Tris-HCl (pH 7.5) buffer, 10 mM $MgCl_2$, 10 mM ATP, and 5 mM ISP with enzyme concentrations of 3.0 µM CK, 1.8 µM IPK, 2.0 µM IDI, 2.0 µM IspA, and 1.0 µM ADS at 37 °C with 250 RPM of shaking. The amorphadiene produced was captured using C-18 resin and analyzed by GC-MS as previously described.

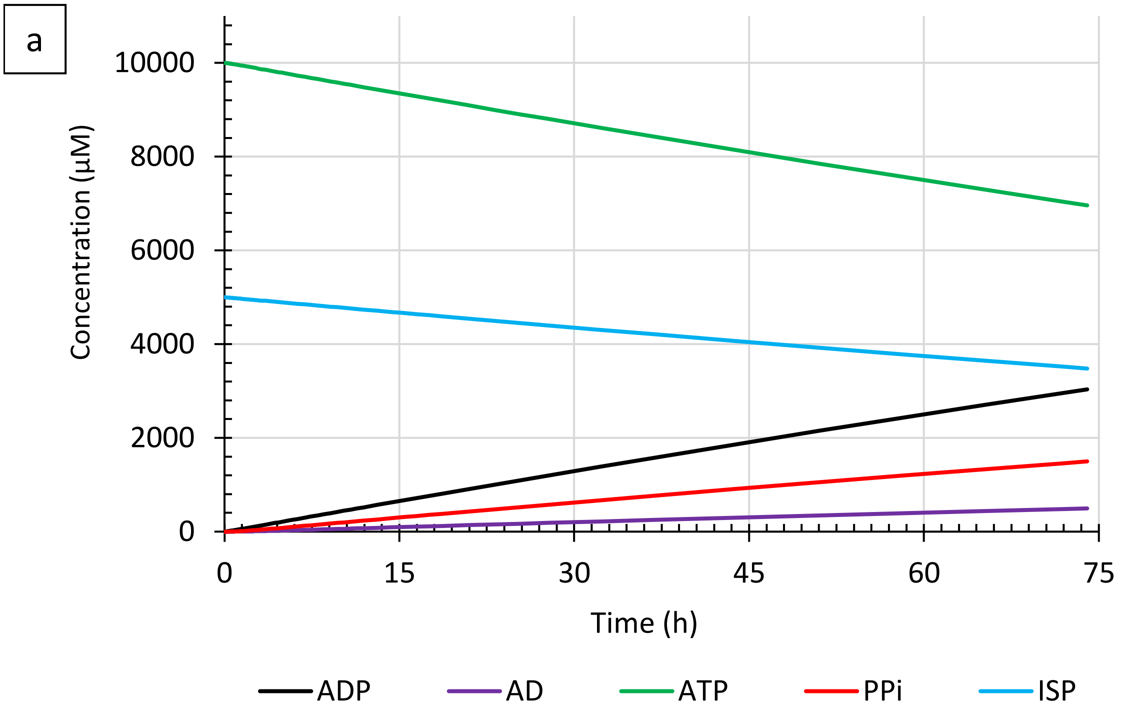

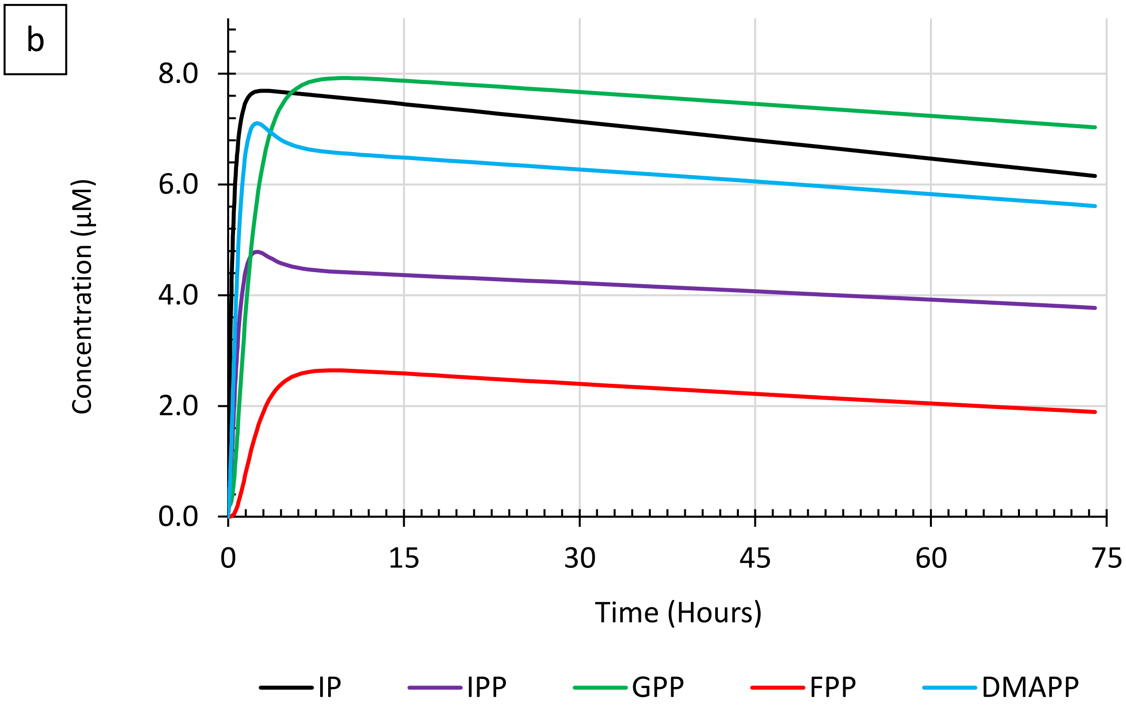

Figure 23: Predicted time-course concentration profiles of a) substrates and products, and b) intermediate metabolites for the cascade IUP reaction modelled by Equation 13 andEquation 14 at a temperature of 37 °C and pH of 7.5. The initial concentrations at the beginning of the reaction were 5 mM ISP, 10 mM ATP, 3.0 µM CK, 1.8 µM IPK, 2.0 µM IDI, 2.0 µM IspA, and 1.0 µM ADS.

As shown in Figure 23a, the predicted concentration of amorphadiene after 74 h was 496 µM corresponding to a productivity of 6.70 µM/h. The concentration of the IUP enzymes were selected to minimize the accumulation of intermediate metabolites such as IP, IPP, DMAPP, GPP, and FPP. As shown in Figure 23b, all of the intermediate metabolites were below 10 µM at low concentrations relative to the products modelled in Figure 23a. Although the concentration of amorphadiene could not be quantified directly without a commercially available standard, the synthesis of amorphadiene from isoprenol was confirmed by GC-MS and determined to have an average final concentration of 0.085 ± 0.006 mg/L β-caryophyllene equivalent. This proof-of-concept corroborates the correct activity and mechanism of the IUP enzymes and supports that the coupled ADP/PPi enzyme assays were efficient for monitoring enzyme activity without the natural oxidation of NADH to NAD$^+$ skewing spectrophotometric detection and providing false observations of ADP/PPi consumption. If the kinetic assays were incorrectly characterized due to the natural oxidation of NADH rather than the consumption of ADP/PPi due to enzyme catalysis, then the formation of amorphadiene would not be observed since one or more enzymatic steps in the IUP pathway would be defunct. Additionally, the synthesis of amorphadiene corroborates the unquantified activity of IDI to be correct since the formation of DMAPP catalyzed by IDI is necessary as an intermediate step before the formation of GPP, FPP, and amorphadiene are possible.

The productivity of cascade IUP amorphadiene synthesis in this study was low at 0.00115 ± 0.00008 mg/L·h compared to other *in vitro* IUP amorphadiene synthesis systems which had an average productivity of approximately 0.00713 mg/L·h after incubation at 30 °C with an enantiomerically pure isoprenol feed and enzyme concentrations of 50 µg/mL CK, IPK, IDI, IspA, and ADS (Ward et al., 2019). As shown in Table 3 the absolute productivity of *in vivo* amorphadiene synthesis is typically much higher than that reported in this study for cell-free synthesis with values reaching up to 390 mg/L·h for a highly engineered strain of *S. cerevisiae* utilizing the MVA pathway (Westfall et al., 2012). For comparison with *in vivo* amorphadiene synthesis systems, only the absolute amorphadiene productivity can be compared since normalizing the amorphadiene productivity depends on the DCW which is not applicable for cell-free synthesis systems utilizing *in vitro* enzyme activity. Consequently, the absolute amorphadiene productivity for *in vitro* batch synthesis is highly dependant on the concentration of enzymes loaded and should therefore be compared with similar cell-free studies.

Evaluating the specific productivity of *in vitro* amorphadiene synthesis based on the enzyme loading of CK, IPK, IDI, IspA, and ADS, the results of this study having a specific productivity of 0.00254 ± 0.00018 µg β-caryophyllene eq./mg·h were lower than those reported in the literature at a value of approximately 0.0285 µg β-caryophyllene eq./mg·h (Ward et al., 2019). The lower specific amorphadiene productivities reported in this study were likely due to the kinetics of IDI which were not characterized experimentally and may have had a lower turnover rate or higher substrate binding affinity values than those assumed in Table 5 which would have negatively affected the formation of DMAPP and the subsequent downstream enzymatic steps producing amorphadiene. Although the effect of IDI on the pathway flux and specific productivity of amorphadiene can be investigated and optimized by varying the concentration of IDI and monitoring amorphadiene synthesis, such an experiment was not performed in this study. The reason for this was that the cascade enzymatic synthesis of amorphadiene free in solution was performed to ensure correct pathway activity and amorphadiene formation before developing a sequentially immobilized cascade enzymatic microfluidic reactor which would be highly labour intensive and impractical for investigating and optimizing the effects of IDI. Despite having low absolute and specific amorphadiene productivities, the successful cascade enzymatic synthesis of amorphadiene free in solution confirmed the correct pathway activity which was beneficial towards increasing the complexity of the system for the development of sequentially immobilized cascade systems.

5.10. COMSOL Multiphysics Modelling of Sequentially Immobilized IUP Microfluidic Reactor

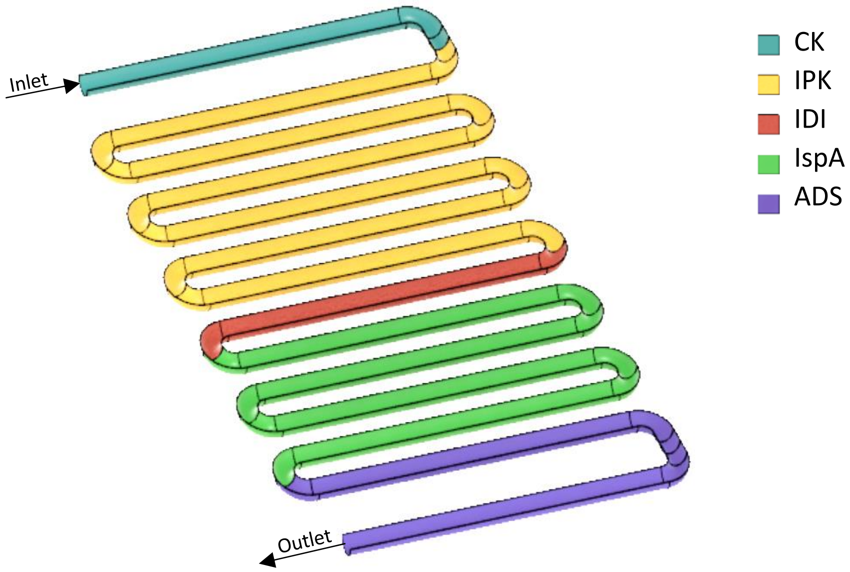

Figure 24: Spatial distribution of the sequentially immobilized IUP microfluidic reactor (see Figure 17 for reactor configuration).

Based on the results of the free enzyme IUP batch reaction which successfully produced amorphadiene and confirmed the correct activity of the pathway, a sequentially immobilized cascade IUP microfluidic reactor was designed, simulated in COMSOL Multiphysics, and tested experimentally. The enzyme spatial distribution and concentration profile results of the COMSOL Multiphysics simulation are shown in Figures 24 and 25 (see next page), respectively. The reactor configuration selected was the same as that used in the ALP study shown in Figure 17 having a diameter of 1.5 mm, length of 388 mm, and surface to volume ratio of 2666 m^2/m^3. To optimize the efficiency of amorphadiene synthesis, the enzyme concentrations should ideally be selected such that the concentration of the intermediate metabolites are above their respective substrate binding affinity values for the enzyme catalyzing each sequential enzymatic step. This consideration ensures that the rate of reaction for each enzymatic step is near the maximum velocity for the duration of each immobilized enzyme compartment. The second consideration for selecting optimal enzyme concentrations is to minimize the accumulation of intermediate metabolites. This is simple when considering CK, IPK, IspA, and ADS which catalyze enzymatic steps where maximum substrate consumption is ideal and so pathway flux is increased as the enzyme concentrations are increased.

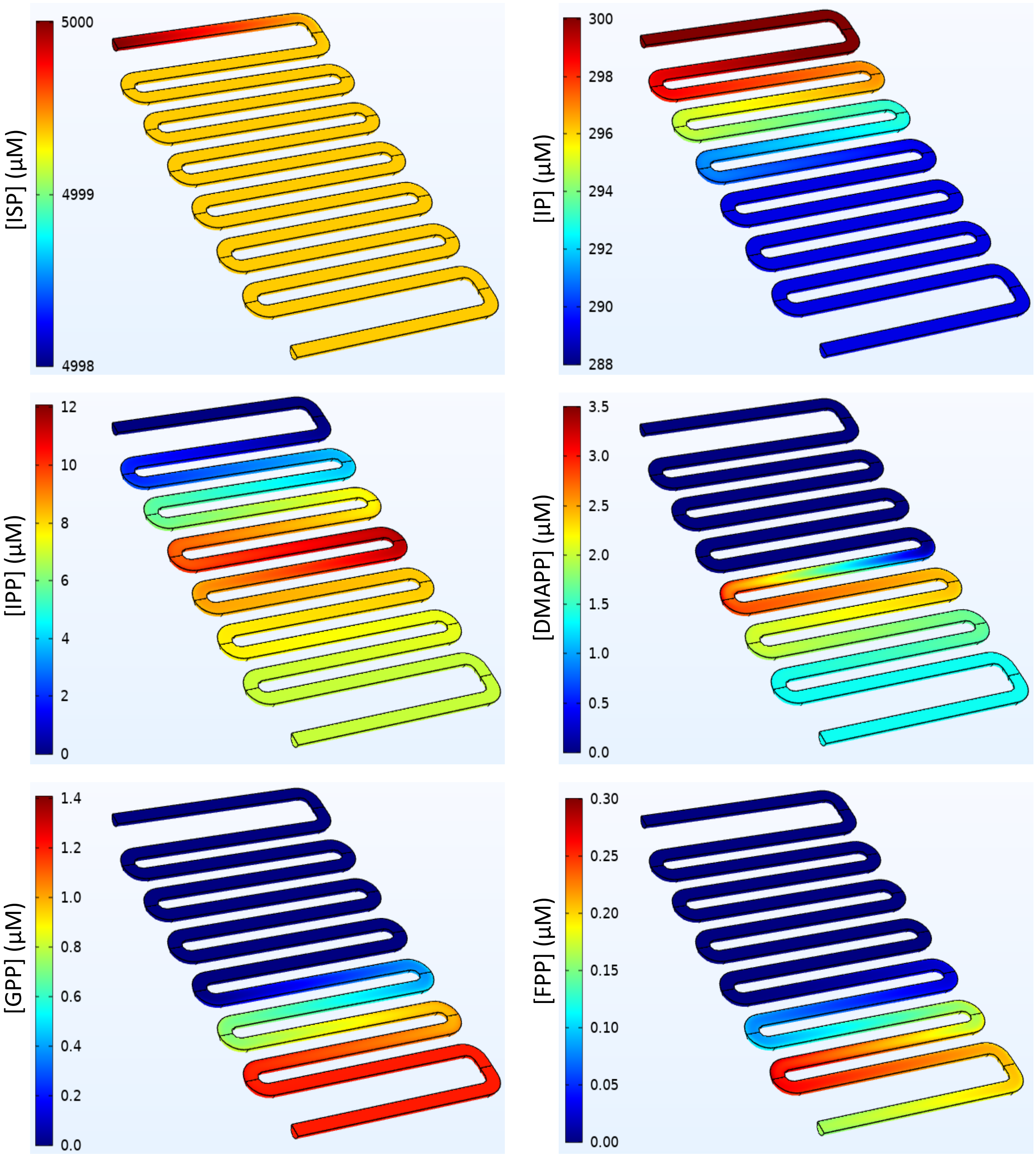
[ISP] (μM)
5000
4999
4998
[IP] (μM)
300
298
296
294
292
290
288
[IPP] (μM)
12
10
8
6
4
2
0
[DMAPP] (μM)
3.5
3.0
2.5
2.0
1.5
1.0
0.5
0.0
[GPP] (μM)
1.4
1.2
1.0
0.8
0.6
0.4
0.2
0.0
[FPP] (μM)
0.30
0.25
0.20
0.15
0.10
0.05
0.00

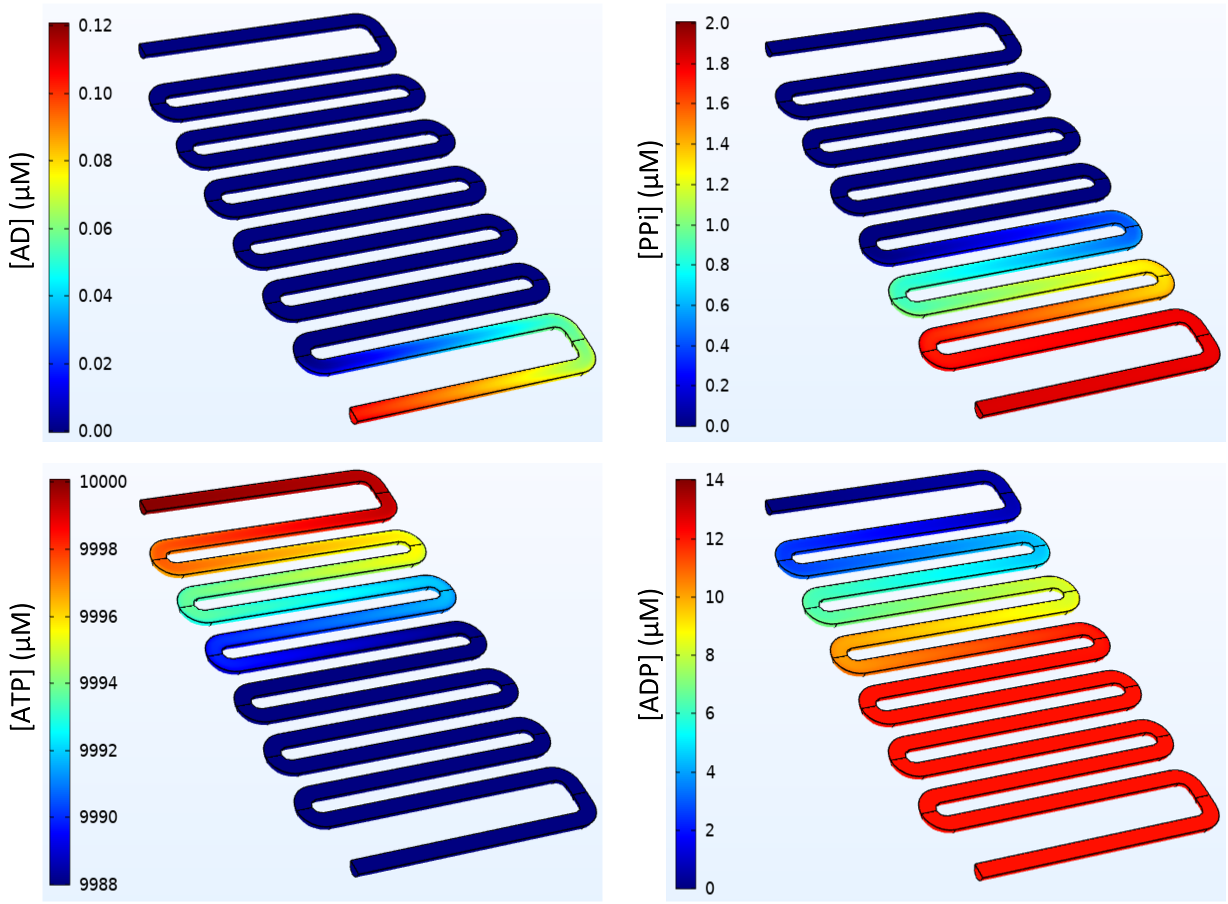

Figure 25: Concentration profiles of substrates, products, and intermediate metabolites modelled in COMSOL Multiphysics as a sequentially immobilized IUP enzymatic microfluidic reactor (see Figure 17 andFigure 24 for reactor details). The sequentially immobilized enzyme concentrations and percent relative spatial distribution were as follows: 0.490 µM CK (6.8 %), 0.238 µM IPK (43.1 %), 0.099 µM IDI (7.2 %), 0.540 µM IspA (28.6 %), and 0.333 µM ADS (14.3 %). The selected flow rate was 79.2 µL/h corresponding to a total residence time of 8 h (32.6 min for CK, 206.9 min for IPK, 34.6 min for IDI, 137.3 min for IspA, and 68.6 min for ADS). The concentrations of the inlet feed stream were 5000 µM ISP, 10000 µM ATP, and 300 µM IP which resulted in an average modelled outlet amorphadiene concentration of 0.104 µM.

More practical for experimentation than maximizing the enzyme concentrations of CK, IPK, IspA, and ADS, the enzyme concentrations should be selected based on acceptable residual intermediate metabolite concentrations since the specific amorphadiene productivity based on the amount of enzyme immobilized would become inefficient at high enzyme concentrations (with the exception of CK which is rate-limiting for the downstream enzymes given an enantiomerically pure feed). For IDI it has been shown that a 3:1 ratio of ISP to prenol (equivalent to the IPP to DMAPP ratio when IDI is used with an enantiomerically pure isoprenol feed) was optimal for cell free isoprenoid synthesis (Ward et al., 2019). This ratio was used as the basis for selecting the concentration of immobilized IDI and was found to be optimal since simulations varying the concentration of IDI (and thus the IPP to DMAPP ratio) resulted in lower pathway flux or significant IPP/DMAPP accumulation (data not shown).

Although a rational for selecting optimal enzyme concentrations based on limiting intermediate metabolites to a specified threshold concentration for CK, IPK, IspA, and ADS, and maintaining a 3:1 ratio of IPP to DMAPP for the selected concentration of IDI have been put forth, maintaining the intermediate metabolite flux above or near the substrate binding affinity of each enzyme proved experimentally impractical. The reason for this was due to the B9Creator 3D-printer used which required a large resin reservoir for printing. Consequently, the purified enzyme stocks were diluted a minimum of 20-100 times once added to the 3D-printing resin. A variety of solutions to this issue are possible and several were implemented to increase the immobilized enzyme concentrations as will be further discussed with respect to the B9Creator 3D-printer used.

The first and most evident solution to offset the effects of significant enzyme dilution was to simply add more enzyme to the 3D-printing resin. Although a very viable solution and one which was partially implemented by loading as much of the purified enzymes as possible into the 3D-printing resin, scaling the production and purification of enzymes to the levels required to maintain relatively high intermediate metabolite concentrations throughout the microfluidic reactor would be labour intensive at laboratory scale and better suited for continuous cultivation and purification which was outside the scope of this project. A minor solution which was implemented to reduce the dilutionary effect was to 3D-print a vat modification which provided void space and reduced the amount of resin required to fill the reservoir for printing by approximately 2-fold (this was applicable since the printing volume was small with only 10 % of the resin being polymerized and the other 90 % remaining in the reservoir after printing). The last solution which was implemented out of necessity due to the relatively low yields and activity of CK was to include IP in the feed stream at a concentration of 300 µM. All else being equal except for the addition of IP, the average concentration of IPP entering the immobilized IDI compartment was only 0.27 µM (COMSOL Multiphysics model not shown) compared to over a 42-fold increase to 11.42 µM as shown in Figure 25 when supplementing IP at concentrations above the substrate binding affinity value of 21.5 µM to increase the enzymatic activity of IPK. Without the supplementation of IP in the feed stream, the downstream IDI, IspA, and ADS enzymatic compartments were very inefficient and produced an insignificant amount of amorphadiene due to the compounding effects of sequentially lower enzyme activity in each enzymatic compartment due to decreasing concentrations of each intermediate metabolite. While this observation still remains in Figure 25 with the modelled concentration of amorphadiene at the reactor outlet of 0.104 µM being only 3.7 % of the theoretical maximum yield based on the limiting concentration of DMAPP leaving the IDI compartment at a concentration of 2.83 µM, supplementing IP greatly increased the pathway flux resulting in amorphadiene concentrations more suitable for experimentation and detection by GC-MS. Although supplementation of IP was not optimal, IP was relatively inexpensive to synthesize in this study and was preferable to alternatives such as supplementing GPP/FPP which are expensive or further increasing the residence time of the reactor which would only have a minimal effect on pathway flux since it was already long at a total of 8 h.

Due to a large degree of enzyme dilution for the modelled sequentially immobilized cascade IUP microfluidic reactor shown in Figure 25, the selection of enzyme concentrations became constrained making an optimal design under the aforementioned considerations for maximum pathway flux unattainable. Instead, the design presented in Figure 25 is better depicted as a proof-of-concept for the immobilized cascade enzymatic production of amorphadiene since the predicted concentrations of the intermediate metabolites at the reactor outlet are at consequently high concentrations of 6.90 µM IPP, 1.36 µM DMAPP, 1.20 µM GPP, and 0.16 µM FPP relative to amorphadiene at only 0.104 µM making the cascade reaction highly inefficient. The supplementation of IP at a concentration of 300 µM in the reactor feed prevented CK from being rate-limiting and instead IPK was rate-limiting for further downstream enzymes and so was given the largest spatial distribution within the microfluidic reactor at 43.1 % of the total reactor surface area. Without any experimental or literature data available to estimate the normalized immobilization efficiency of IDI at a SA:V ratio of 2666 m^2/m^3, an average value of 0.186 was assumed based on the normalized immobilization efficiencies of CK, IPK, IspA, and ADS at a SA:V ratio of 2666 m^2/m^3. Based on this assumption and an allotted spatial distribution of 7.2 % of the total reactor surface area, the average modelled concentrations of IPP and DMAPP leaving the IDI enzymatic compartment were 8.62 µM and 2.83 µM respectively resulting in a modelled IPP to DMAPP ratio of 3.04. In the immobilized IspA compartment, the activity of IspA was highly selective towards the synthesis of GPP which had a much higher modelled concentration of 1.20 µM compared to FPP at only 0.27 µM. As summarized in Table 7, the binding affinity of GPP for the synthesis of FPP by IspA was 8.63 µM which was much higher than even the maximum local GPP concentrations modelled which only reached 1.24 µM. This significantly restricted the rate of FPP synthesis due to low GPP concentrations throughout the IspA compartment. The modelled concentrations of IPP and DMAPP leaving the IspA compartment remained relatively high at an average concentration of 6.90 µM and 1.36 µM respectively which also indicate the inefficiency of the IspA compartment with respect to DMAPP consumption. Although the modelled concentration of DMAPP throughout the IspA enzyme compartment was above the substrate binding affinity value summarized in Table 7 of 1.19 µM for GPP synthesis from IPP and DMAPP which promoted reasonable rates of reaction, the substrate binding affinity of IPP towards FPP synthesis was much lower than for GPP synthesis at 5.65 µM and 20.6 µM respectively which had the undesirable effect for IPP to be consumed towards FPP synthesis faster than GPP was produced. For the optimal case where the concentration of IPP is much higher than the substrate binding affinity for both GPP and FPP synthesis, the rate of reaction for GPP and FPP synthesis are near their respective maximum velocities and the selectivity of IPP towards FPP synthesis becomes advantageous since GPP produced is consumed at a faster rate and therefore does not accumulate (the turnover rate for GPP and FPP synthesis are similar as shown in Table 7). Since the modelled concentration of IPP was relatively low with respect to its substrate binding affinity values for FPP and GPP synthesis, the concentration of GPP remained below the substrate binding affinity required for reasonable rates of FPP synthesis and the IspA compartment was a significant bottleneck with only 9.5 % FPP yields based on the average limiting concentration of DMAPP entering the compartment. Similar to the bottleneck created in the IspA compartment, the maximum local concentration of FPP modelled in the ADS compartment only reached a maximum local concentration of 0.29 µM which was significantly below the substrate binding affinity of 1.91 µM summarized in Table 7. Consequently, the modelled rate of amorphadiene synthesis was relatively low with only 39.2 % of the incoming FPP being converted to amorphadiene despite a 14.3 % ADS spatial distribution within the reactor. Although the yield of amorphadiene in the ADS compartment was relatively low, it was much higher than the IspA bottleneck which only had a FPP yield of 9.5 % despite having double the reactor spatial distribution for ADS at 28.6 %. Overall, the compounding effect of low yields in the IspA and ADS compartments resulted in a modelled amorphadiene yield of only 3.7 % with respect to the limiting-concentration of DMAPP leaving the IDI compartment which resulted in a modelled outlet concentration of only 0.104 µM amorphadiene. Despite the effects of compounding bottlenecks in the sequentially immobilized reactor due to experimental limitations causing significant enzyme dilution restricting reactor design and enzyme activity throughout the reactor, the proposed model in Figure 25 produced amorphadiene at a rate sufficient for detection by GC-MS and so was deemed suitable for experimentation as a proof-of-concept.

It should also be mentioned that external diffusion was not a limiting factor in the design proposed in Figure 25 with the Peclet number above 1000 for all species throughout the reactor suggesting that convective transport was the prevailing transport mechanism. The only exception was along the reactor walls due to the no-slip boundary condition which consequently had a Peclet number of zero. Under these mass transport conditions, the assumptions made regarding the definition of the immobilization efficiency in Equation 15 and the diffusivity coefficients in Equation 21 were satisfied. The former due to the reactor being kinetically-limited throughout the reactor for all species and the latter based on the quantitative assumption that the difference between the solute molal volume at normal boiling point and the assumed values at atmospheric pressure used in Equation 21 were less than the 10^5-fold increase required to reduce the Peclet number from the lowest values of 1000 modelled in this study to a diffusion-limiting range below one.

5.11. Stability of Sequentially Immobilized IUP Microfluidic Reactor Metabolites

Having designed the model given in Figure 25, the sequentially immobilized cascade IUP microfluidic reactor was 3D-printed using the B9Creator stereolithographic printer by intermittently changing the 3D-printing resin at specific points during the printing process as outlined in Figure 24 to spatially immobilize the enzymes in sequential order. The feed stream to the microfluidic reactor was 5.0 mM ISP, 10 mM ATP, 300 µM IP, 10 mM $MgCl_2$, in 1.0 M Tris-HCl (pH 7.5) buffer at a temperature of 37 °C. Samples from the inlet and outlet streams were collected intermittently during operation to monitor the outlet concentrations of ADP and PPi using the previously described spectrophotometric NADH-coupled assays for comparison with the COMSOL Multiphysics model presented in Figure 25 and to identify when the system reached steady-state.

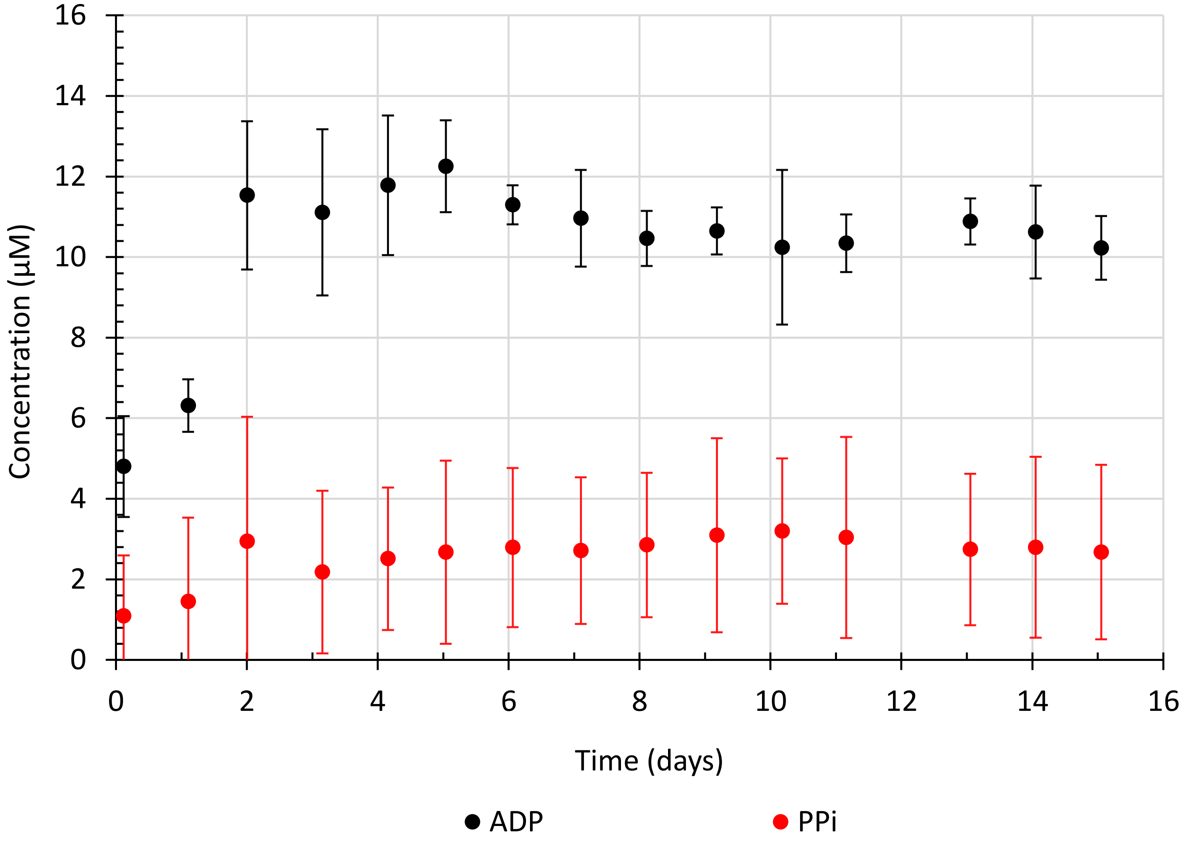

Figure 26: Experimental enzymatic stability of the sequentially immobilized IUP microfluidic reactor by monitoring the outlet concentration of ADP and PPi using coupled enzymatic assays. The feed stream to the reactor was 5.0 mM ISP, 10 mM ATP, 300 µM IP, 10 mM $MgCl_2$, and 1.0 M Tris-HCl (pH 7.5) buffer at a temperature of 37 °C (See Figures 19 and 24 for reactor configuration). Each data point is the average of 4 samples collected throughout the day except for the first PPi data point which only had 2 samples (error bars 1 σ).

The time course concentration profiles of ADP and PPi over the span of 15 days starting from a saturated reactor condition having only buffer solution containing 1.0 M Tris-HCl (pH 7.5) and 10 mM $MgCl_2$ is given in Figure 26. Due to a long residence time of 8 h and the dependency of each sequential enzymatic compartment on those upstream, approximately 6 reactor volumes were required for the concentrations of ADP and PPi to reach steady state by day 2 of continuous operation. Based on the reaction scheme of the IUP, the stability of PPi formation is expected to provide an estimate of the stability for the entire immobilized pathway since PPi is produced downstream in the IspA and ADS compartments. Alternatively, the stability of ADP formation is expected to provide an estimate of the upstream stability of the CK and IPK compartments. As shown in Figure 26, the outlet concentration of PPi had high variability and was at an average initial steady-state concentration after two days of 2.95 ± 3.09 µM. Although this value falls within the range predicted by the COMSOL Multiphysics model in Figure 25 of 1.84 µM at the reactor outlet, the spectrophotometry machine error at low PPi concentrations was estimated to be ± 1.45 µM for each measurement which makes meaningful interpretation of the PPi concentration profile in Figure 26 difficult since the confidence interval is often much larger than the average PPi concentration resulting in considerable amounts of experimental uncertainty. Alternatively, the concentration profile of ADP in Figure 26 was much more consistent with an average initial steady-state concentration of 11.53 ± 1.64 µM after 2 days of continuous operation. Although the experimental uncertainty was still relatively large for many of the ADP concentration measurements, its effect on the interpretation of the ADP concentration profile given in Figure 26 was less significant than for the PPi concentration profile since the measured concentrations of ADP were much higher than PPi such that the spectrophotometry machine error was minimal. Based on these results, the concentration profile of ADP was used for comparison with the COMSOL Multiphysics model in Figure 25 and evaluating the stability of the reactor.

Comparison of the initial and maximum steady-state ADP concentrations of 11.53 ± 1.64 µM and 12.25 ± 1.45 µM after 2 and 5 days of continuous operation respectively demonstrated that the COMSOL Multiphysics model in Figure 25 was efficient at modelling the sequentially immobilized IUP microfluidic reactor in the CK and IPK compartments. The average predicted concentration of ADP at the outlet of the COMSOL Multiphysics model summarized in Figure 25 was 12.1 µM which is only a 1.2-4.9 % difference between the modelled and average experimental steady-state concentration of ADP. The stability of the CK and IPK compartments based on the outlet concentration of ADP were also relatively high with the average flux of ADP decreasing only 11.4-16.6 % after 10-13 days of continuous operation based on the initial and maximum steady state values on days 2 and 5, respectively. The stability of the CK and IPK compartments was also monitored after 41 days of continuous operation (123 cycles) and demonstrated approximately linear time-dependency with the average outlet ADP concentration decreasing to 4.81 ± 1.02 µM corresponding to a 58.3-60.7 % decrease relative to the initial and maximum steady-state ADP concentrations, respectively. The reactor was also tested in the reverse order with the feed stream entering the ADS compartment and the detection of both ADP and PPi leaving the CK compartment were negligible suggesting that the enzymes were spatially distributed without significant multi-compartmental enzyme entrapment.

5.12. Immobilized IUP Microfluidic Reactor Pathway Flux and Amorphadiene Productivity

To estimate the outlet concentration of amorphadiene leaving the sequentially immobilized IUP microfluidic reactor, the amorphadiene in the outlet stream was continuously captured using a stationary C-18 resin loaded into a gravity flow column. Due to the very low predicted concentration of amorphadiene leaving the reactor of 0.104 µM as shown in Figure 25, the amorphadiene from the reactor outlet was collected for 113 h and eluted in 25 µL of 90 mg/L β-caryophyllene resulting in a 358-fold concentration increase sufficient for detection by GC-MS analysis. The amorphadiene from the reactor outlet was collected starting at the end of the third day of continuous operation once steady-state had been reached based on the concentration profile of ADP shown in Figure 26. The resultant productivity and measured concentration of amorphadiene at the reactor outlet were $1.81\text{x}10^{-6} \pm 0.18\text{x}10^{-6}$ mg/L·h β-caryophyllene equivalent and $1.45\text{x}10^{-5} \pm 0.14\text{x}10^{-5}$ mg/L β-caryophyllene equivalent, respectively (the experimental uncertainty was estimated by running the sample in triplicate in lieu of replications). Although this value cannot be compared to the COMSOL Multiphysics model in Figure 25 directly due to the use of β-caryophyllene as an internal standard, it may be compared relatively with the results of the cascade synthesis of amorphadiene free in solution which had a final experimental amorphadiene concentration of 0.085 ± 0.006 mg/L β-caryophyllene equivalent for a predicted amorphadiene concentration of 496 µM as shown in Figure 23a. Based on the average predicted amorphadiene concentration of the sequentially immobilized cascade IUP microfluidic reactor of 0.104 µM as shown in Figure 25, linear interpolation with respect to the results of the cascade IUP free in solution gives a predicted sequentially immobilized microfluidic reactor outlet amorphadiene concentration of $1.78\text{x}10^{-5} \pm 0.13\text{x}10^{-5}$ mg/L β-caryophyllene equivalent. Comparing with the experimentally determined reactor outlet concentration of amorphadiene of $1.45\text{x}10^{-5} \pm 0.14\text{x}10^{-5}$ mg/L β-caryophyllene equivalent, the experimental amorphadiene concentration was on average 22.7 % lower than the predicted concentration based on interpolation of results for the enzymes free in solution. Although a very crude analysis due to the unavailability of amorphadiene standards, and the degree of uncertainty from interpolation of the cascade IUP free in solution experimental results cannot be overstated, the low experimental microfluidic reactor outlet concentration of amorphadiene relative to the predicted value from interpolation suggests that the downstream IDI, IspA, and ADS enzyme compartments had lower pathway flux than predicted by the COMSOL Multiphysics model in Figure 25.

Without overanalyzing uncertain quantitative details based on interpolation of the cascade IUP free in solution results beyond the experimentally determined microfluidic reactor outlet amorphadiene concentration of $1.45\text{x}10^{-5} \pm 0.14\text{x}10^{-5}$ mg/L β-caryophyllene equivalent and the likelihood that the downstream IDI, IspA, and ADS enzyme compartments had lower pathway flux than predicted by the COMSOL Multiphysics model, several potential contributing reasons for reduced amorphadiene flux will be discussed. The first contributing reason for potentially lower amorphadiene flux than predicted in Figure 25 was due to losses and the efficiency of amorphadiene binding and elution during preparation for GC-MS. Although inevitably present, the efficiency of amorphadiene binding was expected to be high based on the C-18 resin selected and the amorphadiene was eluted from the resin several times to maximize the recovery yield and so the overall amorphadiene losses during recovery were expected to be minimal. Another potential reason for reduced amorphadiene flux was due to enzyme deactivation and/or leakage which caused the pathway flux to decrease over time as observed by the reducing ADP flux at the reactor outlet in Figure 26. Although not significant over a short period of time, the amorphadiene sample analyzed by GC-MS was collected over the span of 113 h from days 3 to 8 of continuous operation which had a significant reduction in ADP flux as shown in Figure 26 corresponding to reduced enzymatic activity in the CK and IPK compartments. Since the immobilization procedure of all the enzymes in the IUP were identical, it is expected that the rate of enzyme deactivation and/or leakage would be similar among all the sequentially immobilized enzyme compartments. The rate of amorphadiene production is therefore expected to decrease further than that attributable to the CK and IPK compartments predicted by monitoring the concentration of ADP in Figure 26 due to the compounding effect of reduced activity on each sequential enzyme compartment including IDI, IspA, and ADS which were not accounted for due to the inconclusive and unreliable monitoring of PPi observed in Figure 26. Lastly the COMSOL Multiphysics model in Figure 25 assumed the kinetics of IDI based on literature kinetic parameter values and an average immobilization efficiency based on the immobilized kinetic assays of CK, IPK, IspA, and ADS in this study. Consequently, the experimental and modelled kinetics of IDI are likely to differ based on factors such as enzyme purity and activity which would affect the experimental downstream pathway flux based on the experimental ratio of IPP to DMAPP which may not have been optimal at a ratio of 3.04 as modelled.

6. Conclusion

The recent developments in the field of additive manufacturing technologies for high resolution 3D-printing has gained researcher attention as the new standard for high complexity, low cost, microfluidic reactor fabrication. The development of cascade immobilized enzymatic reactors is of particular interest as an alternative to traditional *in vivo* systems since the requirement for extensive metabolic engineering to enhance pathway productivity to commercially viable levels and reduce metabolic regulation limitations is avoided. Enzyme immobilization also offers several advantages over cell-free systems such as increased stability, easy product recovery, and the ability to operate continuously. Immobilized cascade enzyme reactors are also very versatile and have been used for a variety of applications such as *in vitro* synthesis, cofactor regeneration, and product detection. In this study the application of additive manufacturing was used to simultaneously entrap enzymes during 3D-printing for the fabrication of sequentially immobilized microfluidic reactors for *in vitro* synthesis of amorphadiene via the IUP.

As an initial proof-of-concept to investigate the feasibility of simultaneously entrapping enzymes during 3D-printing in a PMMA matrix using the B9Creator stereolithographic 3D-printer, ALP was selected as a model enzyme for kinetic characterization, COMSOL Multiphysics microfluidic reactor modelling, and immobilized microfluidic reactor experimentation to monitor enzyme stability. Using 3D-printed wells to perform ALP activity assays, no significant shift in the average substrate binding affinity of ALP during immobilization was observed relative to the free enzyme assays having average values of 1.57 ± 0.02 µM and 1.59 ± 0.01 µM, respectively. The immobilization efficiency was also investigated by varying the enzyme concentration and SA:V ratio of the immobilized enzyme assays. As expected for entrapped enzymes, the immobilization efficiency increased linearly with the enzyme concentration and SA:V ratio respectively and had low activity with the immobilization efficiency ranging from 0.01 ± 0.001-0.057 ± 0.002 (0.028 ± 0.003-0.057 ± 0.002 for the specific immobilization efficiency at a SA:V ratio of 2666 m^2/m^3) due to significant internal diffusion limitations. Based on these results, a high SA:V ratio immobilized ALP microfluidic reactor having negligible external diffusion limitations was designed, modelled in COMSOL Multiphysics, and tested experimentally to compare steady-state operation with the predicted COMSOL Multiphysics model and to experimentally determine the stability of ALP after extended operation and storage. Comparison of the reactor outlet concentration of NP at steady-state with the COMSOL Multiphysics model demonstrated the applicability of COMSOL Multiphysics as an effective steady-state modelling tool for immobilized enzyme microfluidic reactor simulations with only a 3.9 % difference between the observed and modelled outlet concentration of NP. Monitoring of the mean ALP activity over the span of 16 days of continuous operation followed by an additional 82 days of storage demonstrated high enzyme stability with the immobilized ALP retaining 85.4-92.3 % and 54.2 % of its initial mean enzymatic activity during continuous operation and storage, respectively. Assuming the lifespan of an immobilized microfluidic reactor to be its activity half-life, the immobilized ALP reactors had a lifespan of 55-104 days (equivalent to 660 reactor cycles) during continuous operation and 91 days during storage which was similar to other entrapped enzyme systems reported in the literature (Xu et al., 2006; Heo & Crooks, 2005).

Based on the effective use of COMSOL Multiphysics for modelling and the high stability of the entrapped ALP microfluidic reactor, the enzymes required for the synthesis of amorphadiene via the IUP were synthesized and purified for the development of a sequentially immobilized microfluidic reactor. To confirm the activity of each enzyme and ensure accurate kinetic modelling in COMSOL Multiphysics, the purified enzymes were kinetically characterized using ADP- and PPi-coupled assays. As shown in Table 7, the substrate binding affinity values and turnover rates were similar to those reported in the literature. Similar to the free enzyme assays, the immobilization efficiency of each enzyme was characterized using coupled enzyme assays and are summarized in Table 8 with the immobilization efficiencies ranging from 0.066 ± 0.005-0.096 ± 0.010 (0.135-0.249 when the average values are normalized to a SA:V ratio of 2666 m^2/m^3) which were similar to other values reported in the literature for entrapped ADH, BFD, and β-gal in PEG-DA (Schmieg et al., 2019).

Having fully characterized the free and immobilized kinetics of CK, IPK, IspA, and ADS, the cascade reaction of isoprenol to amorphadiene via the IUP was tested by first modelling the batch reaction kinetics in COMSOL Multiphysics and then experimentally testing the cascade reaction free in solution. The correct activity of all the IUP enzymes including IDI were confirmed by the GC-MS detection of amorphadiene which had an average concentration of 0.085 ± 0.006 mg/L β-caryophyllene equivalent corresponding to a batch synthesis productivity of 0.00115 ± 0.0008 mg/L·h. Congruent with the development of a COMSOL Multiphysics model, performing surface response optimization varying the concentration of IDI was deemed outside the scope of this study, and instead the activity of IDI was estimated using kinetic parameters available in the literature. In addition to the low activity of the rate limiting enzyme CK, the assumed activity of IDI could have had an adverse affect on the downstream synthesis of GPP, FPP, and amorphadiene if the IPP to DMAPP ratio was not optimally balanced. These reasons both explain the relatively low specific yields of 0.00115 ± 0.00008 mg/L·h for the cascade free enzyme system investigated in this study relative to similar *in vitro* synthesis of amorphadiene results in the literature having a specific productivity of approximately 0.00254 ± 0.0018 mg/L·h (Ward et al., 2019).

Despite having low productivity, the cascade free enzyme synthesis of amorphadiene via the IUP was successful and a sequentially immobilized cascade IUP COMSOL Multiphysics model producing a sufficient concentration of amorphadiene for experimental detection was developed by adjusting the concentration and spatial distribution of each enzyme. Although the use of stereolithography showed promising results for the kinetic analysis of the individual IUP enzymes with the average normalized immobilization efficiency ranging from 0.135-0.249 for a SA:V ratio of 2666 m^2/m^3, the application of stereolithography for the development of a sequentially immobilized microfluidic reactor proved to be highly limited. The requirement for extensive enzyme dilution on the scale of 20-100 times to fill the resin reservoir for 3D-printing resulted in very low enzyme concentrations in each compartment which consequently caused several low reaction rates incapable of producing metabolites at or near the respective substrate binding efficiency values required for reasonable pathway flux. As such the optimal selection of enzyme concentrations to balance the rates within each enzymatic compartment was foregone in pursuit of a design capable of producing amorphadiene as a proof-of-concept. Due to the low activity of CK, supplementation of IP in the reactor feed was employed to shift the rate-limiting step from CK to IPK and artificially increase pathway flux leaving the CK compartment. The enzyme concentration of each compartment was also maximized using the prepared enzyme stock solutions in their entirety to increase the rate of reaction and produce intermediate metabolites at increased, albeit still undesirable, concentrations. The modelled immobilized cascade IUP microfluidic reactor was highly inefficient having a predicted amorphadiene yield of only 3.7 % based on the flux of DMAPP leaving the IDI compartment which experimentally resulted in a very low amorphadiene productivity of $1.81 \times 10^{-6} \pm 0.18 \times 10^{-6}$ mg/L·h β-caryophyllene equivalent. Due to high experimental error measuring the low concentrations of PPi leaving the reactor, the stability of the IDI, IspA, and ADS compartments could not be measured with meaningful quantitative certainty. However, the CK and IPK compartments demonstrated moderate stability decreasing only 11.4-16.6 % after 10-13 days of continuous operation and still had detectable activity after 41 days of continuous operation (123 cycles) with the average concentration of ADP leaving the CK and IPK compartments decreasing by a total of 58.7-60.7 %. Additionally, the sequentially immobilized COMSOL Multiphysics was able to predict the experimentally determined, steady-state, concentration of ADP with only a 1.2-4.9 % relative error.

In this project, the use of additive manufacturing was applied for the kinetic characterization and development of a sequentially entrapped enzymatic microfluidic reactor for the synthesis of amorphadiene via the IUP. This study demonstrated the applicability of entrapment and particularly 3D-printing as a simple and cheap immobilization procedure omitting both enzyme and support specific optimization making it ideal for complex cascade systems and enzyme spatial distribution. It is the first study to take a quantitative kinetic approach towards direct enzyme entrapment during 3D-printing and expands the current field of cascade immobilized enzyme systems beyond the traditional 2-3 covalently immobilized systems typically studied. The kinetic characterization of both ALP and the IUP enzymes demonstrated relatively high immobilization efficiencies consistent with other entrapped enzyme literature sources (Schmieg et al., 2019) and displayed excellent enzyme stability. Although the amorphadiene productivities reported in this study were inconsequential relative to the studies given in Table 3, and the current outlook of stereolithographic enzyme entrapment is unfavourable based on the current technologies available, this study has identified several benefits of coupling additive manufacturing with cascade enzyme entrapment and the future outlook will be highly dependant on technological or application-dependant developments reducing the requirement for significant enzyme dilution in the field of stereolithographic enzyme entrapment.

7. Recommendations

For a more thorough quantitative analysis and comparison of the COMSOL Multiphysics model developed in this study with experimental results, particularly for the enzyme compartments downstream of IPK, it is desirable to test the synthesis of other isoprenoids that are commercially available such that a standard curve for GC-MS (or other suitable detection methods) can be generated. Quantification of additional isoprenoid products was not performed in this study due to the fundamental enzyme dilutionary limitations during 3D-printing which severely constrained the design of the sequentially immobilized IUP enzymatic microfluidic reactor for the synthesis of amorphadiene. Since thermal bonding 3D-printing methods are unsuitable for enzyme immobilization due to high temperatures causing enzyme degradation, a suitable 3D-printer for overcoming significant enzyme dilution would still rely on photoinitiated polymerization. Two solutions which would reduce the effects of enzyme dilution making 3D-printed enzyme entrapment more suitable would be to design a more efficient reservoir system or a 3D-printer capable of selectively dIspEnsing the resin similar to material extrusion methods with the exception that the resin is simultaneously polymerized by photoinitiation instead of thermal bonding. While the former 3D-printer adaptation may be practical to design for enzyme specific applications, the latter has not yet been developed. The most sophisticated stereolithographic 3D-printers such as the Stratasys V650 Flex utilize a similar design to the B9Creator having a large resin reservoir and full layer-by-layer polymerization (as opposed to selective layer-by-layer polymerization).

Although the results of the sequentially immobilized IUP microfluidic reactor were promising having relatively high immobilization efficiencies, good enzymatic stability, and a versatile, simplistic immobilization procedure, the outlook of using 3D-printing for enzyme entrapment remains highly dependant on technological developments in the field of stereolithographic 3D-printers or using material engineering to create application-specific printing resins. While studying enzymatic pathways having higher flux than the IUP or using much higher enzyme concentrations are recommendations likely to enhance control of pathway flux by ensuring favourable/saturable reaction kinetics, the primary limitation of stereolithographic sequential enzyme entrapment is internal diffusion. A recommendation not investigated in this study due to the requirement for surface-response experimentation is to co-immobilize enzymes to reduce the limitations of internal diffusion by enabling substrate channeling. In addition to co-immobilization, the selection or material engineering of polymers more suitable for stereolithographic enzyme entrapment is recommended to increase the porosity, permeability, and polarity of the monomer solution. Particularly of interest, increasing the porosity of the stereolithographic polymer or similarly using hydrogels is recommended to enhance internal diffusion by allowing increased access to the entrapped enzyme active sites. Similarly, washing/rinsing of the monomer solution from the surface of the entrapped enzyme PMMA-matrix using buffer solution proved difficult which suggests residual monomer was present in the internal microenvironments of the polymer. To facilitate increased washing and removal of residual monomer solution, it is recommended to use a polar stereolithographic polymer such that buffer solutions are suitable for washing. Although the mentioned recommendations may lead to minor improvements regarding simultaneous enzyme entrapment during 3D-printing, without foremost improving the requirement for significant enzyme dilution, the current technology in the field of additive manufacturing favours the research and development of affinity binding immobilization procedures for cascade systems.

References

Ajikumar, P. K., Xiao, W.-H., Tyo, K. E. J., Wang, Y., Simeon, F., Leonard, E., Mucha, O., Phon, T. H., Pfeifer, B., & Stephanopoulos, G. (2010). Isoprenoid Pathway Optimization for Taxol Precursor Overproduction in Escherichia coli. *Science*, *330*(6000), 70–74. https://doi.org/10.1126/science.1191652

Alper, H., Miyaoku, K., & Stephanopoulos, G. (2005). Construction of lycopene-overproducing E. coli strains by combining systematic and combinatorial gene knockout targets. *Nature Biotechnology*, *23*(5), 612–616. https://doi.org/10.1038/nbt1083

Baadhe, R., Mekala, N., Parcha, S., & Devi, Y. (2013). Combination of ERG9 repression and enzyme fusion technology for improved production of amorphadiene in saccharomyces cerevisiae. *Journal of Analytical Methods in Chemistry*, *2013*(140469), 1–8. https://doi.org/10.1155/2013/140469

Bach, T. J., Rogers, D. H., & Rudney, H. (1986). Detergent-solubilization, purification, and characterization of membrane-bound 3-hydroxy-3-methylglutaryl-coenzyme A reductase from radish seedlings. *European Journal of Biochemistry*, *154*(1), 103–111. https://doi.org/10.1111/j.1432-1033.1986.tb09364.x

Banerjee, A., Wu, Y., Banerjee, R., Li, Y., Yan, H., & Sharkey, T. D. (2013). Feedback inhibition of deoxy-d-xylulose-5-phosphate synthase regulates the methylerythritol 4-phosphate pathway. *Journal of Biological Chemistry*, *288*(23), 16926–16936. https://doi.org/10.1074/jbc.M113.464636

Berthelot, K., Estevez, Y., Deffieux, A., & Peruch, F. (2012). Isopentenyl diphosphate isomerase: A checkpoint to isoprenoid biosynthesis. *Biochimie*, *94*, 1621–1634. https://doi.org/10.1016/j.biochi.2012.03.021

Bikas, H., Stavropoulos, P., & Chryssolouris, G. (2015). Additive manufacturing methods and modelling approaches: A critical review. *The International Journal of Advanced Manufacturing Technology*, *83*(1–4), 389–405. https://doi.org/10.1007/s00170-015-7576-2

Blanchette, C. D., Knipe, J. M., Stolaroff, J. K., DeOtte, J. R., Oakdale, J. S., Maiti, A., Lenhardt, J. M., Sirajuddin, S., Rosenzweig, A. C., & Baker, S. E. (2016). Printable enzyme-embedded materials for methane to methanol conversion. *Nature Communications*, *7*(1), 11900. https://doi.org/10.1038/ncomms11900

Boehm, C. R., Freemont, P. S., & Ces, O. (2013). Design of a prototype flow microreactor for synthetic biology in vitro. *Lab on a Chip*, *13*(17), 3426–3432. https://doi.org/10.1039/c3lc50231g

Boronat, A., & Rodríguez-Concepción, M. (2015). Terpenoid Biosynthesis in Prokaryotes. *Advances in Biochemical Engineering/Biotechnology*, *148*, 3–18. https://doi.org/10.1007/10_2014_285

Borovinskaya, E. S., & Reschetilowski, W. (2012). Perspectives of heterogeneous process intensification in microreactors. *Russian Journal of General Chemistry*, *82*(12), 2108–2115. https://doi.org/10.1134/S1070363212120316

Brooker, J. D., & Russell, D. W. (1975). Properties of microsomal 3-hydroxy-3-methylglutaryl coenzyme A reductase from pisum sativum seedlings. *Archives of Biochemistry and Biophysics*, *167*(2), 723–729. https://doi.org/10.1016/0003-9861(75)90517-2

Brostrom, M., & Browning, E. (1973). Choline kinase from brewers' yeast: Partial purification, properties, and kinetic mechanism. *The Journal of Biological Chemistry*, *248*(7), 2364–2371. https://doi.org/10.1016/S0021-9258(19)44118-5

Cerdeira Ferreira, L., da Costa, E. T., do Lago, C. L., & Angnes, L. (2013). Miniturized flow system based on enzyme modified PMMA microreactor for amoperometric determination of glucose. *Biosensors and Bioelectronics*, *47*, 539–544. https://doi.org/10.1016/j.bios.2013.03.052

Cerdeira Ferreira, L. M., da Costa, E. T., do Lago, C. L., & Angnes, L. (2013). Miniaturized flow system based on enzyme modified PMMA microreactor for amperometric determination of glucose. *Biosensors and Bioelectronics*, *47*, 539–544. https://doi.org/10.1016/j.bios.2013.03.052

Cerqueira, M. R. F., Santos, M. S. F., Matos, R. C., Gutz, I. G. R., & Angnes, L. (2015). Use of poly(methyl methacrylate)/polyethyleneimine flow microreactors for enzyme immobilization. *Microchemical Journal*, *118*, 231–237. https://doi.org/10.1016/j.microc.2014.09.009

Chandran, S. S., Kealey, J. T., & Reeves, C. D. (2011). Microbial production of isoprenoids. *Process Biochemistry*, *46*(9), 1703–1710. https://doi.org/10.1016/j.procbio.2011.05.012

Chang, Y.-J., Song, S.-H., Park, S.-H., & Kim, S.-U. (2000). Amorpha-4,11-diene synthase of Artemisia annua: CDNA isolation and bacterial expression of a terpene synthase involved in artemisinin biosynthesis. *Archives of Biochemistry and Biophysics*, *383*(2), 178–184. https://doi.org/10.1006/abbi.2000.2061

Chappelet-Tordo, D., Fosset, M., Iwatsubo, M., Gache, C., & Lazdunski, M. (1974). Intestinal alkaline phosphatase. Catalytic properties and half of the sites reactivity. *Biochemistry*, *13*(9), 1788–1795. https://doi.org/10.1021/bi00706a002

Chatzivasileiou, A. O., Ward, V., Edgar, S. M., & Stephanopoulos, G. (2019). Two-step pathway for isoprenoid synthesis. *Proceedings of the National Academy of Sciences*, *116*(2), 506–511. https://doi.org/10.1073/pnas.1812935116

Chauhan, N., & Pundir, C. S. (2011). Co-immobilization of cholesterol esterase, cholesterol oxidase and peroxidase on PVC strip for serum cholesterol determination. *Analytical Methods*, *3*(6), 1360. https://doi.org/10.1039/c1ay05082f

Chen, Y., Zhou, Y. J., Siewers, V., & Nielsen, J. (2015). Enabling technologies to advance microbial isoprenoid production. *Advances in Biochemical Engineering/Biotechnology*, *148*, 143–160. https://doi.org/10.1007/10_2014_284

Danckwerts, P. V. (1953). Continuous flow systems. Distribution of residence times. *Chemical Engineering Science*, *2*(1), 3857–3866. https://doi.org/10.1016/0009-2509(96)81811-2

Dellas, N., Thomas, S. T., Manning, G., & Noel, J. P. (2013). Discovery of a metabolic alternative to the classical mevalonate pathway. *ELife*, *2*, 1–18. https://doi.org/10.7554/eLife.00672

Dudley, Q., Karim, A., & Jewett, M. (2015). Cell-free metabolic engineering: Biomanufacturing beyond the cell. *Biotechnology Journal*, *10*(1), 69–82. https://doi.org/10.1002/biot.201400330

Dudley, Q. M., Karim, A. S., & Jewett, M. C. (2015). Cell-free metabolic engineering: Biomanufacturing beyond the cell. *Biotechnology Journal*, *10*(1), 69–82. https://doi.org/10.1002/biot.201400330

Erb, T. J., Jones, P. R., & Bar-Even, A. (2017). Synthetic metabolism: Metabolic engineering meets enzyme design. *Current Opinion in Chemical Biology*, *37*, 56–62. https://doi.org/10.1016/j.cbpa.2016.12.023

Farmer, W. R., & Liao, J. C. (2000). Improving lycopene production in Escherichia coli by engineering metabolic control. *Nature Biotechnology*, *18*(5), 533–537. https://doi.org/10.1038/75398

Faustino, V., Catarino, S. O., Lima, R., & Minas, G. (2016). Biomedical microfluidic devices by using low-cost fabrication techniques: A review. *Journal of Biomechanics*, *49*(11), 2280–2292. https://doi.org/10.1016/j.jbiomech.2015.11.031

Fornera, S., Kuhn, P., Lombardi, D., Schlüter, A. D., Dittrich, P. S., & Walde, P. (2012). Sequential immobilization of enzymes in microfluidic channels for cascade reactions. *ChemPlusChem*, *77*(2), 98–101. https://doi.org/10.1002/cplu.201100068

Fu, J., Liu, M., Liu, Y., Woodbury, N. W., & Yan, H. (2012). Interenzyme substrate diffusion for an enzyme cascade organized on spatially addressable DNA nanostructures. *Journal of the American Chemical Society*, *134*(12), 5516–5519. https://doi.org/10.1021/ja300897h

Fujisaki, S., Hara, H., Nishimura, Y., Horiuchi, K., & Nishino, T. (1990). Cloning and nucleotide sequence of the IspA gene responsible for farnesyl diphosphate synthase activity in Escherichia coli. *Journal of Biochemistry*, *108*, 995–1000. https://doi.org/10.1093/oxfordjournals.jbchem.a123327

George, K. W., Thompson, M. G., Kim, J., Baidoo, E. E. K., Wang, G., Benites, V. T., Petzold, C. J., Chan, L. J. G., Yilmaz, S., Turhanen, P., Adams, P. D., Keasling, J. D., & Lee, T. S. (2018). Integrated analysis of isopentenyl pyrophosphate (IPP) toxicity in isoprenoid-producing Escherichia coli. *Metabolic Engineering*, *47*, 60–72. https://doi.org/10.1016/j.ymben.2018.03.004

González-Henríquez, C. M., Sarabia-Vallejos, M. A., & Rodriguez-Hernandez, J. (2019). Polymers for additive manufacturing and 4D-printing: Materials, methodologies, and biomedical applications. *Progress in Polymer Science*, *94*, 57–116. https://doi.org/10.1016/j.progpolymsci.2019.03.001

Grant, J., Modica, J. A., Roll, J., Perkovich, P., & Mrksich, M. (2018). An immobilized enzyme reactor for spatiotemporal control over reaction products. *Small*, *14*(31), 1800923. https://doi.org/10.1002/smll.201800923

Hahn, F., Hurlburt, A., & Poulter, D. (1999). Escherichia coli open reading frame 696 is idi, a nonessential gene encoding isopentenyl diphosphate isomerase. *Journal of Bacteriology*, *181*(15), 4499–4504. https://doi.org/10.1128/JB.181.15.4499-4504.1999

Heo, J., & Crooks, R. M. (2005). Microfluidic biosensor based on an array of hydrogel-entrapped enzymes. *Analytical Chemistry*, *77*(21), 6843–6851. https://doi.org/10.1021/ac0507993

Hinson, D., Chambliss, K., Toth, M., Tanaka, R., & Gibson, M. (1997). Post-translational regulation of mevalonate kinase by intermediates of the cholesterol and nonsterol isoprene biosynthetic pathways. *Journal of Lipid Research*, *38*, 2216–2223. https://doi.org/10.1016/S0022-2275(20)34935-X

Hoffmann, C., Pereira Rosinha Grundtvig, I., Thrane, J., Garg, N., Gernaey, K. V., Pinelo, M., Woodley, J. M., Krühne, U., & Daugaard, A. E. (2018). Experimental and computational evaluation of area selectively immobilized horseradish peroxidase in a microfluidic device. *Chemical Engineering Journal*, *332*, 16–23. https://doi.org/10.1016/j.cej.2017.09.050

Hosfield, D., Zhang, Y., Dougan, D., Broun, A., Tari, L., Swanson, R., & Finn, J. (2004). Structural basis for bIspHosphonate-mediated inhibition of isoprenoid synthesis. *The Journal of Biological Chemistry*, *279*(10), 8526–8529. https://doi.org/10.1074/jbc.C300511200

Jesionowski, T., Zdarta, J., & Krajewska, B. (2014). Enzyme immobilization by adsorption: A review. *Adsorption*, *20*(5–6), 801–821. https://doi.org/10.1007/s10450-014-9623-y

Ji, Q., Wang, B., Tan, J., Zhu, L., & Li, L. (2016). Immobilized multienzymatic systems for catalysis of cascade reactions. *Process Biochemistry*, *51*(9), 1193–1203. https://doi.org/10.1016/j.procbio.2016.06.004

Jia, F., Narasimhan, B., & Mallapragada, S. (2014). Materials-based strategies for multi-enzyme immobilization and co-localization: A review. *Biotechnology and Bioengineering*, *111*(2), 209–222. https://doi.org/10.1002/bit.25136

Jones, F., Lu, Z., & Elmore, B. B. (2002). Development of novel microscale system as immobilized enzyme bioreactor. *Applied Biochemistry and Biotechnology*, *98–100*, 627–640. https://doi.org/10.1385/ABAB:98-100:1-9:627

Kang, A., George, K. W., Wang, G., Baidoo, E., Keasling, J. D., & Lee, T. S. (2016). Isopentenyl diphosphate (IPP)-bypass mevalonate pathways for isopentenol production. *Metabolic Engineering*, *34*, 25–35. https://doi.org/10.1016/j.ymben.2015.12.002

Kang, A., Meadows, C. W., Canu, N., Keasling, J. D., & Lee, T. S. (2017). High-throughput enzyme screening platform for the IPP-bypass mevalonate pathway for isopentenol production. *Metabolic Engineering*, *41*, 125–134. https://doi.org/10.1016/j.ymben.2017.03.010

Kazenwadel, F., Biegert, E., Wohlgemuth, J., Wagner, H., & Franzreb, M. (2016). A 3D-printed modular reactor setup including temperature and pH control for the compartmentalized implementation of enzyme cascades. *Engineering in Life Sciences*, *16*(6), 560–567. https://doi.org/10.1002/elsc.201600007

Kazenwadel, F., Franzreb, M., & Rapp, B. E. (2015). Synthetic enzyme supercomplexes: Co-immobilization of enzyme cascades. *Analytical Methods*, *7*(10), 4030–4037. https://doi.org/10.1039/C5AY00453E

Kim, K.-H., Voelker, D., Flocco, M., & Carman, G. (1998). Expression, purification, and characterization of choline kinase, product of the CKI gene from Saccharomyces cerevisiae. *The Journal of Biological Chemistry*, *273*(12), 6844–6852. https://doi.org/10.1074/jbc.273.12.6844

Kim, S.-H., Heo, K., Chang, Y.-J., Park, S.-H., Rhee, S.-K., & Kim, S.-U. (2006). Cyclization mechanism of amorpha-4,11-diene synthase, a key enzyme in artemisinin biosynthesis. *Journal of Natural Products*, *69*, 758–762. https://doi.org/10.1021/np050356u

King, J. R., Woolston, B. M., & Stephanopoulos, G. (2017). Designing a new entry point into isoprenoid metabolism by exploiting fructose-6-phosphate aldolase side reactivity of Escherichia coli. *ACS Synthetic Biology*, *6*(7), 1416–1426. https://doi.org/10.1021/acssynbio.7b00072

Korman, T. P., Opgenorth, P. H., & Bowie, J. U. (2017). A synthetic biochemistry platform for cell free production of monoterpenes from glucose. *Nature Communications*, *8*(1), 1–8. https://doi.org/10.1038/ncomms15526

Ku, B., Jeong, J.-C., Mijts, B. N., Schmidt-Dannert, C., & Dordick, J. S. (2005). Preparation, characterization, and optimization of an in vitro C30 carotenoid pathway. *Applied and Environmental Microbiology*, *71*(11), 6578–6583. https://doi.org/10.1128/AEM.71.11.6578-6583.2005

Kulsharova, G., Dimov, N., Marques, M. P. C., Szita, N., & Baganz, F. (2018). Simplified immobilisation method for histidine-tagged enzymes in poly(methyl methacrylate) microfluidic devices. *New Biotechnology*, *47*, 31–38. https://doi.org/10.1016/j.nbt.2017.12.004

Lange, B. M., & Croteau, R. (1999). Isopentenyl diphosphate biosynthesis via a mevalonate-independent pathway: Isopentenyl monophosphate kinase catalyzes the terminal enzymatic step. *Proceedings of the National Academy of Sciences*, *96*(24), 13714–13719. https://doi.org/10.1073/pnas.96.24.13714

Lee, J. W., Na, D., Park, J. M., Lee, J., Choi, S., & Lee, S. Y. (2012). Systems metabolic engineering of microorganisms for natural and non-natural chemicals. *Nature Chemical Biology*, *8*(6), 536–546. https://doi.org/10.1038/nchembio.970

Leonard, E., Ajikumar, P. K., Thayer, K., Xiao, W.-H., Mo, J. D., Tidor, B., Stephanopoulos, G., & Prather, K. L. J. (2010). Combining metabolic and protein engineering of a terpenoid biosynthetic pathway for overproduction and selectivity control. *Proceedings of the National Academy of Sciences*, *107*(31), 13654–13659. https://doi.org/10.1073/pnas.1006138107

Liao, C.-A., Wu, Q., Wei, Q.-C., & Wang, Q.-G. (2015). Bioinorganic nanocomposite hydrogels formed by HRP-GOx-cascade-catalyzed polymerization and exfoliation of the layered composites. *Chemistry - A European Journal*, *21*(36), 12620–12626. https://doi.org/10.1002/chem.201501529

Liebermeister, W., & Klipp, E. (2006). Bringing metabolic networks to life: Convenience rate law and thermodynamic constraints. *Theoretical Biology and Medical Modelling*, *3*(1), 41. https://doi.org/10.1186/1742-4682-3-41

Lira, L. M., Vasilev, D., Pilli, R. A., & Wessjohann, L. A. (2013). One-pot synthesis of organophosphate monoesters from alcohols. *Tetrahedron Letters*, *54*(13), 1690–1692. https://doi.org/10.1016/j.tetlet.2013.01.059

Liu, H., Sun, Y., Ramos, K. R. M., Nisola, G. M., Valdehuesa, K. N. G., Lee, W., Park, S. J., & Chung, W.J. (2013). Combination of Entner-Doudoroff pathway with MEP increases isoprene production in engineered Escherichia coli. *PLoS ONE*, *8*(12), e83290. https://doi.org/10.1371/journal.pone.0083290

Logan, T. C., Clark, D. S., Stachowiak, T. B., Svec, F., & Fréchet, J. M. J. (2007). Photopatterning enzymes on polymer monoliths in microfluidic devices for steady-state kinetic analysis and spatially separated multi-enzyme reactions. *Analytical Chemistry*, *79*(17), 6592–6598. https://doi.org/10.1021/ac070705k

Mandon, C., Blum, L., & Marquette, C. (2017). 3D–4D Printed objects: New bioactive material opportunities. *Micromachines*, *8*(4), 102. https://doi.org/10.3390/mi8040102

Marsafari, M., & Xu, P. (2020). Debottlenecking mevalonate pathway for antimalarial drug precursor amorphadiene biosynthesis in Yarrowia lipolytica. *Metabolic Engineering Communications*, *10*, e00121. https://doi.org/10.1016/j.mec.2019.e00121

Martin, V. J. J., Pitera, D. J., Withers, S. T., Newman, J. D., & Keasling, J. D. (2003). Engineering a mevalonate pathway in Escherichia coli for production of terpenoids. *Nature Biotechnology*, *21*(7), 796–802. https://doi.org/10.1038/nbt833

Mathesh, M., Liu, J., Barrow, C. J., & Yang, W. (2017). Graphene-oxide-based enzyme nanoarchitectonics for substrate channeling. *Chemistry - A European Journal*, *23*(2), 304–311. https://doi.org/10.1002/chem.201604348

McNerney, M. P., Watstein, D. M., & Styczynski, M. P. (2015). Precision metabolic engineering: The design of responsive, selective, and controllable metabolic systems. *Metabolic Engineering*, *31*, 123–131. https://doi.org/10.1016/j.ymben.2015.06.011

Meller, K., Szumski, M., & Buszewski, B. (2017). Microfluidic reactors with immobilized enzymes—Characterization, dividing, perspectives. *Sensors and Actuators B: Chemical*, *244*, 84–106. https://doi.org/10.1016/j.snb.2016.12.021

Mercke, P., Bengtsson, M., Bouwmeester, H., Posthumus, M., & Brodelius, P. (2000). Molecular cloning, expression, and characterization of amorpha-4,11-diene synthase, a key enzyme of artemisinin biosynthesis in Artemisia annua L. *Archives of Biochemistry and Biophysics*, *381*(2), 173–180. https://doi.org/10.1006/abbi.2000.1962

Morrone, D., Lowry, L., Determan, M. K., Hershey, D. M., Xu, M., & Peters, R. J. (2010). Increasing diterpene yield with a modular metabolic engineering system in E. coli: Comparison of MEV and MEP isoprenoid precursor pathway engineering. *Applied Microbiology and Biotechnology*, *85*(6), 1893–1906. https://doi.org/10.1007/s00253-009-2219-x

Muschiol, J., Peters, C., Oberleitner, N., Mihovilovic, M. D., Bornscheuer, U. T., & Rudroff, F. (2015). Cascade catalysis – strategies and challenges en route to preparative synthetic biology. *Chemical Communications*, *51*(27), 5798–5811. https://doi.org/10.1039/C4CC08752F

Nagegowda, D. A., Bach, T. J., & Chye, M.-L. (2004). Brassica juncea 3-hydroxy-3-methylglutaryl (HMG)-CoA synthase 1: Expression and characterization of recombinant wild-type and mutant enzymes. *Biochemical Journal*, *383*(3), 517–527. https://doi.org/10.1042/BJ20040721

Nakagawa, K., Tamura, A., & Chaiya, C. (2014). Preparation of proteolytic microreactors by freeze-drying immobilization. *Chemical Engineering Science*, *119*, 22–29. https://doi.org/10.1016/j.ces.2014.07.054

Newman, J. D., Marshall, J., Chang, M., Nowroozi, F., Paradise, E., Pitera, D., Newman, K. L., & Keasling, J. D. (2006). High-level production of amorpha-4,11-diene in a two-phase partitioning bioreactor of metabolically engineered Escherichia coli. *Biotechnology and Bioengineering*, *95*(4), 684–691. https://doi.org/10.1002/bit.21017

Ngo, T. D., Kashani, A., Imbalzano, G., Nguyen, K. T. Q., & Hui, D. (2018). Additive manufacturing (3D printing): A review of materials, methods, applications and challenges. *Composites Part B: Engineering*, *143*, 172–196. https://doi.org/10.1016/j.compositesb.2018.02.012

Nouaimi, M., Möschel, K., & Bisswanger, H. (2001). Immobilization of trypsin on polyester fleece via different spacers. *Enzyme and Microbial Technology*, *29*, 567–574. https://doi.org/10.1016/S0141-0229(01)00429-X

Ogończyk, D., Jankowski, P., & Garstecki, P. (2012). Functionalization of polycarbonate with proteins; open-tubular enzymatic microreactors. *Lab on a Chip*, *12*(15), 2743. https://doi.org/10.1039/c2lc40204a

Oshige, M., Yumoto, K., Miyata, H., Takahashi, S., Nakada, M., Ito, K., Tamegai, M., Kawaura, H., & Katsura, S. (2013). Immobilization of his-tagged proteins on various solid surfaces using NTA-modified chitosan. *Open Journal of Polymer Chemistry*, *3*(1), 6–10. https://doi.org/10.4236/ojpchem.2013.31002

Peris, E., Okafor, O., Kulcinskaja, E., Goodridge, R., Luis, S. V., Garcia-Verdugo, E., O'Reilly, E., & Sans, V. (2017). Tuneable 3D printed bioreactors for transaminations under continuous-flow. *Green Chemistry*, *19*(22), 5345–5349. https://doi.org/10.1039/C7GC02421E

Picaud, S., Olofsson, L., Brodelius, M., & Brodelius, P. (2005). Expression, purification, and characterization of recombinant amorpha-4,11-diene synthase from Artemisia annua L. *Archives of Biochemistry and Biophysics*, *436*, 215–226. https://doi.org/10.1016/j.abb.2005.02.012

Pickens, L. B., Tang, Y., & Chooi, Y.-H. (2011). Metabolic engineering for the production of natural products. *Annual Review of Chemical and Biomolecular Engineering*, *2*(1), 211–236. https://doi.org/10.1146/annurev-chembioeng-061010-114209

Pitera, D. J., Paddon, C. J., Newman, J. D., & Keasling, J. D. (2007). Balancing a heterologous mevalonate pathway for improved isoprenoid production in Escherichia coli. *Metabolic Engineering*, *9*(2), 193–207. https://doi.org/10.1016/j.ymben.2006.11.002

Pramastya, H., Xue, D., Abdallah, I. I., Setroikromo, R., & Quax, W. J. (2021). High level production of amorphadiene using Bacillus subtilis as an optimized terpenoid cell factory. *New Biotechnology*, *60*, 159–167. https://doi.org/10.1016/j.nbt.2020.10.007

Rapp, B. E. (2017). *Microfluidics: Modelling, mechanics, and mathematics* (1st ed.). Elsevier Inc.

Redding-Johanson, A. M., Batth, T. S., Chan, R., Krupa, R., Szmidt, H. L., Adams, P. D., Keasling, J. D., Soon Lee, T., Mukhopadhyay, A., & Petzold, C. J. (2011). Targeted proteomics for metabolic pathway optimization: Application to terpene production. *Metabolic Engineering*, *13*(2), 194–203. https://doi.org/10.1016/j.ymben.2010.12.005

Reetz, M. T., Zonta, A., & Simpelkamp, J. (1996). Efficient immobilization of lipases by entrapment in hydrophobic sol-gel materials. *Biotechnology and Bioengineering*, *49*(5), 527–534. https://doi.org/10.1002/(SICI)1097-0290(19960305)49:5<527::AID-BIT5>3.0.CO;2-L

Ro, D.-K., Paradise, E. M., Ouellet, M., Fisher, K. J., Newman, K. L., Ndungu, J. M., Ho, K. A., Eachus, R. A., Ham, T. S., Kirby, J., Chang, M. C. Y., Withers, S. T., Shiba, Y., Sarpong, R., & Keasling, J. D. (2006). Production of the antimalarial drug precursor artemisinic acid in engineered yeast. *Nature*, *440*(7086), 940–943. https://doi.org/10.1038/nature04640

Rodriguez, S., Kirby, J., Denby, C., & Keasling, J. (2014). Production and quantification of sesquiterpenes in Saccharomyces cerevisiae, including extraction, detection and quantification of terepene products and ket related metabolites. *Nature Protocols*, *9*(8), 1980–1996. https://doi.org/10.1038/nprot.2014.132

Schäpper, D., Lencastre Fernandes, R., Lantz, A. E., Okkels, F., Bruus, H., & Gernaey, K. V. (2011). Topology optimized microbioreactors. *Biotechnology and Bioengineering*, *108*(4), 786–796. https://doi.org/10.1002/bit.23001

Schmieg, B., Döbber, J., Kirschhöfer, F., Pohl, M., & Franzreb, M. (2019). Advantages of hydrogel-based 3D-printed enzyme reactors and their limitations for biocatalysis. *Frontiers in Bioengineering and Biotechnology*, *6*(211), 1–12. https://doi.org/10.3389/fbioe.2018.00211

Scopes, R. (1995). The effect of temperature on enzymes used in diagnostics. *Clinica Chimica Acta*, *237*(1–2), 17–23. https://doi.org/10.1016/0009-8981(95)06060-Q

Sheldon, R. A., & Woodley, J. M. (2018). Role of biocatalysis in sustainable chemistry. *Chemical Reviews*, *118*(2), 801–838. https://doi.org/10.1021/acs.chemrev.7b00203

Shukal, S., Chen, X., & Zhang, C. (2019). Systematic engineering for high-yield production of viridiflorol and amorphadiene in auxotrophic Escherichia coli. *Metabolic Engineering*, *55*, 170–178. https://doi.org/10.1016/j.ymben.2019.07.007

Straathof, A. J. J., Panke, S., & Schmid, A. (2002). The production of fine chemicals by biotransformations. *Current Opinion in Biotechnology*, *13*(6), 548–556. https://doi.org/10.1016/S0958-1669(02)00360-9

Su, C.-K., Yen, S.-C., Li, T.-W., & Sun, Y.-C. (2016). Enzyme-immobilized 3D-printed reactors for online monitoring of rat brain extracellular glucose and lactate. *Analytical Chemistry*, *88*(12), 6265–6273. https://doi.org/10.1021/acs.analchem.6b00272

Sun, T., Miao, L., Li, Q., Dai, G., Lu, F., Liu, T., Zhang, X., & Ma, Y. (2014). Production of lycopene by metabolically-engineered Escherichia coli. *Biotechnology Letters*, *36*(7), 1515–1522. https://doi.org/10.1007/s10529-014-1543-0

Tsuruta, H., Paddon, C. J., Eng, D., Lenihan, J. R., Horning, T., Anthony, L. C., Regentin, R., Keasling, J. D., Renninger, N. S., & Newman, J. D. (2009). High-Level Production of amorpha-4,11-diene, a precursor of the antimalarial agent artemisinin, in Escherichia coli. *PLoS ONE*, *4*(2), e4489. https://doi.org/10.1371/journal.pone.0004489

Underwood, P., Kananen, G., & Armitage, E. (1997). A practical approach to determination of laboratory GC-MS limits of detection. *Journal of Analytical Toxicology*, *21*(1), 12–16. https://doi.org/10.1093/jat/21.1.12

UniProtKB - Q8H1F7 (IPK_ARATH). (2021). *UniProt*. https://www.uniprot.org/uniprot/Q8H1F7

Vickers, C. E., Bongers, M., Liu, Q., Delatte, T., & Bouwmeester, H. (2014). Metabolic engineering of volatile isoprenoids in plants and microbes. *Plant, Cell & Environment*, *37*(8), 1753–1775. https://doi.org/10.1111/pce.12316

Voynova, N. E., Rios, S. E., & Miziorko, H. M. (2004). Staphylococcus aureus mevalonate kinase: Isolation and characterization of an enzyme of the isoprenoid biosynthetic pathway. *Journal of Bacteriology*, *186*(1), 61–67. https://doi.org/10.1128/JB.186.1.61-67.2004

Wang, C.-W., Oh, M.-K., & Liao, J. C. (1999). Engineered isoprenoid pathway enhances astaxanthin production in Escherichia coli. *Biotechnology and Bioengineering*, *62*(2), 7. https://doi.org/10.1002/(SICI)1097-0290(19990120)62:2<235::AID-BIT14>3.0.CO;2-U

Wang, T., Ma, J., Zhu, G., Shan, Y., Liang, Z., Zhang, L., & Zhang, Y. (2010). Integration of capillary isoelectric focusing with monolithic immobilized pH gradient, immobilized trypsin microreactor and capillary zone electrophoresis for on-line protein analysis. *Journal of Separation Science*, *33*(20), 3194–3200. https://doi.org/10.1002/jssc.201000324

Ward, V. C. A., Chatzivasileiou, A. O., & Stephanopoulos, G. (2019). Cell free biosynthesis of isoprenoids from isopentenol. *Biotechnology and Bioengineering*, *116*(12), 3269–3281. https://doi.org/10.1002/bit.27146

Weaver, L. J., Sousa, M. M. L., Wang, G., Baidoo, E., Petzold, C. J., & Keasling, J. D. (2015). A kinetic-based approach to understanding heterologous mevalonate pathway function in E. coli. *Biotechnology and Bioengineering*, *112*(1), 111–119. https://doi.org/10.1002/bit.25323

Westfall, P. J., Pitera, D. J., Lenihan, J. R., Eng, D., Woolard, F. X., Regentin, R., Horning, T., Tsuruta, H., Melis, D. J., Owens, A., Fickes, S., Diola, D., Benjamin, K. R., Keasling, J. D., Leavell, M. D., McPhee, D. J., Renninger, N. S., Newman, J. D., & Paddon, C. J. (2012). Production of amorphadiene in yeast, and its conversion to dihydroartemisinic acid, precursor to the antimalarial agent artemisinin. *Proceedings of the National Academy of Sciences*, *109*(3), E111–E118. https://doi.org/10.1073/pnas.1110740109

Wilke, C. R., & Chang, P. (1955). Correlation of diffusion coefficients in dilute solutions. *AIChE Journal*, *1*(2), 264–270. https://doi.org/10.1002/aic.690010222

Willrodt, C., David, C., Cornelissen, S., Bühler, B., Julsing, M. K., & Schmid, A. (2014). Engineering the productivity of recombinant Escherichia coli for limonene formation from glycerol in minimal media. *Biotechnology Journal*, *9*(8), 1000–1012. https://doi.org/10.1002/biot.201400023

Wollenberg, L. A., Kabulski, J. L., Powell, M. J., Chen, J., Flora, D. R., Tracy, T. S., & Gannett, P. M. (2014). The use of immobilized cytochrome P4502C9 in PMMA-based plug flow bioreactors for the production of drug metabolites. *Applied Biochemistry and Biotechnology*, *172*(3), 1293–1306. https://doi.org/10.1007/s12010-013-0537-z

Woo, H. M., Murray, G. W., Batth, T. S., Prasad, N., Adams, P. D., Keasling, J. D., Petzold, C. J., & Lee, T. S. (2013). Application of targeted proteomics and biological parts assembly in E. coli to optimize the biosynthesis of an anti-malarial drug precursor, amorpha-4,11-diene. *Chemical Engineering Science*, *103*, 21–28. https://doi.org/10.1016/j.ces.2013.04.033

Woolston, B. M., Edgar, S., & Stephanopoulos, G. (2013). Metabolic engineering: Past and future. *Annual Review of Chemical and Biomolecular Engineering*, *4*(1), 259–288. https://doi.org/10.1146/annurev-chembioeng-061312-103312

Xu, S., Lu, Y., Li, J., Jiang, Z., & Wu, H. (2006). Efficient conversion of CO2 to methanol catalyzed by three dehydrogenases co-encapsulated in an alginate−silica (ALG−SiO2) hybrid gel. *Industrial and Engineering Chemistry Research*, *45*(13), 4567–4573. https://doi.org/10.1021/ie051407l

Xue, R., & Woodley, J. M. (2012). Process technology for multi-enzymatic reaction systems. *Bioresource Technology*, *115*, 183–195. https://doi.org/10.1016/j.biortech.2012.03.033

Yadav, V. G., De Mey, M., Giaw Lim, C., Kumaran Ajikumar, P., & Stephanopoulos, G. (2012). The future of metabolic engineering and synthetic biology: Towards a systematic practice. *Metabolic Engineering*, *14*(3), 233–241. https://doi.org/10.1016/j.ymben.2012.02.001

Yuan, L. Z., Rouvière, P. E., LaRossa, R. A., & Suh, W. (2006). Chromosomal promoter replacement of the isoprenoid pathway for enhancing carotenoid production in E. coli. *Metabolic Engineering*, *8*(1), 79–90. https://doi.org/10.1016/j.ymben.2005.08.005

Zhang, C., Zou, R., Chen, X., Stephanopoulos, G., & Too, H.-P. (2015). Experimental design-aided systematic pathway optimization of glucose uptake and deoxylulose phosphate pathway for improved amorphadiene production. *Applied Microbiology and Biotechnology*, *99*(9), 3825–3837. https://doi.org/10.1007/s00253-015-6463-y

Zhang, Y.-H. P. (2011). Simpler is better: High-yield and potential low-cost biofuels production through cell-free synthetic pathway biotransformation (SyPaB). *ACS Catalysis*, *1*(9), 998–1009. https://doi.org/10.1021/cs200218f

Zhou, K., Zou, R., Stephanopoulos, G., & Too, H.-P. (2012). Metabolite profiling identified methylerythritol cyclodiphosphate efflux as a limiting step in microbial isoprenoid production. *PLoS ONE*, *7*(11), e47513. https://doi.org/10.1371/journal.pone.0047513

Zhu, Y., Chen, Q., Shao, L., Jia, Y., & Zhang, X. (2020). Microfluidic immobilized enzyme reactors for continuous biocatalysis. *Reaction Chemistry and Engineering*, *5*(1), 9–32. https://doi.org/10.1039/C9RE00217K

Appendices

Appendix I – Primer Sequences

Table 9: Primers required for Gibson assembly and colony PCR.

Primers	Sequence (forward and reverse)	Tm (°C)
pET28	atccggctgctaacaaag cggtatatctccttcttaaagttaaac	57.1
CK	tttaagaaggagatataccgatggtgcaggagtcccgc ggctttgttagcagccggattcagtggtggtggtggtgcaggtagctggtgtcgagg	62.9
IPK	tttaagaaggagatataccgatggaactcaatatcagcgaaag ggctttgttagcagccggattcagtggtggtggtggtgtttgctgaagcggatgatg	58.3
IDI	tttaagaaggagatataccgatgcaaacggaacacgtc ggctttgttagcagccggattcagtggtggtggtggtgtttaagctgggtaaatgcag	56.8
IspA	tttaagaaggagatataccgatggactttccgcagcaac ggctttgttagcagccggattcagtggtggtggtggtgtttattacgctggatgatgtagtc	59.3
ADS	tttaagaaggagatataccgatggccctgaccgaagag ggctttgttagcagccggattcagtggtggtggtggtggatggacatcgggtaaacc	59.1
cPCR-CK	ggtgatgtcggcgatatagg ccttgaagatcgcattggtc	-
cPCR-PK	ggtgatgtcggcgatatagg atgatgacatcgccggacag	-
cPCR-IDI	ggtgatgtcggcgatatagg cacaccattgataatccatcac	-
cPCR-IspA	ggtgatgtcggcgatatagg tcaagacccagaagtgcagg	-
cPCR-ADS	ggtgatgtcggcgatatagg agcagggtcttgttgtgagag	-

Appendix II – Enzyme Assay Raw Data

Table 10: Raw data for free enzyme kinetic assays (excluding blanks).

Concentration (µM)							
ISP	IP	ATP	IPP	DMAPP	GPP	FPP	v (µM/s)
5000	-	280	-	-	-	-	0.00213
5000	-	140	-	-	-	-	0.00244
5000	-	70.0	-	-	-	-	0.00136
5000	-	35.0	-	-	-	-	0.00097
5000	-	560	-	-	-	-	0.00261
5000	-	280	-	-	-	-	0.00114
5000	-	140	-	-	-	-	0.00135
5000	-	70.0	-	-	-	-	0.00077
5000	-	35.0	-	-	-	-	0.00079
2500	-	560	-	-	-	-	0.00150
2500	-	560	-	-	-	-	0.00278
1250	-	560	-	-	-	-	0.00142
1250	-	560	-	-	-	-	0.00209
625	-	560	-	-	-	-	0.00254
625	-	560	-	-	-	-	0.00163
312.5	-	560	-	-	-	-	0.00154
312.5	-	560	-	-	-	-	0.00271
-	203	4266	-	-	-	-	0.01046
-	101	4266	-	-	-	-	0.00897
-	50.7	4266	-	-	-	-	0.00843
-	25.3	4266	-	-	-	-	0.00633
-	12.7	4266	-	-	-	-	0.00423
-	203	49.6	-	-	-	-	0.00617
-	203	24.8	-	-	-	-	0.00363
-	203	12.4	-	-	-	-	0.00235
-	203	6.2	-	-	-	-	0.00144
-	203	4266	-	-	-	-	0.00997
-	101	4266	-	-	-	-	0.00916
-	50.7	4266	-	-	-	-	0.00777
-	25.3	4266	-	-	-	-	0.00590
-	12.7	4266	-	-	-	-	0.00403
-	203	12.4	-	-	-	-	0.00227
-	203	6.2	-	-	-	-	0.00144
-	-	-	150	10.0	-	-	0.00629
-	-	-	150	5.0	-	-	0.00566
-	-	-	150	2.5	-	-	0.00617
-	-	-	150	1.3	-	-	0.00453
-	-	-	37.5	10.0	-	-	0.00649

Concentration (μM)							
ISP	**IP**	**ATP**	**IPP**	**DMAPP**	**GPP**	**FPP**	**ν (μM/s)**
-	-	-	37.5	25.0	-	-	0.00583
-	-	-	18.8	25.0	-	-	0.00500
-	-	-	9.4	25.0	-	-	0.00247
-	-	-	75.0	6.3	-	-	0.00645
-	-	-	75.0	3.1	-	-	0.00587
-	-	-	75.0	1.6	-	-	0.00532
-	-	-	75.0	25.0	-	-	0.00608
-	-	-	37.5	25.0	-	-	0.00537
-	-	-	18.8	25.0	-	-	0.00522
-	-	-	9.4	25.0	-	-	0.00441
-	-	-	75.0	6.3	-	-	0.00594
-	-	-	75.0	3.1	-	-	0.00587
-	-	-	75.0	1.6	-	-	0.00547
-	-	-	10.0	-	20.0	-	0.00690
-	-	-	5.0	-	20.0	-	0.00522
-	-	-	2.5	-	20.0	-	0.00315
-	-	-	10.0	-	10.0	-	0.00560
-	-	-	10.0	-	5.0	-	0.00358
-	-	-	10.0	-	20.0	-	0.00695
-	-	-	5.0	-	20.0	-	0.00561
-	-	-	2.5	-	20.0	-	0.00365
-	-	-	1.3	-	20.0	-	0.00277
-	-	-	10.0	-	10.0	-	0.00518
-	-	-	10.0	-	5.0	-	0.00474
-	-	-	10.0	-	2.5	-	0.00373
-	-	-	10.0	-	20.0	-	0.00695
-	-	-	5.0	-	20.0	-	0.00527
-	-	-	2.5	-	20.0	-	0.00372
-	-	-	1.3	-	20.0	-	0.00232
-	-	-	10.0	-	10.0	-	0.00563
-	-	-	10.0	-	5.0	-	0.00381
-	-	-	10.0	-	2.5	-	0.00226
-	-	-	-	-	-	10.0	0.00733
-	-	-	-	-	-	2.5	0.00432
-	-	-	-	-	-	1.3	0.00277
-	-	-	-	-	-	0.6	0.00298
-	-	-	-	-	-	0.3	0.00195
-	-	-	-	-	-	0.2	0.00170
-	-	-	-	-	-	10.0	0.00738
-	-	-	-	-	-	5.0	0.00129
-	-	-	-	-	-	2.5	0.00326
-	-	-	-	-	-	1.3	0.00289

Concentration (μM)							
ISP	IP	ATP	IPP	DMAPP	GPP	FPP	ν (μM/s)
-	-	-	-	-	-	0.6	0.00199
-	-	-	-	-	-	0.3	0.00150
-	-	-	-	-	-	0.2	0.00272
-	-	-	-	-	-	5.0	0.00512
-	-	-	-	-	-	2.5	0.00398
-	-	-	-	-	-	1.3	0.00293
-	-	-	-	-	-	0.6	0.00186
-	-	-	-	-	-	0.3	0.00113
-	-	-	-	-	-	5.0	0.00501
-	-	-	-	-	-	2.5	0.00411
-	-	-	-	-	-	1.3	0.00288
-	-	-	-	-	-	0.6	0.00195
-	-	-	-	-	-	0.3	0.00117

Table 11: Raw data for immobilized enzyme kinetic assays (excluding blanks).

Concentration (µM)							
ISP	**IP**	**ATP**	**IPP**	**DMAPP**	**GPP**	**FPP**	**ν (µM/s)**
5000	-	560	-	-	-	-	3.96E-05
5000	-	280	-	-	-	-	2.42E-05
5000	-	140	-	-	-	-	1.75E-05
5000	-	70.0	-	-	-	-	2.66E-05
2500	-	560	-	-	-	-	4.29E-05
625	-	560	-	-	-	-	1.08E-05
5000	-	560	-	-	-	-	2.75E-05
5000	-	140	-	-	-	-	2.92E-05
5000	-	70.0	-	-	-	-	2.08E-05
2500	-	560	-	-	-	-	2.99E-05
625	-	560	-	-	-	-	1.46E-05
-	269	5722	-	-	-	-	9.13E-05
-	269	5722	-	-	-	-	5.93E-05
-	67.3	5722	-	-	-	-	7.63E-05
-	16.8	5722	-	-	-	-	4.66E-05
-	269	5722	-	-	-	-	8.96E-05
-	269	5722	-	-	-	-	9.78E-05
-	67.3	5722	-	-	-	-	8.28E-05
-	16.8	5722	-	-	-	-	8.30E-05
-	-	-	10.0	-	20.0	-	3.09E-05
-	-	-	5.0	-	20.0	-	2.74E-05
-	-	-	2.5	-	20.0	-	1.26E-05
-	-	-	1.3	-	20.0	-	1.39E-05
-	-	-	10.0	-	10.0	-	2.14E-05
-	-	-	10.0	-	5.0	-	1.84E-05
-	-	-	10.0	-	2.5	-	1.84E-05
-	-	-	10.0	-	1.3	-	6.07E-06
-	-	-	10.0	-	20.0	-	3.89E-05
-	-	-	5.0	-	20.0	-	2.54E-05
-	-	-	2.5	-	20.0	-	9.05E-06
-	-	-	1.3	-	20.0	-	1.09E-05
-	-	-	10.0	-	10.0	-	2.94E-05
-	-	-	10.0	-	5.0	-	1.57E-05
-	-	-	10.0	-	2.5	-	1.62E-05
-	-	-	10.0	-	1.3	-	5.08E-06
-	-	-	75.0	8.3	-	-	5.67E-05
-	-	-	75.0	4.2	-	-	4.04E-05
-	-	-	75.0	2.1	-	-	4.19E-05
-	-	-	75.0	1.0	-	-	2.76E-05
-	-	-	75.0	25.0	-	-	4.51E-05

Concentration (μM)							
ISP	**IP**	**ATP**	**IPP**	**DMAPP**	**GPP**	**FPP**	**ν (μM/s)**
-	-	-	37.5	25.0	-	-	3.08E-05
-	-	-	18.8	25.0	-	-	2.86E-05
-	-	-	9.4	25.0	-	-	3.06E-05
-	-	-	75.0	8.3	-	-	5.71E-05
-	-	-	75.0	4.2	-	-	4.61E-05
-	-	-	75.0	2.1	-	-	3.68E-05
-	-	-	75.0	1.0	-	-	3.37E-05
-	-	-	75.0	25.0	-	-	5.00E-05
-	-	-	37.5	25.0	-	-	4.36E-05
-	-	-	18.8	25.0	-	-	2.97E-05
-	-	-	9.4	25.0	-	-	2.04E-05
-	-	-	-	-	-	10.0	1.99E-05
-	-	-	-	-	-	10.0	2.29E-05
-	-	-	-	-	-	5.0	1.17E-05
-	-	-	-	-	-	5.0	1.33E-05
-	-	-	-	-	-	2.5	9.93E-06
-	-	-	-	-	-	0.6	4.26E-06
-	-	-	-	-	-	0.3	3.21E-06
-	-	-	-	-	-	10.0	3.29E-05
-	-	-	-	-	-	5.0	1.49E-05
-	-	-	-	-	-	2.5	2.23E-05
-	-	-	-	-	-	0.3	3.34E-06